AFRL-PR-WP-TM-2006-2177

AMORPHOUS AND NANOCRYSTALLINE HIGH TEMPERATURE MAGNETIC MATERIAL FOR PWR

Michael E. McHenry

Carnegie Mellon University
5000 Forbes Avenue
Pittsburgh, PA 15213

MARCH 2006

Final Report for 18 July 2002 – 03 March 2006

Approved for public release; distribution is unlimited.

STINFO COPY

PROPULSION DIRECTORATE
AIR FORCE MATERIEL COMMAND
AIR FORCE RESEARCH LABORATORY
WRIGHT-PATTERSON AIR FORCE BASE, OH 45433-7251

NOTICE

Using Government drawings, specifications, or other data included in this document for any purpose other than Government procurement does not in any way obligate the U.S. Government. The fact that the Government formulated or supplied the drawings, specifications, or other data does not license the holder or any other person or corporation; or convey any rights or permission to manufacture, use, or sell any patented invention that may relate to them.

This report was cleared for public release by the Air Force Research Laboratory Wright Site (AFRL/WS) Public Affairs Office (PAO) and is releasable to the National Technical Information Service (NTIS). It will be available to the general public, including foreign nationals.

PAO case number: AFRL/WS 06-0876
Date cleared: 06 Apr 2006

THIS TECHNICAL REPORT IS APPROVED FOR PUBLICATION.

//Signature//   //Signature//

_____   _____
JOHN C. HORWATH   JAMES TSCHANTZ
Electrical Engineer   Acting Chief
Power Generation Branch   Power Generation Branch

//Signature//

_____
KIRK L. YERKES, PhD
Deputy for Science
Power Division

This report is published in the interest of scientific and technical information exchange and its publication does not constitute the Government's approval or disapproval of its ideas or findings.

REPORT DOCUMENTATION PAGE		*Form Approved* *OMB No. 0704-0188*

The public reporting burden for this collection of information is estimated to average 1 hour per response, including the time for reviewing instructions, searching existing data sources, searching existing data sources, gathering and maintaining the data needed, and completing and reviewing the collection of information. Send comments regarding this burden estimate or any other aspect of this collection of information, including suggestions for reducing this burden, to Department of Defense, Washington Headquarters Services, Directorate for Information Operations and Reports (0704-0188), 1215 Jefferson Davis Highway, Suite 1204, Arlington, VA 22202-4302. Respondents should be aware that notwithstanding any other provision of law, no person shall be subject to any penalty for failing to comply with a collection of information if it does not display a currently valid OMB control number. **PLEASE DO NOT RETURN YOUR FORM TO THE ABOVE ADDRESS.**

1. REPORT DATE *(DD-MM-YY)*	2. REPORT TYPE	3. DATES COVERED *(From - To)*
March 2006	Final	07/18/2002 – 03/03/2006

4. TITLE AND SUBTITLE	5a. CONTRACT NUMBER
AMORPHOUS AND NANOCRYSTALLINE HIGH TEMPERATURE MAGNETIC MATERIAL FOR PWR	F33615-02-2-2241
	5b. GRANT NUMBER
	5c. PROGRAM ELEMENT NUMBER 62805F

6. AUTHOR(S)	5d. PROJECT NUMBER
Michael E. McHenry	3145
	5e. TASK NUMBER 13
	5f. WORK UNIT NUMBER 0G

7. PERFORMING ORGANIZATION NAME(S) AND ADDRESS(ES)	8. PERFORMING ORGANIZATION REPORT NUMBER
Carnegie Mellon University 5000 Forbes Avenue Pittsburgh, PA 15213	

9. SPONSORING/MONITORING AGENCY NAME(S) AND ADDRESS(ES)	10. SPONSORING/MONITORING AGENCY ACRONYM(S)
Propulsion Directorate Air Force Research Laboratory Air Force Materiel Command Wright-Patterson AFB, OH 45433-7251	AFRL-PR-WP
	11. SPONSORING/MONITORING AGENCY REPORT NUMBER(S) AFRL-PR-WP-TM-2006-2177

12. DISTRIBUTION/AVAILABILITY STATEMENT
Approved for public release; distribution is unlimited.

13. SUPPLEMENTARY NOTES
Report contains color.

PAO Case Number: AFRL/WS 06-0876, Clearance date: 06 Apr 2006.

14. ABSTRACT

The initial charge of the DUST Program was to provide technical support to the development of inductive components for power electronics and integrated circuits where the driving forces for future improvement are size, frequency, and temperature. The CMU program was charged with examining amorphous and nanocomposite materials for inductive components. For these magnetic components the following figures of merit were identified for new materials development: 1) Induction: 1 to 2 T (5 to 10 times that of conventional ferrites at room temperature); 2) Frequency: 200 kHz to 1 MHz; 3) Temperature: 200 °C and above. The goals of the DUST project were to develop composition, structure, and magnetic properties relationships in three areas for use in inductive components. These three areas of pursuit were: 1) amorphous precursors to HITPERM materials; 2) Fe-based amorphous materials; 3) HITPERM powders. The HITPERM materials are now felt to be competitive with Fe-based Metglas materials in terms of losses, while offering higher inductions and better high temperature magnetic properties.

15. SUBJECT TERMS

soft magnetic materials, iron cobalt alloys, amorphous and nanocrystalline materials

16. SECURITY CLASSIFICATION OF:			17. LIMITATION OF ABSTRACT:	18. NUMBER OF PAGES	19a. NAME OF RESPONSIBLE PERSON (Monitor)
a. REPORT Unclassified	**b. ABSTRACT** Unclassified	**c. THIS PAGE** Unclassified	SAR	68	John Horwath **19b. TELEPHONE NUMBER** *(Include Area Code)* N/A

Table of Contents

I. Introduction

The initial charge of the DUST Program were to provide technical support to the development of inductive components for power electronic components and integrated circuits where the driving forces for future improvement are size, frequency, and temperature. The CMU program was charged with examining amorphous and nanocomposite materials for inductive components. For magnetic components the following figures of merit were identified for new materials development: (1) Induction: 1 - 2 T (5-10 times those conventional ferrites at RT); (2) Frequency: 200 kHz - 1 MHz; (3) Temperature: 200 ^{0}C and above. The ultimate goal was to determine whether the materials would meet needs of Boeing for converter circuits of interest.

Magnetic core components targeted for study were (1) Laminates where it was thought that amorphous laminates could potentially benefit from planar flow casting. (2) Tape Cores where new Metglas derivatives and amorphous precursors to HITPERM could offer superior high temperature properties and (3) Powder Cores where powdered HITPERM nanocomposites might provide a high temperature analog to Sendust currently being produced under the Spang Tradename KoolMu.

The goals of the DUST project were to develop composition, structure, magnetic properties relationships in three areas for use in inductive components. The materials were tested for viability in tape wound and powder cores. These three areas of pursuit were:

(1) **Amorphous Precursors to HITPERM Materials:** New variations on the CMU developed HITPERM compositions $(Fe_{1-x}Co_x)_{88}M_7B_4Cu$ and $(Fe_{1-x}Co_x)_{89}M_7B_4$ (M = Zr, Nb) were studied. Results of these studies are summarized here and have been reported on in the CMU Materials Science and Engineering Department thesis of Frank Johnson. Frank's work has been published in several archival journals as detailed below.

(2) **Fe-based Amorphous Materials:** Derivatives of Metglas materials were investigated as detailed in the body of the document. Results of these studies are summarized here and will be reported on in the CMU Materials Science and Engineering Department thesis of Chang-yong Um. Chang-yong's work has been published in archival journals as detailed below.

(3) **HITPERM Powders:** CMU in collaboration with Magnetics, Inc. has produced nanopowders of the HITPERM materials.

The work was extended to include study of nanocrystalline ferrite materials through matching funding by the CMU Institute for Complex Engineered Systems (ICES) with funds provided by the State of Pennsylvania. This work is also summarized below and is reported in the CMU Materials Science and Engineering Department thesis of Raja Swaminathan.

In the following is offered a report of the major results, research output and developments for each of these sub-tasks following the details as given in the DUST Statement of work and the CMU ICES project on ferrite nanoparticles. The report is organized as follows:

Section I: Introduction
Section II: Research Output and Ancillary Program Support
Section III: Programmatic Milestones
Section IV: Appendices

II. Research Output and Ancillary Program Support

In this section is detailed the major research output from the DUST program. Table II.1 summarizes the personnel contributing to the efforts of the DUST project. The faculty members M. E. McHenry, D. E. Laughlin and D. N. Lambeth and graduate student Chang-yong Um were all directly supported by the DUST project. Frank Johnson's work was supported through an NSF fellowship with research funding provided by the DUST program. Others received partial support from the project or worked on projects with related research. Suk-Joon Son was supported through a no-cost extension to the CMU MURI program.

Faculty

    M. E. McHenry   D. E. Laughlin   D. N. Lambeth - 2 years.

Student - Graduate

    F. Johnson (co- with NASA)   → NIST post-doc 02/04
                                        → General Electric CRD 07/05
    C. -Y. Um   → due to defend 2005/2006
    S. Son (MURI NCE)   → Samsung, Korea
    R. Swaminathan (ICES)   → Intel, Pheonix
    P. Ohodnicki (NDSEG Fellowship) → CMU

Students - CMU Undergraduate (CMU SURG, ICES, IFYRE, MRSEC)

    J. McKinley → Univ. Michigan   R. Gallagher → U.S. Steel
    J. Hess → Boeing (NASA)   M. Lucas → Caltech
    J. Woods → NRL SU REU → CMU   D. Chan → CMU
    M. Simone --> U.Va → CMU   C. Manganello → CMU
    N. Lippa → CMU   Y. Hanlumyuang → CMU
    N. Hayward → CMU

Students - REU (ICES, MRSEC)

    R. Rencewicz (U. Pittsburgh)   J. Barrow (Fla. A&M)
    R. Jacobs (Cal. State Northridge)   R. Gordon (Fla. A&M)
    S. Nayer (Cal. State Northridge) → CMU

Post-docs, Visiting Scientists, Visiting Faculty

    H. Okumura (DSSC)   → Faculty Kyoto University
    M. Sorescu   → Duquesne
    V. Keilin (Spang/ARL)   → to begin CMU Ph.d program 2005/06

Table II.1: Personnel contributing to the efforts of the DUST project.

Programmatic goals were supported by developments in programs funded by the National Science Foundation, CMU ICES and CMU MRSEC programs. Many of the undergraduate students who have worked with the project have moved on to top graduate schools or industrial positions. Table II.2 summarizes other direct or in-kind support for the DUST project. Without this additional support from many other sources the results of the DUST program would have been substantially diminished.

NASA Glenn Fellowship: Frank Johnson
NDSEG Fellowship: Paul Ohodnicki
National High Field Magnet Lab: Field Annealing (Hamid Garmestami)
Naval Research Lab: Matt Willard,Technical Support (Ferrites, Loss Models)
Wright Patterson AFB: Zafer Turgut, Technical Support (RF Plasma torch)
NIST: Support for Hide Okumura
CMU Data Storage Systems Center (DSSC): Support for Hide Okumura
CMU Institute for Complex Engineered Systems: Support for Raja Swaminathan, and REU from Univ. Pittsburgh
CMU MRSEC Undergraduate REUs from CMU, FLA A&M, CSUN Nanoindentation
CMU SURG   Undergraduate REUs from CMU
Sarah Lawrence College: Scott Calvin, EXAFS (and V. Harris, Northeastern)
Duquesne University: Sabbatical support for Monica Sorescu
National Research Institute for Materials (NRIM), Japan: K. Hono and T. Ohkubo. Atom Probe Field Ion Microscopy (APFIM).

Table II.2 Other substantial direct or in-kind support for the DUST project.

Personnel in the DUST program won several research competitions and awards during the duration of the program. These are summarized in Table II.3

F. Johnson was awarded NASA fellowship for graduate studies.
F. Johnson was awarded 2004-2005 NRC post-doctoral fellowship at NIST.
M. E. McHenry won the 2003 Professor Philbrook Award in the MSE Dept. at CMU for Excellence in Teaching.
J. Hess won the 2003 Pittsburgh Section ASM's Young Member night UG poster competition.
J. Hess was awarded a Boeing scholarship for UG studies.
R. Swaminathan won 3rd prize the 2003 ASM's Young Member night Grad poster competition.
R. Swaminathan was awarded 2004 MMM Jacksonville Graduate Travel Grant.
J. Woods won 2nd prize in the 2005 CMU Intel First Year Research Experience (IFYRE) competition.
D. Chan, 2nd Place Undergraduate, ASM Young Members Night, Pittsburgh Chapter, Feb. 2005.
D. Chan was presented the "Past Chairpersons' Education Assistance award at the Annual Young Member's Night of the Pittsburgh Golden Triangle Chapter_of ASM International.
Y. Hanlumyuang will performed Carnegie Institute of Technology (CIT) Honors research in 2005-2006 and won a MMM conference travel award to present his research in San Jose, CA in November, 2005.
M. Simone performed CIT Honors research in 2005-2006.
P. Ohodnicki was awarded NDSEG fellowship for graduate studies.

Table II.3: Awards to CMU DUST program participants.

As stipulated by the DUST contract technical information was communicated through quarterly research meetings and reports which are summarized in Table II.4. In addition to the contract mandated technical reviews CMU had approximately biweekly research group meetings in the group of M. E. McHenry. The research was also disseminated in the following oral presentations at Carnegie Mellon University:

> **Public Doctoral Thesis Presentations:** S. Son, F. Johnson and R. Swaminathan
> **Thesis Overviews:** F. Johnson, R. Swaminathan, and C. -Y. Um
> **MSE Dept. Research Presentations:** F. Johnson, R. Swaminathan, and C. -Y. Um
> **DSSC Research Presentation:** H. Okumura

Participants in the research published articles in archival journals that are listed in Appendix I. These are available as pdf files on the website of M.E. McHenry at CMU.

Meetings		Reports		
Sept.	**13, 2002 - Magnetics, Inc. (Kickoff)**	**Oct.**	**11, 2002**	**Y1Q1**
Jan.	**10, 2003 - CMU**	**Jan.**	**11, 2003**	**Y1Q2**
Mar.	**25, 2003 - CMU**	**Apr.**	**28, 2003**	**Y1Q3**
Jul.	**31, 2003 - Magnetics**	**Aug.**	**12, 2003**	**Y1Q4**
Oct.	**21, 2003 - CMU**	**Nov.**	**17, 2003**	**Y2Q1**
Mar.	**09, 2004 - CMU**	**Mar.**	**12, 2004**	**Y2Q2**
	(Mar. 09, 2004)	**Apr.**	**29, 2004**	**Y2Q3**
Jun.	**28, 2004 - CMU**	**Jul.**	**08, 2004**	**Y2Q4**
Oct.	**01, 2004 - CMU**	**Dec.**	**01, 2004**	**Y3Q1**
Jan.	**14, 2005 - CMU**	**Feb.**	**01, 2005**	**Y3Q2**
Apr.	**21, 2005 - CMU**	**May**	**13, 2005**	**Y3Q3**
Aug.	**12, 2005 - WPAFB**	**Final Dec. 2005**		**Y3Q4**

Table II.4: Research communication between the participants.

The DUST program used a variety of technical equipment and facilities. Some of these were purchased in the previously funded MURI program and others are central facilities in the Materials Science and Engineering Department at Carnegie Mellon University. The facilities and apparatus employed in the DUST program are summarized in Appendix II.

Low-loss Himalloy alloys (MURI support) and further investigated in the DUST program were the subject of CMU Disclosure 03-040. Carl Mahler Senior Project Manager of CMU's Innovation Transfer Center set up a MTA for Himalloy materials.

III. Programmatic Milestones

This section gives a summary of the compliance with the program milestones and the major results achieved in each of four areas:

III.1   Amorphous Precursors to HITPERM Materials.
III.2   Fe-based Amorphous Materials.
III.3   HITPERM Powders.
III.4   Nanocrystalline Coatings and Inductive Devices Produced by RF Plasma Synthesis.

These are discussed in this order rather than the order stated in the DUST proposal.

The major results of the Task involving amorphous precursors to HITPERM materials was the determination of the importance of field induced anisotropy on the determination of losses in these materials. This effort has been successfully transitioned to Magnetics, Inc. who have now commissioned a state of the art field annealing furnace. This is now being used as a tool in a follow-up Army Research Laboratory project that CMU is participating in as a subcontractor. CMU has also successfully proposed follow-up funding to study the fundamentals of field induced anisotropy from the National Science Foundation. Materials first conceived in the predecessor MURI project and further developed in the DUST project have been transitioned to Magnetics, Inc. for pilot plant scale-up. This task and NASA funding provided the support for the CMU Ph.d thesis of Frank Johnson. This work has also resulted in refinement of and a more complete understanding of nanocrystallization kinetics in important nanocomposite sytems. This includes the phenomenon of chemical partitioning during nanocrystallization. *The HITPERM materials are now felt to be competitive with Fe-based Metglas materials in terms of losses, while offering higher inductions and better high temperature magnetic properties.*

The major results of the Task involving Fe-based amorphous materials has been to develop new materials in the series $Fe_{82-x}Co_xNb_3Ta_1Mo_1B_{13}$, that have since been demonstrated to rival the losses of FINEMET at frequencies exceeding 500 kHz. The best soft magnetic properties have been observed in an alloy of composition $Fe_{82-x}Co_xNb_3Ta_1Mo_1B_{13}$ (x = 21.5). These Fe-based amorphous materials have also been transitioned to Magnetics, Inc. for pilot plant scale-up. The crystallization products of $Fe_{82-x}Co_xNb_3Ta_1Mo_1B_{13}$ ($0 \leq x \leq 41$) amorphous alloys have been studied in great detail. In particular, the importance of an $Fe_{23}B_6$-based secondary crystallization product has been noted. Stabilizing the amorphous structure with respect to the formation of this phase is important in developing both bulk amorphous and nanocomposite materials with excellent high temperature magnetic properties. *New Fe-based amorphous material with higher inductions and better high temperature magnetic properties are likely to compete with FINEMET at f >500 kHz.*

The major results of the Task involving HITPERM powders included identifying the notable propensity for Al and Si to embrittle these materials making them easy to powder for powder core applications. The large inductions of the HITPERM materials make them interesting for powder core applications. *A more detailed analysis of the compositional dependence of losses is necessary to further develop these materials.*

The major results of the ICES PITA project included determining a roadmap for producing planar ferrite inductive components utilizing an RF plasma torch. The thesis of Raja Swaminathan and publications describing the work include a new model for the plasma gas phase nucleation and growth of ferrite nanoparticles. This model offers new insights into nanoparticle shape and surface morphology. Raja's work also concludes that low temperature sintering is possible with nanoparticles and that the nanocrystalline size can be retained in a dense compact. Decomposition reactions in high temperature sintering have also been identified. *We recommend that these significant new results be transitioned into new applications for microwave ferrites.*

III.1 Amorphous Precursors to HITPERM Materials.

The statement of work items and their timeline for the DUST task on developing Amorphous Precursors to HITPERM Materials is shown in Table III.1. Major results for this task are detailed in this section. This work was the thesis project of Frank Johnson who was partially supported by a NASA graduate fellowship. Frank was awarded his Ph.d in 2003 and went on to post-doc at NIST. He has since been hired by General Electric. His current contact information is:

> GE Global Research
> 1 Research Circle, MB-241, Niskayuna, NY 12309
> T 518 387 5087   F 518 387 6232
> johnsonf@ge.com

Microstructural characterization work was also supported by the efforts of post-doctoral associate Hide Okumura who was supported by NIST and the CMU Data Storage Systems Center. Hide returned to Japan to take a faculty position at Kyoto University. Visiting scientist T. Ohkubo, supported by the CMU DSSC, also aided with microstructural characterization. He has returned to the National Research Institute for Metals in Japan. He and the group of Kazuhiro Hono have continued to explore new HITPERM based alloys by atomic probe field ion microscopy (APFIM).

Work extending the results of this project have continued through the support of Jianguo Long who is supported through new NSF funding to study crystallization kinetics and field induced anisotropy in FeCo-based amorphous materials (beginning July 1, 2004). The proposal funded is entitled "Nanocrystallization Kinetics and Induced Anisotropy in Soft Magnetic Nanocomposites", NSF DMR-0406220, with Prof. McHenry and Laughlin serving as Principal Investigators. Paul Ohodnicki, who received his B. S. form the University of Pittsburgh, accepted a position to work on this project and began in June, 2005, funded by an NDSEG fellowship. Magnetics, Inc. has also received funding from the Army Research Laboratory to continue the development of these alloys for high temperature converter circuits. CMU is a subcontractor to this contract. It is funding the work of Vladimir Keilin that is focused on transferring planar flow casting technology to a pilot caster at the Magnetics, Inc. research facility.

Amorphous Precursors to HITPERM Materials			
Materials Synthesis – Chemistry Determination	X	X	X
Structural Characterization	X	X	
Magnetic Characterization	X	X	X
Magnetostriction Measurements		X	X
Crystallization Kinetics		X	
Tapes to Magnetics, Inc. for Cores		X	X
Properties measurements of tape cores		X	X
Communicate Results to Boeing (Supply Cores if viable and competitive)		X	X
Report Results			X

Table III.1: Statement of work for DUST task: Amorphous Precursors to HITPERM Materials.

HITPERM is an FeCo-base nanocomposite soft ferromagnetic alloy. It was first developed as part of the predecessor MURI program and initial developments are summarized in the thesis of Matt Willard and reviewed in reference 1. As originally conceived it had a nominal composition

of $(Fe_xCo_{1-x})_{89}M_7B_4$ (M = Zr, Nb, Hf) and its structure is composed of nanocrystalline B2 ordered FeCo grains embedded within an amorphous matrix. Its soft magnetic properties result from its nanocrystalline grain size, as predicted by the Random Anisotropy Model as originally proposed by Herzer[2]. HITPERM is distinguished from other nanocomposite alloys by its high amorphous phase Curie temperature. This allows nanocrystalline grains to remain exchange coupled to 600 °C or higher, which has been further elaborated in the thesis of Frank Johnson[3]. This work built upon the original research of Matt Willard[4] in developing new alloy compositions for a variety of programmatic and development goals. This new alloy development is described below along with a summary of new research findings which have helped to advance the field of amorphous and nanocomposite magnets. The state of the field at the beginning of the DUST program is summarized in the CMU Ph.d thesis of Frank Johnson. In particular, worldwide research immediately prior to the DUST program and during the program are summarized in ref. 5-14.

III.1.1 Materials Synthesis – Chemistry Determination

Suzuki[5] summarized the design of nanocomposite alloys by separating the elemental components into four categories. Suzuki presented the matrix:

$$\begin{bmatrix} \overset{FM}{Fe} & Co & Ni \end{bmatrix}_{66-91} \begin{bmatrix} \overset{EM}{Ti} & V & Cr \\ Zr & Nb & Mo \\ Hf & Ta & W \end{bmatrix}_{2-8} \begin{bmatrix} \overset{ML}{B} & C \\ Al & Si & P \\ Ga & Ge \end{bmatrix}_{2-31} \begin{bmatrix} \overset{LM}{Cu} \\ Ag \\ Au \end{bmatrix}_{0-1} \qquad (3.1)$$

where **FM** denotes **F**erromagnetic transition **M**etals, EM denotes **E**arly transition **M**etals, ML denotes **M**eta**L**loid elements, and LM denotes **L**ate transition **M**etals. The FM elements provide the magnetic properties, the EM and ML elements act as glass-formers and grain refiners, and the LM elements act as nucleation agents in forming the nanocomposite state. This serves as a template for describing the further development of HITPERM alloys during the DUST program.

Frank Johnson made the following class of alloy modifications to HITPERM alloys in order to further improve their properties and/or develop a more fundamental understanding of these materials. These alloy modifications included:

(1) New EM substitutions (Nb, Ta, Cr, and Mo) to influence the stability of the amorphous phase as well as to promote casting in air without excessive oxidation.

(2) Cr substitution for FM to reduce the amorphous phase Curie temperature to allow for fundamental studies of the decoupling of nanoparticles above the amorphous phase Curie temperature.

(3) Variation of the Fe:Co FM ratio in HITPERM alloys to optimize the amorphous phase Curie temperature, and inductions, and magnetostriction coefficients of the amorphous and nanocrystalline phases in these nanocomposite materials.

(4) Evaluation of Al and Si as a low-cost metalloid species and for potential benefit in reducing the magnetostriction coefficients in analogy with Sendust alloys.

(5) Evaluation of the necessity of the nucleation agent for developing the nanostructure.

Amorphous alloy precursors to HITPERM alloys of composition $(Fe_{1-x}Co_x)_{88}M_7B_4(Cu)$ (M = Nb, Zr, Hf, Cr, Ta, Mo), with x in atomic percentages ranging from 20 to 70 were investigated for tape wound cores. Initial analysis included a benchmarking of the chemical composition of base HITPERM alloys by Magnetics. This baseline chemistry was determined by an inductively-coupled-plasma (ICP) analysis on three HITPERM runs. Results are detailed in Table III.1.1. The results were used to verify nominal compositions. The Nb, Ta, Cr, and Mo modifications had not been investigated in previous studies of HITPERM.

Sample ID	Element (Atomic %)	Fe	Co	Zr	Nb	Al	B	Si	C	S	O_2	N_2
CMU 81	Target	44.5	44.5	7			4					
	Analysis	42.989	43.546	8.512		0.408	4.075	0.196	0.215	0.002	0.045	0.012
CMU 91	Target	42.75	42.75	2	4		8					
	Analysis	42.631	42.964	2.083	4.030	0.207	7.756	0.199			0.073	0.056
CMU 102	Target	44.5	44.5	7		2	2					
	Analysis	43.964	43.864	7.840		2.296	1.563	0.200	0.155	0.002	0.088	0.028

Table III.1.1: Chemistry determination on 3 runs of amorphous precursors to HITPERM.

The research of Frank Johnson showed the Curie temperature of the amorphous phase precursor to HITPERM to be reduced by the addition of Cr.   While this is technically deleterious to high temperature properties it was possible to use this to lower the Curie temperature to near room temperature so as to make study of decoupling phenomena possible. Small Cr additions are also thought to have some benefit in improving corrosion resistance in these alloys. This will be the subject of future studies in alloy development. The low temperature decoupling is also useful in new generations of materials being investigated for their magnetocaloric effects.

Fe:Co in the 65:35 ratio has the highest saturation induction and Curie temperature, whereas the 50:50 ratio has a minimum in magnetocrystalline anisotropy. The original HITPERM alloys were produced in the 50:50 ratio to minimize loss due to anisotropy. In this work, a new series of 65:35 ratio HITPERM alloys were produced. The compositions produced are summarized in Table III.1.2 along with the technically important primary crystallization temperatures, T_{x1}, and the $\alpha \rightarrow \gamma$ structural phase transformation temperature of the nanocrystalline phase. These significance of these transition temperatures is discussed further in the sections below. Core loss measurements indicated that the 65:35 alloys have higher core loss than similar 50:50 alloys, but higher inductions and amorphous phase Curie temperatures.

Composition (atomic %)	Description	T_{x1} (°C)	$T_{\alpha-\gamma}$ (°C)
$Fe_{57.2}Co_{30.8}Zr_7B_4Cu_1$	Fe:Co 65:35	475	980
$Fe_{44}Co_{44}Zr_{5.7}B_{3.3}Ta_2Cu_1$	Ta-Mod	480	968
$Fe_{44}Co_{44}Zr_{5.7}B_{3.3}Mo_2Cu_1$	Mo-Mod	463	939
$Fe_{44}Co_{44}Zr_7B_4Cu_1$	HITPERM	480	985

Table III.1.2: Comparison of primary crystallization temperatures and α-γ transition temperatures for 50:50 Fe:Co base HITPERM and 3 modifications: 65:35 Fe:Co, Ta-modified, and Mo-modified[3].

New alloys were produced with Al-Si compositions were chosen in an attempt to control the magnetostriction and resistivity of the resulting alloy by following a philosophy similar to that used in producing ternary Fe-Si-Al Sendust alloys. These alloys were $Fe_{43}Co_{43}Al_1Si_2Zr_7B_4$, $Fe_{41.5}Co_{41.5}Al_2Si_4Zr_7B_4$, $Fe_{40}Co_{40}Al_3Si_6Zr_7$ B_4 , $Fe_{38.5}Co_{38.5}Al_4Si_8Zr_7B_4$ and $Fe_{37}Co_{37}Al_5Si_{10}Z_7B_{4.}$ These followed published reports of Fe-Zr-B-Si and Fe-Zr-B-Al NANOPERM alloys exhibiting zero magnetostriction (A. Inoue, Materials Science Forum 225-227, ser. 2, 639-48, (1996)). Al and Si are also used as metalloid glass formers. Only the sample with the least amount of Al and Si was

cast successfully into the amorphous state. The other crystalline materials were concluded to be suitable for processing into powder cores because of their brittleness.

A conclusion of the DUST program is the relative unimportance of the addition of a nucleation agent for developing the nanostructure in HITPERM alloys. These conclusions were first proposed after the Atomic Probe Field Ion Microscopy (APFIM) studies in collaboration with K. Hono's group. Ping et al.[16] examined both Cu containing and non-Cu-containing HITPERM ($Fe_{44}Co_{44}Zr_7B_4Cu_1$ and $Fe_{44.5}Co_{44.5}Zr_7B_4$) with 3-Dimensional Atom Probe (3DAP). They found no evidence of Cu clusters during crystallization. They postulated that this was due to the less positive heat of mixing between Co and Cu than Fe and Cu. This provides less driving force for rejection of Cu from the amorphous phase. Ping et al. also showed that Fe and Co do not segregate equally between the crystalline and amorphous phases in $Fe_{44}Co_{44}Zr_7B_4Cu_1$. The crystalline phase had an Fe concentration of 58 atomic % and a Co concentration of 37 atomic %. The amorphous phase had an Fe concentration of 34.5 atomic % and a Co concentration of 49.9 atomic percent. Thus, the amorphous phase is enriched in Co, and depleted in Fe. New results on alloys with EM = Nb and ML = Ge have observed some Cu clustering but not at sufficient enough concentrations to explain copious nucleation in these alloys. This work has recently been completed on alloys synthesized by J. Long as part of a new NSF program.

At the conclusion of his thesis Frank Johnson demonstrated that the core loss of HITPERM was comparable to a commercially available $Fe_{49}Co_{49}V_2$ alloy. Core loss was reduced by compositional modification and by field annealing. Microstructural studies of Zr-containing HITPERM in his thesis showed Zr to be depleted near the surface of the as-cast ribbons that was suggested to be the cause of a crystalline layer in this region. Partially crystallized ribbons display a uniform grain size distribution on both sides of the ribbon. Cu was determined not to be necessary as a nucleation agent during crystallization. Zero-field reannealing of the field annealed and field crystallized samples was used to identify that a structural cause other than crystalline texture contributes to induced anisotropy.

Jianguo Long is continuing efforts on some new HITPERM compositions in support of the Magnetics, Inc. funded subcontract effort as part of an Army Research Laboratory (ARL) contract and their fundamental properties with NSF support at CMU. Jianguo is currently studying magnetic, thermal and structural properties of FeCoNbBGeCu alloys. Vladimir Keilin joined the group in February, 2005 to begin scale-up efforts at Magnetics, and funded by the Army contract. He has helped Magnetics, Inc. to implement planar flow casting technology for use in producing wide ribbons. He is pursuing alloy modification on the pilot plant caster at Magnetics. Paul Ohodnicki, began work on the project beginning in June, 2005 funded by an NDSEG fellowship. He is exploring Mn substitutions in HITPERM alloys and has recently published a model for the effects of large magnetic fields on phase equilibria in the FeCo system.

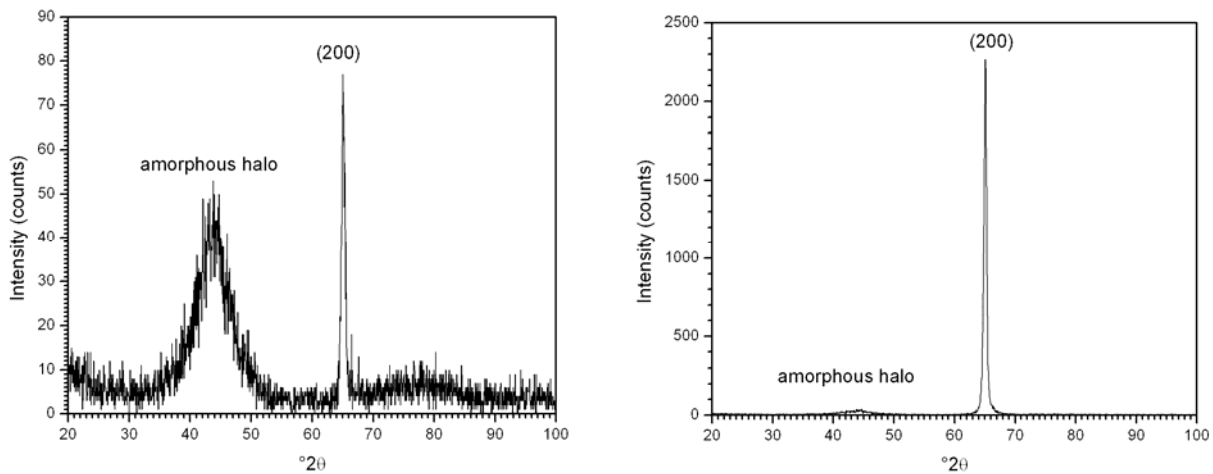**III.1.2 Structural Characterization**

Structural characterization of as cast and nanocomposite alloys were routinely performed by x-ray diffraction. Selected samples were studied by transmission electron microscopy and high resolution transmission electron microscopy. Atomic Probe Field Ion Microscopy (APFIM) studies of K. Hono's group were used to examine local chemical partitioning in the nanocrystallization process. Crystallization kinetics studies based on in-situ hot stage high resolution TEM (HRTEM) of HITPERM amorphous precursors were performed by Hide Okumura and discussed below.

X-ray diffraction studies revealed the phases present in surface crystallization, those which developed after primary nanocrystallizaton and those which resulted from the secondary

crystallization experiments. The details of these numerous studies are summarized in the thesis of Frank Johnson. A few of the more notable results include:

(1) The universal observation of the BCC phase as primary nanocrystallization product. This phase has been previously shown by synchrotron XRD studies to be ordered.

(2) The observation of (200) texture of nanocrystallites on the roll and surface sides of as-cast ribbons.

(3) Observation of new secondary crystallization products in several alloy systems.

X-Ray diffraction (XRD) was performed with x-rays incident on either the roll and surface sides of as-cast ribbons to look for the (200) crystalline texture that is often observed in nanocrystalline ribbons.[15] Figure III.1.1 shows the x-ray diffraction patterns of the surface and roll sides of an as-cast HITPERM ribbon. The surface side shows a strong (200) reflection, indicating strongly textured nanocrystals. The crystalline occurs with a lower volume fraction on the roll side.

Figure III.1.1: X-ray diffraction pattern of roll side (left) and surface side (right) of as-cast HITPERM ribbon.

During secondary crystallization, the residual amorphous precursor to HITPERM destabilizes and several stable and metastable $FM_2(EM,ML)$ and $FM_{23}(EM,ML)_6$ phases can precipitate (FM, EM, and ML refer to the elemental groupings in Equation 3.1). The $FM_{23}(EM,ML)_6$ is sometimes called a metastable $FM_3(EM,ML)$ phase in the literature. The binary $FM_{23}(ML)_6$ and $FM_{23}(EM)_6$ phases both have space group 225 with Pearson symbol cF116, but with atoms occupying different special positions in the structure. $Fe_{23}Zr_6$ is isostructural with the $Mn_{23}Th_6$ structure and $Fe_{23}B_6$ is isostructural with the $Cr_{23}B_6$ structure, respectively. Figure III.1.2 illustrates the building of the $Fe_{23}Zr_6$ structure from constituent atoms. These $FM_{23}(EM,ML)_6$ phases are also observed as crystallization products of some of the Fe-based metallic glasses that were studied in the DUST program and detailed in Section III.2. The ordering of the smaller ML and larger EM atomic species on the sublattices in ternary systems is still an open question and being actively studied in the thesis research of Chang-yong Um, Jianguo Long and Paul Ohodnicki.

When the residual amorphous phase no longer exists as a barrier to grain growth, grain coarsening occurs. Secondary phases themselves have undesirable magnetic properties (high anisotropy, low magnetization and Curie temperatures). Thus, in the design of nanocomposite alloys, secondary crystallization is to be avoided and T_{x2} serves as an upper operating temperature limit. Unique secondary crystallization products were observed in a $Fe_{44.2}Co_{23.8}Cr_{20}Zr_7B_4$ alloy.

Along with the ubiquitous BCC primary crystallization products, a tetragonal phase was observed as a secondary crystallization product.
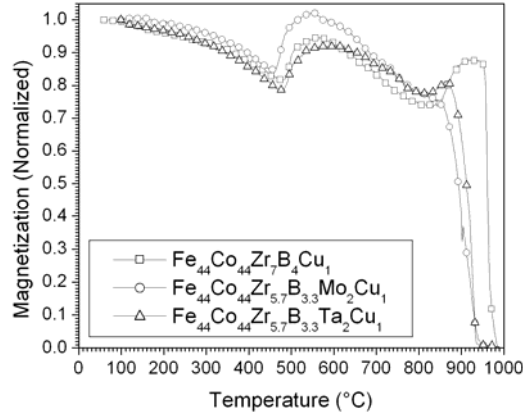

Figure III.1.2: $Fe_{23}Zr_6$ structure built from constituent atoms (a) Zr octahedra with larger ocathedra centered by Fe (black) at one of four special positions (b) addition of Fe atoms (yellow) at a second special position, (c) addition of Fe atoms (red) at a third special position, and (d) final addition of Fe atoms (brown) at a 4th special position.

III.1.3 Magnetic Properties Characterization

An important tool in the magnetic characterization of all amorphous and nanocomposite materials studied in the DUST program was thermomagnetic measurements performed on a Lakeshore vibrating sample magnetometer equipped with a 1000 ^{0}C furnace. These measurements were used to identify the Curie temperatures of amorphous precursors and nanocrystalline phases, the $\alpha \rightarrow \gamma$ structural phase transformation temperature of the nanocrystalline phase, and the primary and secondary crystallization temperatures, T_{x1} and T_{x2}. Figure III.1.3 illustrates thermomagnetic data for alloys described in Table III.1.2.

The Torque Magnetometry option of the CMU Quantum Design Physical Properties Measurement System (PPMS) was used to measure the magnetic anisotropy present in the field annealed HITPERM samples. Four samples were measured: amorphous, zero-field-crystallized, zero-field-crystallized-than-field-annealed, and field-crystallized. Torque curves as a function of angle were determined. Measured anisotropy energy densities and angular positions of the easy axes (relative to the zero position of the cantilever) were determined. The measured anisotropy was uniaxial and field annealing was observed to reduce the magnitude of the anisotropy. This was coupled with a similar decrease in the magnitude of the core loss. The source of the large, uniaxial anisotropy was postulated to be the coupling of the magnetostrictive effect with residual

strain due to crystallization. This leads to a magnetoelastic anisotropy that was shown to the same order of magnitude of the measured anisotropy.
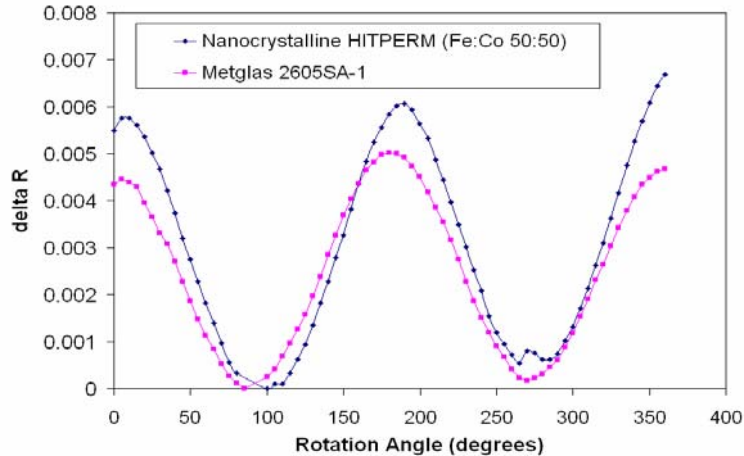

Figure III.1.3: M(T) for base, Mo- and Ta-modified HITPERM. Measurements were made on a VSM at a constant field of 42 kA/m (525 Oe) while sweeping temperature from 100-1000 °C at a constant rate of 2.2 °C/min. All curves normalized to magnetization at 100 °C.

Other physical properties measurements included amorphous HITPERM samples, of compositions: $Fe_{44.5}Co_{44.5}Zr_7B_4$, $Fe_{53.95}Co_{29.05}Cr_5Zr_7B_4$, and $Fe_{54}Co_{31.5}Mn_{4.5}Zr_6B_4$ that were sent to Z. Turgut at UES/WPAFB for high temperature resistivity measurements.

III.1.4 Magnetostriction Measurements

A collaborator from our MURI program, Dr. V. Franco provided preprints of his work entitled "The Evolution of Coercivity with Temperature in the Early Stages of Nanocrystallization in FeCoNbB(Cu) Alloys."; which provided a model for coercivity mechanisms based on magnetostriction in amorphous precursors to and partially nanocrystallized HITPERM materials. This motivated our exploration of magnetostriction in our alloys.

Figure III.1.4: Magnetostriction as a function of angle for a HITPERM and Metglas alloys.

A strain gage technique was selected to measure magnetostriction in HITPERM alloys. A difference in resistance between a gage attached to a sample and a reference gage was measured as a differential voltage across a Wheatstone bridge. The low strains associated with

12

magnetostriction requires a measurement technique sensitive to a level of 1-10 microvolts. At this level noise interference was a significant issue. To address this a simple waveform generator was constructed with a 555 timer and a 9V battery. The generator and the bridge was built into a shielded aluminum box. Initial work was done using a high field electromagnet with the signal across the bridge was measured with a lock-in amplifier. The magnetostriction effect caused the generated waveform to appear across the bridge.   Typical data is shown in Figure III.4

Subsequent studies were performed using a Quantum Design Physical Properties Measurement System (PPMS) to rotate the sample in a saturating field while measuring the change in resistance across the bridge due to strain. Figure III.3 shows an example curve. The magnetostrictive constant of Metglas 2605 SA1 was measured at 30 ppm, within 10 % of the published value of 27 ppm. Measured magnetostriction for two HITPERM alloys, both in as-cast and crystalline states, are presented in Table III.1.3.

Composition	Condition	λ_s (ppm)
$Fe_{44.5}Co_{44.5}Zr_7B_4$	As-cast (amorphous)	37
$Fe_{44.5}Co_{44.5}Zr_7B_4$	Annealed (nanocrystalline)	25
$Fe_{42.75}Co_{42.75}Zr_2Nb_4B_{8.5}$	As-cast (amorphous)	54
$Fe_{42.75}Co_{42.75}Zr_2Nb_4B_{8.5}$	Annealed (nanocrystalline)	32

Table III.1.3: Measured magnetostriction values for some HITPERM alloys.

Results of magnetostriction measurements were interpreted as suggesting that the HITPERM alloys exhibit a longitudinal, uniaxial anisotropy that is magnetoelastic in origin. To the extent that alloy modifications can reduce these magnetostriction coefficients, the ease for which tranverse induced anisotropy can be engendered by field annealing will be increased.

III.1.5 Crystallization Kinetics

Crystallization kinetics studies based on in-situ hot stage high resolution TEM (HRTEM) of HITPERM amorphous precursors were performed by Hide Okumura. When an as-spun amorphous HITPERM ribbon was slowly heated from a room temperature in the CMU JEOL JEM2000-EXII using an in-situ hot stage TEM sample holder, a slow clustering process was observed to begin below 350°C with a cluster size less than 5 nm. When the sample temperature approached to ~370°C, crystallization bursts of FeCo nanocrystals were observed due to instantaneous nucleation event. Some nanocrystal sizes quickly reached > 30 nm (less than 5 minutes).   In the early stages of crystallization chemical partitioning was observed to be significant with the retained amorphous matrix with constantly changing chemical composition.

A model (corroborated by APFIM studies) was that Zr and B were expelled homogeneously into the amorphous matrix.   In less than 10 min. the nucleation event is completed followed by relatively slow grain growth and relaxation of atomic positions involving relatively slow diffusive processes. It was noted that there were a significant number of planar defects in the nanocrystals even after a long holding of the sample at higher temperatures (up to 500°C for 30 min.). Isolated FeCo nanoparticles with crystallographically oriented facets surrounded by amorphous matrix were often found even at the latter stage of the heating. Facetted crystals were typically not found in samples nanocrystallized prior to thinning for TEM observation. The fact that an active crystallization event takes place below 400°C (some start even around 370°C), that is much lower than a bulk nanocrystallization temperature of ~500°C, is notable. The significantly lower crystallization temperature was thought to be a manifestation

of lower dimensional crystallization processes. 2-d crystallization kinetics has been a theme of recent work by Chang-yong Um on NANOPERM thin films.

III.1.6 Core Loss Measurements of Tape Cores.

Magnetic losses on trial cores were routinely fit using the Steinmetz equation:

$$P = A(B_p)^n f^m, \qquad [3.2]$$

where B_p is the peak induction in T, f is frequency in kHz. The slopes of log-log plots of P(f) will be used to determine m. The exponent n were determined from measurements of losses at peak inductions up to 1 T.   HITPERM cores of composition $Fe_{44.5}Co_{44.5}Zr_7B_4$ and $Fe_{44.5}Co_{44.5}Zr_7B_2Al_2$ were provided to the National Magnet Laboratory for field annealing and field crystallization. The cores were then measured using the Walker AMH-401 Permeameter. Core loss measurements were made across a frequency spectrum of 60 Hz to 1 MHz at peak inductions from 0.1-1.5 T. Selected frequency/peak induction conditions were measured 30 times to gather descriptive statistics about the repeatability of the measurement. In all cases, field annealing was seen to lower the core loss of the alloys (Figure III.1.5). Reannealing the core in zero field increases the core loss in both the field annealed and field crystallized samples, but not to the same level as prior to field annealing. This suggested that a structural change occurred during field annealing to induce a permanent anisotropy in the material.

Figure III.1.5: Core Loss (W/g) of sample CMU81-6. Error bars correspond to 95% confidence intervals with a sample size of 30. Field annealing is seen to reduce core loss at all B_{max}.

A comparison was made between field annealed, crystalline HITPERM and commercially available ferrite materials from Magnetics, Inc. A field annealed sample of $Fe_{44.5}Co_{44.5}Zr_7B_4$ (CMU81-5) and a field crystallized sample of $Fe_{44.5}C_{44.5}Zr_7B_2Al_2$ (CMU102-5). The field annealed sample was initially crystallized in the absence of an external field for 1 hour at 600 °C, then annealed in the presence of a 17 T transverse field for 1 hour at 480 °C. The field crystallized sample was initially in the as cast, amorphous condition, then crystallized in the presence of a 17 T transverse field for 1 hour at 480 °C. Core loss measurements were made on toroidal tape wound cores with a Walker AMH-401 permeameter at room temperature.

Ferrite materials chose for comparison were the K, R, P, and F materials. K material has a µ of 1500 ±25%, R material a µ of 2300 ±25%, P material a µ of 2500 ±25%, and F material a µ of

3000 ±20%. These materials are used for inductors and power transformers, similar to the expected applications for HITPERM. The volume specific core loss data was scanned directly from charts published in the Magnetics, Inc. ferrite catalog.

Figures A1-A8 in Appendix I, present the HITPERM core loss data overlaid directly onto the ferrite core loss charts. HITPERM measurements were only made at flux densities of 1000 and 2000 gauss. In all cases, HITPERM exhibits a larger volume specific core loss than the ferrite materials at comparable frequency and flux density conditions. For example, CMU81-5 exhibits a core loss of 55 mW/cc at 10 kHz, 1000 gauss B_{Max}. F material exhibits a core loss a loss of 10 mW/cc at the same frequency and flux density. HITPERM has a density of 7.8 g/cc and the ferrite materials have a density of 4.8 g/cc. At 10 kHz and 1000 gauss, HITPERM has a core loss of 7.0 mW/g and F material has a core loss of 2.0 mW/g. Hence, on a mass specific basis the core losses are closer but ferrites still are lower overall.

While the losses in the HITPERM cores did not rival commercial ferrite materials, it may be possible to improve them by compositional modifications, production of thinner ribbons, and optimization of field annealing protocol. It has been shown that the HITPERM materials can be driven to higher inductions. Efforts to improve on these losses includes transition to Magnetics, Inc. for planar flow casting to produce thinner ribbons, to optimize a transverse field annealing protocal and to determine high temperature stability of cores with field induced anisotropy.

A commercially produced Supermendur core was supplied by NASA Glenn Research Center for comparison to the HITPERM material. Supermendur is an FeCo alloy with a nominal composition of $Fe_{49}Co_{49}V_2$ (wt %). The core under test was an Arnold 6T4635R1-01 core with a laminate thickness of 1 mil (25.4 µm) and a path length of 9.476 cm. Table III.1.4 presents the core loss comparison for the two cores at a B_{Max} of 0.5 T. The core loss is seen to be comparable at low frequencies and diverge as frequency is increased. Figure III.1.6 compares hysteresis loops of the two materials at 1,000 Hz and 1.5 T B_{Max}. The HITPERM material is observed to have a smaller squareness than Supermendur. This reduction in squareness is more pronounced when the cores are driven to 1.5 T B_{Max} (Figure III.1.6).
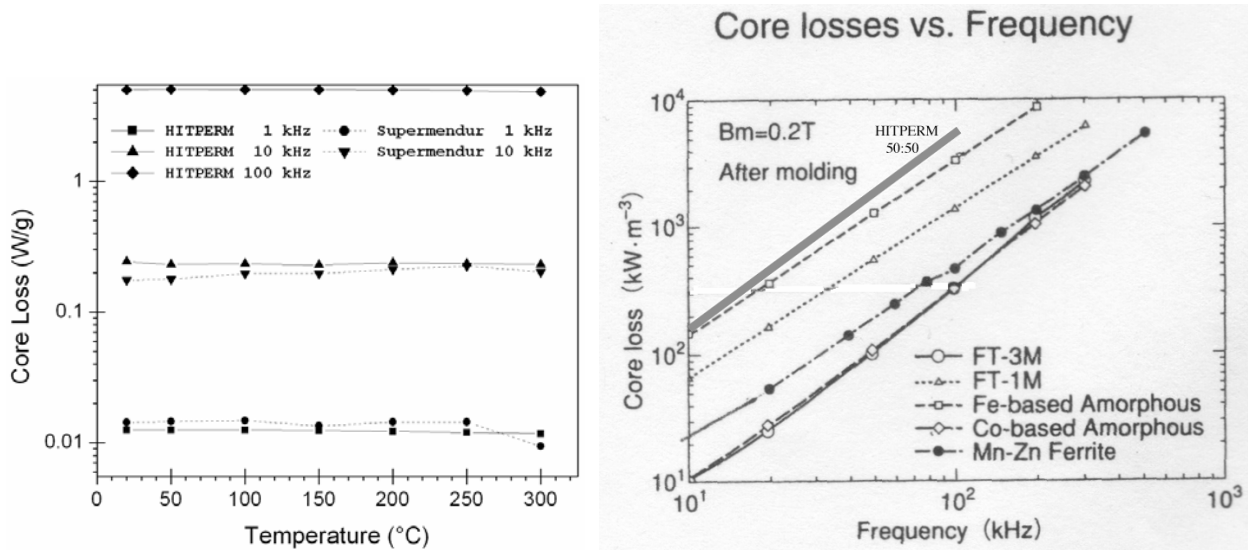
	Nanocrystalline $Fe_{44.5}Co_{44.5}Zr_7B_4$		1-Mil Supermendur ($Fe_{49}Co_{49}V_2$)		Ratio (HITPERM/
Frequency (Hz)	Core Loss (W/g)	Phase Angle (°)	Core Loss (W/g)	Phase Angle (°)	Supermendur)
100	0.00068824	65.831	0.00068206	48.283	1.01
400	0.0040173	48.543	0.002859	36.72	1.40
1,000	0.012909	42.694	0.0080493	34.113	1.60
10,000	0.23492	36.503	0.13038	31.777	1.80

Table III.1.4: Comparison of Nanocrystalline HITPERM core to commercially available 1-Mil Supermendur from 100 Hz to 1.0 kHz.

As reported in the CMU Ph.d thesis of Frank Johnson, the temperature dependence of the AC properties of nanocrystalline HITPERM ($Fe_{44.5}Co_{44.5}Zr_7B_4$) were measured by heating a nanocrystalline core up to 300 °C while measuring core loss with the Walker hysteresisgraph. For comparison, the core loss readings for HITPERM are plotted with those of a 1-mil Supermendur core reported by Weiserman, et al.[17] [W.R. Wieserman, G.E. Schwarze and J.M. Niedra, *Comparison of high temperature, high frequency core loss and dynamic B-H loops of a 2V-49Fe-49Co and a grain oriented 3Si-Fe alloy*, San Diego, CA, USA: Soc. Automotive Eng, 1992.] Plots of core loss vs. temperature are shown in Figure III.1.7 for a maximum induction of 0.5 T at frequencies of 1, 10 and 100 kHz respectively.

Figure III.1.6: Hysteresis loops of Nanocrystalline HITPERM to commercially available Supermendur measured at 400 Hz when driven to 1.5 T B_{Max}.

Figure III.1.7: (a) Specific core Loss vs. Temperature, measured 0.5 T B_{Max}, for nanocrystalline HITPERM ($Fe_{44.5}Co_{44.5}Zr_7B_4$) and Supermendur and (b) comparison of nanocrystalline HITPERM core loss data of Fig. III.1.6 to some commercial Fe- and Co-based amorphous alloys (Hitachi product literature), Mn-ferrites and Finemet alloys, respectively.

HITPERM materials have also been benchmarked at room temperature against some commercial Fe- and Co-based amorphous alloys, Mn-ferrites and Finemet alloys, respectively as illustrated in Fig. III.1.7(b). HITPERM materials with equiatomic Fe:Co ratios have low frequency losses comparable to Fe-based amorphous materials, but do not yet compete with the field annealed Finemet materials. At frequencies in excess of 300 kHz Mn ferrites losses look to be superior. Because of the lower Curie temperatures of Mn-Zn ferrite and the amorphous coupling phase in Finemet, both of these alloys are expected to have properties degrade at elevated temperatures more quickly than HITPERM. Potentials for improvement of HITPERM by alloy substitution and/or in-field crystallization has been documented by Frank Johnson. The high frequency response of HITPERM in the regime dominated by eddy current losses can be potentially improved with the development of planar flow casting techniques that allow for the production of thinner ribbons.

Frank Johnson successfully defended his Ph.D thesis entitled "High temperature and Frequency-dependent Properties and Structural evolution of HITPERM, an FeCo-base Nanocomposite Soft Ferromagnetic Material". Soft copies of this thesis were provided to Magnetics, Inc. and WPAFB at the 2nd Year 2nd Quarter review. Frank Johnson accepted a post-doctoral position with NIST Gaithersburg working for the group of Dr. R. Shull working under the direction of Dr. R. McMichael which he completed in 2005 and moved on to a pemanent position with GE The paper: Induced Anisotropy by Very High Magnetic Field Annealing of FeCo-based Nanocrystalline Soft Ferromagnetic Alloys. F. Johnson, H. Garmestami, S. Chu, M. E. McHenry, and D. E. Laughlin, appeared in 2004 in IEEE Trans. Mag. Frank's work on process development has been transitioned to Vladimir Keilin, working on PFC under the Magnetics ARL program. Alloy development is continuing with the work of Jianguo Long and Paul Ohodnicki on M.E. McHenry and D. E. Laughlin's currently funded NSF program.

III.1.7 Transition to Magnetics.

Materials development at CMU was coincident with materials processing developments. Frank Johnson and Chang Yong Um in installed a new Cu quenching wheel on melt spinner. with a lower total indicated runout and better dynamic balance. They attempted planar flow casting trials with slotted crucibles but our design never resulted in wide ribbons with excellent surface quality due to issues in controlling the gap between the crucible and wheel. The development effort in planar flow casting (PFC) was largely transferred to Magnetics, Inc. and their better equipped pilot scale caster which was developed concurrently. In subsequent studies by Vladimir Keilin HITPERM materials have been cast at Magnetics, Inc. using planar flow casting and losses better than commercial Metglas alloys have been demonstrated.

Magnetics, Inc. is currently funded by the Army Research Laboratory (ARL) and CMU is subcontracted to provide further alloy development. Vladimir Keilin is the key person charged with the alloy development program. He collaborates with Jianguo Long and Chang-yong Um on the transition of HITPERM and Fe-based amorphous alloys for pilot-caster scale-up.

Vladimir Keilin has benchmarked losses in new HITPERM compositions produced on the Magnetics, Inc. pilot melt caster.

References

1. M.E. McHenry, M.A. Willard and D.E. Laughlin, "Amorphous and Nanocrystalline Materials for Applications as Soft Magnets," *Progress in Materials Science* **44**, 1999, 291-433.

2. G. Herzer, "Grain-Size Dependence of Coercivity and Permeability in Nanocrystalline Ferromagnets," *Ieee Transactions on Magnetics*, **26**, 1990, pp. 1397-1402.

3. F. Johnson, High-temperature and Frequency-dependent Properties and Structural Evolution of HITPERM, an FeCo-base Nanocomposite Ssoft Ferromagnetic Material. Carnegie Mellon University Materials Science and Engineering Ph.d thesis 2003.

4. M. Willard, High-temperature and Frequency-dependent Properties and Structural Evolution of HITPERM, an FeCo-base Nanocomposite Ssoft Ferromagnetic Material. Carnegie Mellon University Materials Science and Engineering Ph.d thesis.

5. K. Suzuki, "Nanocrystalline Soft Magnetic Materials: a Decade of Alloy Development," *Materials Science Forum*, Vol. 312-314, 1999, pp. 521-30.

6. M.A. Willard, D.E. Laughlin, M.E. McHenry, D. Thoma, K. Sickafus, J.O. Cross and V.G. Harris, "Structure and Magnetic Properties of $(Fe_{0.5}Co_{0.5})_{88}Zr_7B_4Cu$ Nanocrystalline Alloys," *Journal of Applied Physics*, Vol. 84, 1998, pp. 6773-6777.

7. M.A. Willard, Y. Nakamura, D.E. Laughlin and M.E. McHenry, "Magnetic properties of ordered and disordered spinel-phase ferrimagnets," *Journal of the American Ceramic Society*, Vol. 82, 1999, pp. 3342-3346.

8. T. Kemeny, D. Kaptas, L.F. Kiss, J. Balogh, L. Bujdoso, J. Gubicza, T. Ungar and I. Vincze, "Structure and magnetic properties of nanocrystalline (Fe1-xCox)(90)Zr7B2Cu1 (0 <= x <= 0.6)," *Applied Physics Letters*, Vol. 76, 2000, pp. 2110-2112.

9. J.S. Blazquez, C.F. Conde and A. Conde, "Crystallisation process in (FeCo)(78)Nb-6(BCu)(16) alloys," *Journal of Non-Crystalline Solids*, Vol. 287, 2001, pp. 187-192.

10. J. Olszewski, H. Fukunaga, W. Ciurzynska, J. Zbroszczyk, A. Lukiewska, A. Mlynczyk, K. Perduta and J. Lelatko, "Microstructure and temperature dependence of magnetic properties of nanocrystalline Fe 42.7 Co 42.7 Zr 6.8-x Nb x B 6.8 Cu1 (x=0, 1) alloys," *Journal of Magnetism and Magnetic Materials*, Vol. 254-255, 2003, pp. 516-518.

11. J. Zbroszczyk, J. Olszewski, W. Ciurzynska, B. Wyslocki, R. Kolano, A. Mlynczyk, M. Lukiewski, A. Kolano and J. Lelatko, "Microstructure and some magnetic characteristics of amorphous and nanocrystalline $Fe_{83-x}Co_xNb_3 B_{13}Cu$ (x=0 or 41.5) Alloys," *Journal of Magnetism and Magnetic Materials* **254**, 2003, 513-515.

12. T. Kulik, A. Wlazlowska, J. Ferenc and J. Latuch, "Magnetically Soft Nanomaterials for High-temperature Applications," *IEEE Transactions on Magnetics*, **38**, 2002, 3075-3077.

13. H. Iwanabe, Bin Lu, M.E. McHenry and D.E. Laughlin, "Thermal Stability of the Nanocrystalline Fe-Co-Hf-B-Cu Alloy," *Journal of Applied Physics* **85**, 1999, 4424-6.

14. M.A. Willard, D.E. Laughlin and M.E. McHenry, "Recent advances in the development of $(Fe,Co)_{88}M_7B_4Cu$ magnets.," *Journal of Applied Physics*, **87**, 2000, 7091-7096.

15. J.D. Ayers, J.H. Konnert, P. Dantonio, A. Pattnaik, C.L. Vold and H.N. Jones, "Morphology of Surface Crystallites on Amorphous Fe87zr7b5cu1," *Journal of Materials Science* **30**, 1995, pp. 4492-4506.

16. D.H. Ping, Y.Q. Wu, K. Hono, M.A. Willard, M.E. McHenry and D.E. Laughlin, "Microstructural characterization of $(Fe_{0.5}Co_{0.5})_{88}Zr_7B_4Cu$ Nanocrystalline Alloys," *Scripta Materialia* **45**, 2001, pp. 781-786.

17. W.R. Wieserman, G.E. Schwarze and J.M. Niedra, *Comparison of high temperature, high frequency core loss and dynamic B-H loops of a 2V-49Fe-49Co and a grain oriented 3Si-Fe alloy*, San Diego, CA, USA: Soc. Automotive Eng, 1992.

III.2 Fe-based Amorphous Materials

Fe-based amorphous materials have been studied in the thesis research of Chang-yong Um. Changyong is currently working on writing up his thesis and transitioning promising alloy compositions to Magnetics, Inc. He is supported until May 2005 by ICES PITA funding. Chang-yong's thesis overview draft has been provided to Magnetics and Air Force personnel. It is anticipated that he will defend his thesis will be defended in Spring 2006.

The statement of work items and their timeline for the DUST task on developing Fe-based amorphous materials is shown in Table III.1. Major results for this task are detailed in this section.

Statement of Work Item	Year1	Year 2	Year 3
Fe-based Amorphous Materials			
Materials Synthesis – Chemistry Determination (Iteration)	X	(X)	
Structural Characterization (Iteration)	X	(X)	
Magnetic Characterization (Iteration)	X	(X)	
Properties measurements of magnetic cores (Iteration)	X	(X)	
Transition to Magnetics, Inc. for Scale-up (Iteration)	X	(X)	

Table III.2: Statement of work for DUST task: Fe-based Amorphous Materials

III.2.1 Materials Synthesis – Chemistry Determination

Materials synthesis efforts in this task required several process improvements and modifications. A new melt spinner casting wheel was installed to alleviate problems in maintaining stable puddle between the nozzle and wheel due vibration. Planar flow casting (PFC) trials were performed with Quartz crucibles supplied by Glas Werk and Finkenbeiner. The minimum crucible-wheel gap distance achievable in our PFC design was found to be approximately 0.5 mm for the crucible from Finkenbeiner and 0.75 mm for the crucible from Glaswerk. By reference to Ranjan Ray's PFC procedure the wheel-gap distance must be below 1mm in PFC, three different gap distances of 0.5, 0.75, and 1 mm, measured by insertion of the filler gauge into the gap between the highest spot of the wheel taking into account the run-out and the crucible, were employed in our PFC trials. Melt-spin runs at various gap distance, wheel speeds and applied argon gas flow rates were performed using the two different types of crucibles to establish a correlation between the processing parameters and the ribbon thickness. Most runs couldn't successfully produce the amorphous ribbons however, the thickness was found to decrease with decreasing gap distance and increasing wheel speed. A problem with the nozzle plug was apparent in most of runs (severe with the crucible from Glaswerk). Using the crucible from Finkenbeiner we had two successful runs in the thin ribbon production.

Materials synthesis was initiated on alloys of the typical Metglas composition, $Fe_{78}B_{13}Si_9$. Alloy compositions chosen were based on the Luborsky, et al., U. S Patents 4,217,135 and 4,300,950. Attempts at producing bulk amorphous alloys included studied of compositions related to Metglas. These were of interest because of the possibility of producing large cross-sections by conventional slow cooling processes due to their large glass forming ability. Our research focused on the amorphous alloy production of multi-component systems with high induction by copper mould casting. We were unsuccessful in producing amorphous, melt-spun samples from the $(Fe_{75}B_{15}S_{I0})_{100-x}Nb_x$ bulk amorphous alloy composition developed by A. Inoue. We modified the above composition slightly and successfully produced amorphous ribbons with the composition of $(Fe_{78}B_{13}Si_9)_{99}Nb_1$, $(Fe_{78}B_{13}Si_9)_{98}Nb_2$, $(Fe_{78}B_{13}Si_9)_{98}Nb_2$, $(Fe_{39}Co_{39}B_{13}Si_9)_{99}Nb_4$.

Fe-based new soft magnetic bulk amorphous alloy development focused on finding alloy compositions having large GFA and good intrinsic magnetic properties. We investigated tuning the crystallization temperatures for the potential bulk amorphous alloy production and tuning the Curie temperature and saturation magnetization for the high operating temperature applications through alloying additions. Additional alloys were designed based on the modification to the previously described Nb containing Metglas alloy compositions to achieve two goals:

(1) Substitutions of several combinations of early transition metals (Mo, Ta, Hf, Zr) and metalloids (P, Al) have been made to produce multi-component alloy systems with large Glass Forming Ability (GFA).

(2) Co substitutions were made to increase the T_c and M_s.

New alloys that included elements sensitive to oxidation (Zr, Hf, Al) were found to hard to cast in the form of amorphous ribbons. The ferro-phosphorous we employed for phosphorous additions also was observed to decrease castability, possibly due to raw materials chemistry. Amorphous alloys were successfully cast with the compositions: $(Fe_{81.7}B_{13.5}Si_5)_{96}Nb_4$, $Fe_{81.7}B_{13.3}Nb_5$, $Fe_{82}Nb_3Mo_1Ta_1B_{13}$ and $Fe_{41}Co_{41}Nb_3Mo_1Ta_1B_{13}$. In particular, the last of these was shown to have both excellent GFA and intrinsic high temperature magnetic properties.

$Fe_{82-x}Co_xNb_3Ta_1Mo_1B_{13}$ ($0 \leq x \leq 41$) amorphous alloys were produced by rapid solidification to investigate the optimization of magnetic properties and core losses with Fe:Co ratio. The lowest losses were observed in $Fe_{82-x}Co_xNb_3Ta_1Mo_1B_{13}$ (x = 20.5) alloy as discussed below. It was therefore targeted for further compositional tuning and comparative loss measurements.. In an attempt to reduce the core loss, a series of Ni substitutions (x = 0, 4, 8, 12, 16, and 20.5) for Co in our alloy $Fe_{82-x}Co_xNb_3Ta_1Mo_1B_{13}$ (x = 20.5) were made.
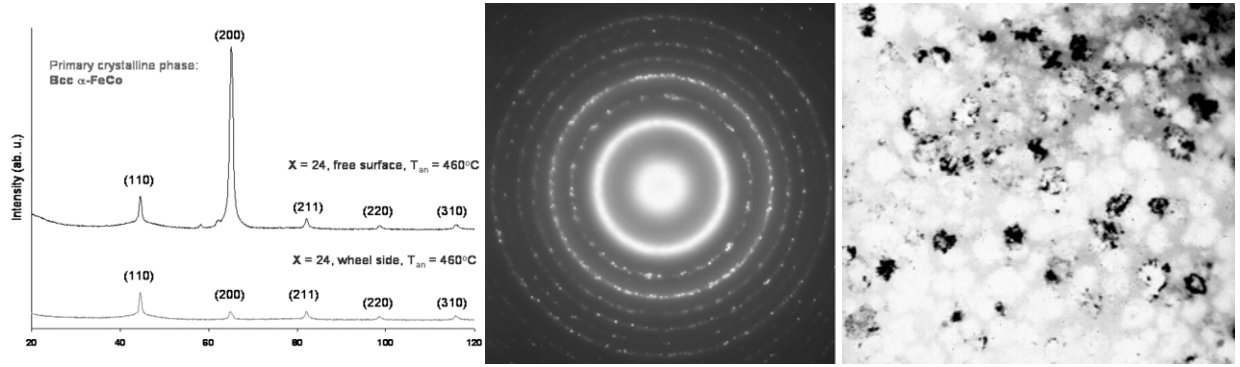
III.2.2 Structural Characterization

Structural characterization of as-cast and nanocrystallized alloys were routinely performed by XRD. Selected samples were studied by TEM and HRTEM. Chang-yong Um was trained in TEM operation and sample preparation from Hideuki Okumura and Tom Nuhfer. His initial studies were of crystallization products of Metglas alloys to identify the primary and secondary crystallization products of the Fe-based amorphous materials, to complement the study of crystallization temperatures and kinetic studies.

Chang-yong Um performed crystallization experiments of Fe-based amorphous materials. After an Fe-based amorphous ribbon with a $Fe_{81.7}B_{13.3}Si_5$ composition was heated from room temperature to 590 ^oC at 30^oC/min, in a DSC (Differential Scanning Calorimeter), a BCC Fe (a = 2.87Å) and tetragonal Fe_2B phase (a = 5.10Å, c = 4.24Å) was observed. These phases have been identified by Hide Okumura using TEM electron diffraction. In the TEM the large grains (of submicron size) of the BCC Fe phase, and smaller grains, less than 100 nm of aboride phase were identified. The crystallization products were observed to be slightly different in a Metglas composition with a lower B concentration ($Fe_{82.2}B_{11.7}Si_{6.1}$). Another minority phase with a tetragonal Fe_3B structure (a = 8.67 Å, c = 4.31 Å) was determined by electron diffraction.

$Fe_{82-x}Co_xNb_3Ta_1Mo_1B_{13}$ ($0 \leq x \leq 41$) amorphous alloys were produced by rapid solidification and have been reported on in the paper: Magnetic Properties of Co-substituted Fe-Nb-B-Ta-Mo Bulk Amorphous Alloys. C. Um and M. E. McHenry, IEEE Trans. Mag.[1] These amorphous alloys were characterized by XRD and TEM. The XRD scan [Fig. III.2.1(a)] and electron diffraction pattern [Fig. III.2.1(b)] revealed primary crystallization to yield a bcc α-FeCo phase. The alloy $Fe_{82-x}Co_xNb_3Ta_1Mo_1B_{13}$ (x = 20.5) was identified as having the best soft magnetic properties and was the subject of further studies including loss measurements.
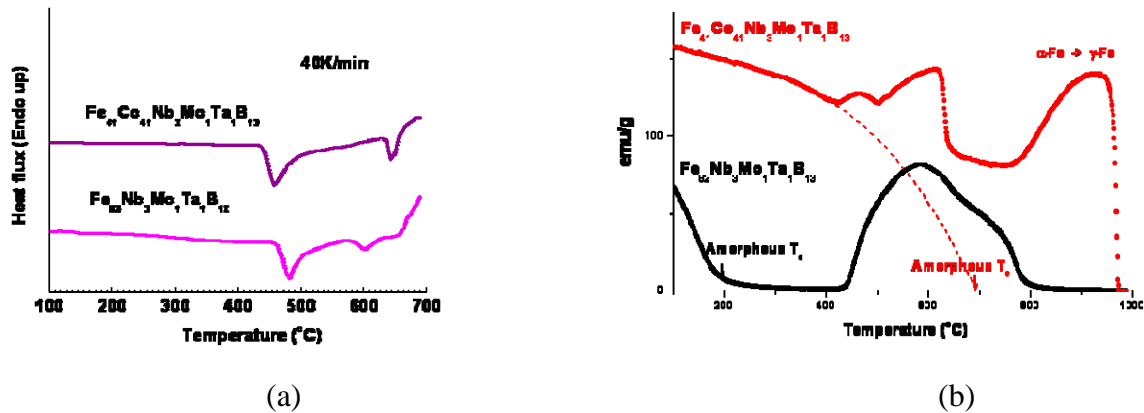
Fig. III.2.1: (a) XRD data (free surface and wheel side) for an $Fe_{82-x}Co_xNb_3Ta_1Mo_1B_{13}$ (x=24) alloy heated to T_{an} at 4°C/min and water-cooled, showing α-FeCo primary crystallization products. (b) EDPT for α-FeCo showing a bcc ring patterns and an amorphous halo. (c) BF image shows α-FeCo particles dispersed in the amorphous matrix.

Microstructural features in fully crystallized $Fe_{61.5}Co_{20.5}Nb_3B_{13}Ta_1Mo_1$ alloy included large crystals of approximately 20 μm in size having a $Fe_{75}Co_{25}$ composition. A lamellar intergranular eutectic microstructure was observed by EDS to have the composition of $Fe_{62.7}Co_{25.4}Nb_{5.4}Mo_{2.5}Ta_4$. Boron was not detectable because of its light atomic mass.

III.2.3 Magnetic Characterization and Properties Measurements

DSC and VSM were used for measurement of T-dependent magnetic properties of alloys of composition $Fe_{82}Nb_3Mo_1Ta_1B_{13}$ and $Fe_{41}Co_{41}Nb_3Mo_1Ta_1B_{13}$ (Fig.III.2.2). The substitution of Co for half of the Fe increased the amorphous phase Curie temperature, T_c^{am}, by ~140 K to the point where the primary crystallization temperature, T_{x1}, exceeded T_c^{am}. This is thought to be important for optimal response in field crystallization. T_{x1} was also observed to decrease and a glass transition was not observed in the Co-containing alloy. Three crystallization reactions were observed in this multi-component system attributed to the composition being far from a eutectic. Co substitutions increased the moment and T_c^{am}. The Co containing alloy had large moment at high temperature making it attractive for high T applications.

| (a) | (b) |

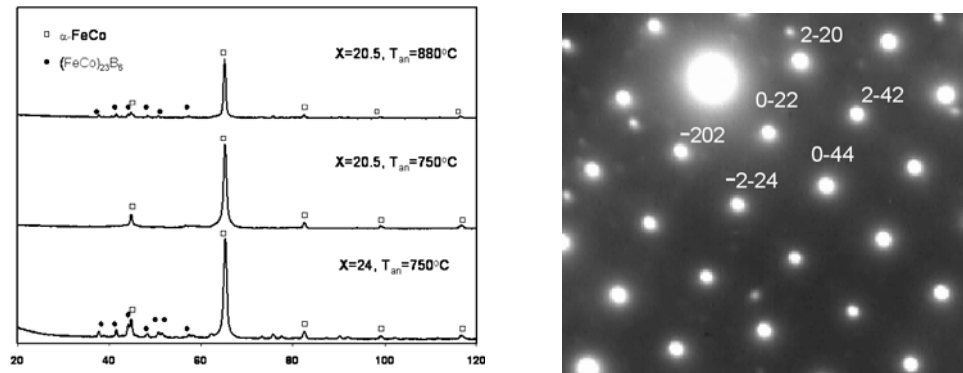**Figure III.2.2:** (a) DSC on Co and non-Co containing amorphous alloys, (b) M(T) for the same.

Fig.III.2.3 illustrates T-dependence of the magnetization for $Fe_{82-x}Co_xNb_3Ta_1Mo_1B_{13}$ alloys with the two compositions, x = 20.5 and x = 24. A gradual decrease in the saturation

magnetization in the initial heating stage reflects the Curie transition of the amorphous phase. An increase in the M_s begins well below the Curie transition of the amorphous phase, indicating the crystallization of a ferromagnetic primary crystalline phase embedded in the still ferromagnetic amorphous matrix. After the primary crystallization the magnetization decreases for a temperature interval of ~30 $^{\circ}$C potentially due to the Curie transition of another magnetic phase that may have precipitated at lower temperatures. It starts increasing again with the increase of the volume fraction of the bcc α-FeCo phase.

Figure III.2.3: Thermomagnetic data of x = 20.5 and x = 24 in a heating cycle and x = 24 in a cooling cycle of $Fe_{82-x}Co_xNb_3Ta_1Mo_1B_{13}$ alloys.

A 25 % decrease in the magnetization was observed for 620 $^{\circ}$C < T < 650 $^{\circ}$C for $18 \leq x \leq 41$ with the exception of the x = 20.5 composition. This temperature range corresponds to the secondary crystallization temperature, T_{x2} determined by DSC. The formation of an $(FeCo)_{23}B_6$ phase with a fcc structure was confirmed using XRD [Figure III.2.4(a)] and TEM electron diffraction [Figure III.2.4(b)] on samples heated to 750 $^{\circ}$C. This phase was not observed for the x = 20.5 composition. This suggests a large loss in magnetization resulted from secondary crystallization of the nonmagnetic $(FeCo)_{23}B_6$ phase, consuming some of the α-FeCo phase. This is consistent with observations originally reported by J. S. Blazquez et al. for HITPERM alloys[2]. The abrupt decrease in the magnetization was not observed until 790 $^{\circ}$C for the x = 20.5 composition, where the fractional decrease is smaller than that observed in the other alloys. For sample quenched from above this temperature, the $(FeCo)_{23}B_6$ phase was identified by XRD.

Figure III.2.4: (a) XRD patterns of x =20.5 and x = 24 of $Fe_{82-x}Co_xNb_3Ta_1Mo_1B_{13}$ alloys heated to T_{an} at 4°C/min and water-cooled, identifying the a-FeCo and $(FeCo)_{23}B_6$ crystallization products. (b) EDPT of $(FeCo)_{23}B_6$ phase shows an FCC[110] zone axis.

The previous data imply a strong compositional dependence for the formation of the $(FeCo)_{23}B_6$ phase. The thermomagnetic data for the x = 20.5 composition was reproduced three times and the alloy composition was validated by EDS chemical analysis. Keeping the high moment to higher temperatures (delaying the magnetization drop) ~ 140 ^{o}C widens the temperature interval over which only ferromagnetic phases exist. The small increase in the moment at ~590 ^{o}C corresponded to the T_{X2} determined by DSC. This increase can be attributed to a new magnetic phase forming in the amorphous matrix.

The T-dependence of the magnetization after secondary crystallization was postulated to reflect the sum of the moments from the α-FeCo and unknown magnetic phases that could include a secondary boride, niobide, or other ferromagnetic phases. The magnetization was seen to gradually decrease for a temperature interval of ~130 ^{o}C for the x = 24 composition due to the Curie transition of this unidentified ferromagnetic phase. At ~900 ^{o}C a rise in the magnetization is observed, followed by a gradual and then abrupt drop at ~960 ^{o}C for both compositions. It is postulated that the increased magnetization reflects an increasing volume fraction of the high moment α-FeCo phase. The abrupt drop in the magnetization (to zero) is consistent with the first order α→γ structural transformation of the FeCo phase. This also implies that any other remaining secondary ferromagnetic phases have lower Curie temperatures than α-FeCo phase. As the temperature is increased the α-FeCo phase may grow consuming other secondary phases. The reversibility of the α→γ structural transformation is revealed in the cooling cycle. The observed transition temperatures for $0 \le x \le 12$ and $18 \le x \le 41$ agree well with the composition dependence of Curie transition of α-FeCo phase and α→γ structural transformation reported in the equilibrium Fe-Co phase diagram, respectively.

Nanocrystallization kinetics of a Finemet ($Fe_{71.1}Si_{18.5}B_{6.3}Nb_3Cu_{1.1}$) and a Nanoperm alloy ($Fe_{91}Zr_7B_2$) were studied and the variation of mechanical properties (hardness) with volume fraction of the crystalline phase (VFC) compared. Time-dependent magnetization and hysteresis loop measurements were used to determine VFC for Finemet and Nanoperm, respectively. Both the isothermal and continuous heating experiments were used to determine the crystallization kinetics for Finemet, while hardness measurements were used for Nanoperm. Kinetic results provided the information necessary to interpret the hardness measurements. Hardness was measured by nanoindentation as a function of VFC to investigate the effect of the evolution of the nanocomposite structure on the mechanical properties. A linear increase in hardness was observed[3]. The detailed results are discussed in reference 4. *This technique could be extended to provide a more exhaustive general study of nanocomposite materials in the future.*

Magnetostriction measurements using a strain gage technique were performed on alloys with the compositions $Fe_{82-x}Co_xB_{12}Nb_3Mo_1Ta_1$. The trend of magentostriction constant with composition was observed to be similar to that of coercivity in the range of $16 \le x \le 36$. This suggested that magnetostriction is the determining factor for the coercivity.
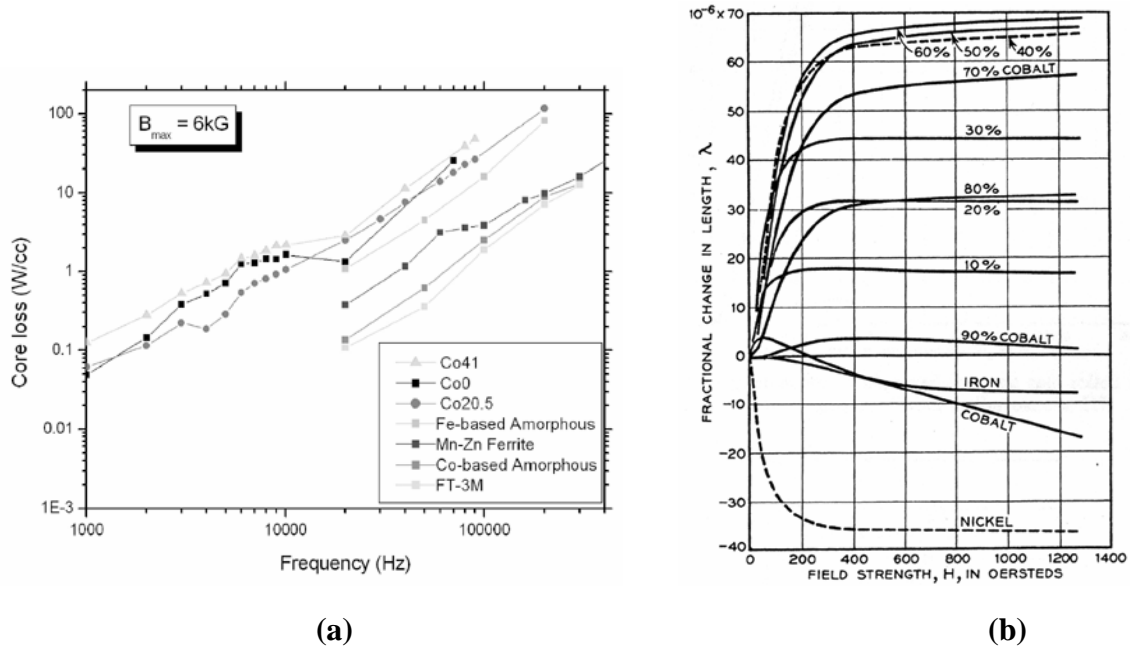
III.2.4 Magnetic Core Loss Measurments

Core-loss measurements required development of ceramic bobbins to facilitate annealing. Frank Johnson has assisted Chang-Yong Um on producing ceramic bobbin tape wound cores for core loss measurements. Core-loss measurements were performed on a Walker AMH-401 permeameter. Julia Hess, a CMU MSE undergraduate aided in core winding and crystallization experiments (partially supported from the Small Undergraduate Research Grant (SURG) program at CMU. Tape wound cores were provided to Magnetics, Inc. for core loss measurements. Initial measurements were performed on alloys of composition: $Fe_{82.2}B_{11.7}Si_{6.1,}$

$Fe_{82.3}B_{11.2}Si_{6.5}$, $Fe_{82.6}B_{10.5}Si_{6.9}$, and $Fe_{82.7}B_{9.7}Si_{7.6}$ covered by the US. Patent of E. Luborsky et al. It was determined that stress relief annealing lowered losses for all compositions.

Hysteresis loops for $Fe_{82}Nb_3Mo_1Ta_1B_{13}$ and $Fe_{41}Co_{41}Nb_3Mo_1Ta_1B_{13}$ amorphous alloys showed both alloys to be very soft and exhibit the small coercivity required for the potential soft magnetic applications. The coercivity in the $Fe_{82-x}Co_xNb_3Ta_1Mo_1B_{13}$ ($0 \leq x \leq 41$) bulk amorphous alloys was shown to decrease with increasing Co content. Relatively small coercivities (0.3 Oe $\leq$ H_c $\leq$ 0.5 Oe) were observed at 25 at% and 50 at% Co. However, the AC coercivity was observed to increase at the 50 at% Co (x = 41) composition resulting in the larger core loss. The frequency response of the core loss of the first alloys produced were comparable to HITPERM. $Fe_{82-x}Co_xNb_3Ta_1Mo_1B_{13}$ ($0 \leq x \leq 41$) amorphous alloys were have been reported on by C. Um and M. E. McHenry IEEE Trans. Mag.[1]
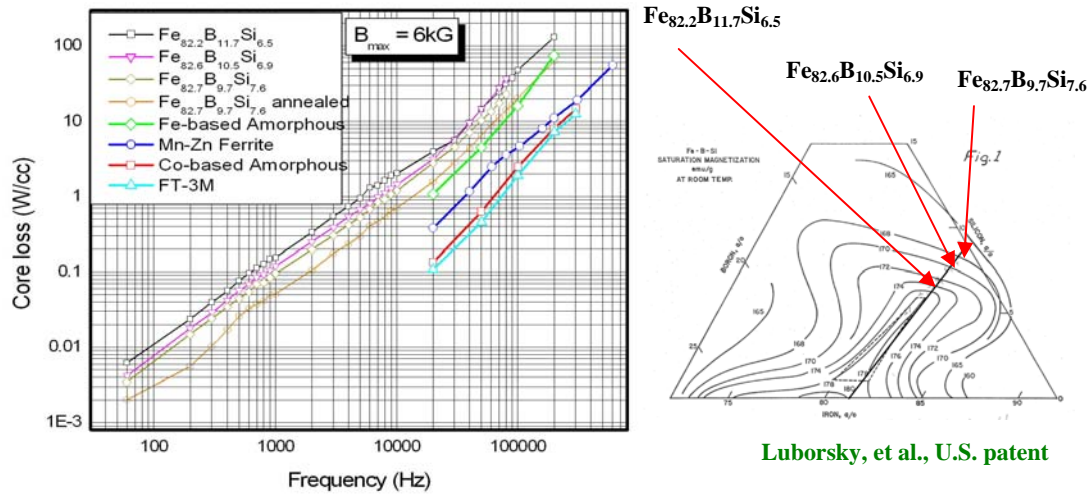
The frequency dependence of core loss (W/cc) at B_{max} = 0.6 T was benchmarked for various commercial soft magnetic materials (field annealed) compared with our multi-component as-cast amorphous alloys containing 0, 20.5, and 41 at% Co, respectively as illustrated in Figure III.2.5. Data for the commercial materials were taken from the Hitachi Metals website and scaled to 0.6 T assuming the core loss to scale as ~ B^2 to be compared with our alloys. The composition dependence of core loss of our alloys was in part attributed to the compositional dependence of the magnetostriction constant, λ. The significant increase of λ after substitution of 50% Co as shown in Figure III.2.5(b) is consistent with the higher core loss for our alloy with 41 at% Co (Fe:Co = 1:1) than that without Co. The decrease of core loss for the alloy with 20.5 at% Co (Fe:Co = 3:1) is consistent with data for 30% Co bulk Fe-Co alloys in Figure III.2.5(b). Since the lowest losses were observed in $Fe_{82-x}Co_xNb_3Ta_1Mo_1B_{13}$ (x=20.5) alloy, it was targeted for compositional tuning and comparative loss measurements.

(a)   **(b)**

Figure III.2.5: (a) Frequency dependence of core loss at B_{max} = 0.6 T for selected soft magnetic materials Co41, Co0 and Co20.5 refer to our $Fe_{82-x}Co_xNb_3Ta_1Mo_1B_{13}$ alloys containing 0, 20.5, and 41at% Co, respectively, FT-3M is a state of the art Finemet material; (b) magnetostriction of iron-cobalt alloys and Ni plotted as a function of field strength.

The lowest core loss we observed for $Fe_{82-x}Co_xNb_3Ta_1Mo_1B_{13}$ (x = 20.5) was consistent with magnetostriction and coercivity measurements. In addition, the x = 0 and 24 compositions had relatively small magnetostriction and showed comparable core loss at B_{max} = 0.6 T. The difference in the core loss at different compositions diminished with increasing B_{max} due having an induction exponent smaller than 2 (1.5-1.6) to which the hysteretic core loss, P_h ($P_h = P_{tot} - P_{exess\ eddy\ current\ loss} - P_{classical\ eddy\ current\ loss}$) is related. The other parts of core loss, P_{ex} and P_{cl} have a square power relationship with B_{max}. The core loss for x = 20.5 at B_{max} = 0.6 T approaches that of Fe-based amorphous alloys and crossed over for f > 200 kHz. An optimum annealing treatment on this variant was predicted to further reduce core loss. Only FT-3M nanocrystalline alloys are competitive with this alloy at the high maximum flux induction range.

A possible further improvement on our alloy, from a cost perspective would be in substituting Si for B. Figure III.2.6 shows the core loss for conventional Fe-B-Si hypoeutectic Metglas alloy compositions which were selected along the tie line on the ternary diagram. Along this line, the expensive B can be replaced with the cheaper Si, leading to the reduction of production cost. The substitution of B with Si also reduced the core loss and it became closer to that for Fe-based amorphous alloys after stress relief annealing process. *These alloy additions will need to be studied in future work.*

Figure III.2.6: Frequency dependent core loss for conventional Fe-B-Si hypoeutectic Metglas alloy compositions which were selected along the tie line on the ternary diagram.

In a final attempt to reduce the core loss further, a series of Ni substitutions (x = 0, 4, 8, 12, 16, and 20.5) for Co in our alloy composition: $Fe_{60.5}Co_{20.5-x}Ni_xB_{13}Nb_3Ta_1Mo_1$, were made. This was based on our postulate that since Ni metal shows comparable magnitude and opposite sign of magnetostriction coefficient, λ to the FeCo alloy with 30 at% Co, Ni substitutions for Co in our alloy composition containing 20.5 at% Co (Fe:Co = 3:1) might reduce λ. A benchmark of the frequency dependence of core loss (W/cc) at B_{max} = 0.6 T for various commercial soft magnetic materials (field annealed) compared with our multicomponent as-cast amorphous alloys containing 0, 4, 12, 16, and 20.5 at% Ni, respectively was made. A significant core loss reduction after Ni addition was attributed to the decrease of λ as we expected, however, the dependence of the core loss on the amount of Ni addition was anomalous. The accuracy of the

25

magnitude of the core loss was affected by the method of determining the cross-sectional area. *These alloy additions will also need to be studied in future work.*

Loss Separation Analysis[2,3]

We have used recently proposed models[2,3] to separate loss components from our data. The total loss (P_{tot}) is decomposed into the sum of hysteresis (P_h), classical (P_{cl}), and excess loss (P_{ex}) components. Loss separation is a useful way to analyze each loss as if they were independent each other. Static hysteresis loss per cycle were fit to the Steinmetz model by the power law relation: $P_h = P_0 B^n_{max}$ where P_0 is a fitting parameter, and the exponent, n normally ranges from 1.5 to 1.7. Classical losses are large-scale losses, emerging on the scale of the sample geometry, where magnetic domains are no longer resolved and the material appears as a homogeneous medium. They are directly calculated form Maxwell's equations. In the low-f limit, H inside the laminate shows only a slight deviation from the applied field, meaning that $H_{eddy} \ll H_a$. If we introduce a dimensionless parameter, γ, which can be derived from a dispersion relation then:

$$\gamma = \sqrt{\pi \sigma \mu d^2 f}$$

[3.3]

where d = thickness of a laminate, μ = permeability, and σ = conductivity. This low-frequency limit is the case for $\gamma \ll 1$, and under sinusoidal induction one has:

$$\frac{P_{cl}}{f} = \frac{\pi^2 d^2 B_{max}^2 f}{6\rho}$$

[3.4]

where ρ is resistivity. At the other extreme, $\gamma \gg 1$, one finds:

$$\frac{P_{cl}}{f} \cong \frac{\pi^{3/2} t B_{max} \sqrt{f}}{2\sqrt{\mu\rho}}$$

[3.5]

Excess losses are the direct consequence of the existence of an intermediate scale, the scale of magnetic domains. This loss term can be separated from the total loss by the subtraction of the hysteresis and classical loss. A statistical loss theory was applied by Bertotti, et al[5] to analyze this excess loss. The excess field resulting from domain wall effect is called H_{ex} and can be determined from the following relation:
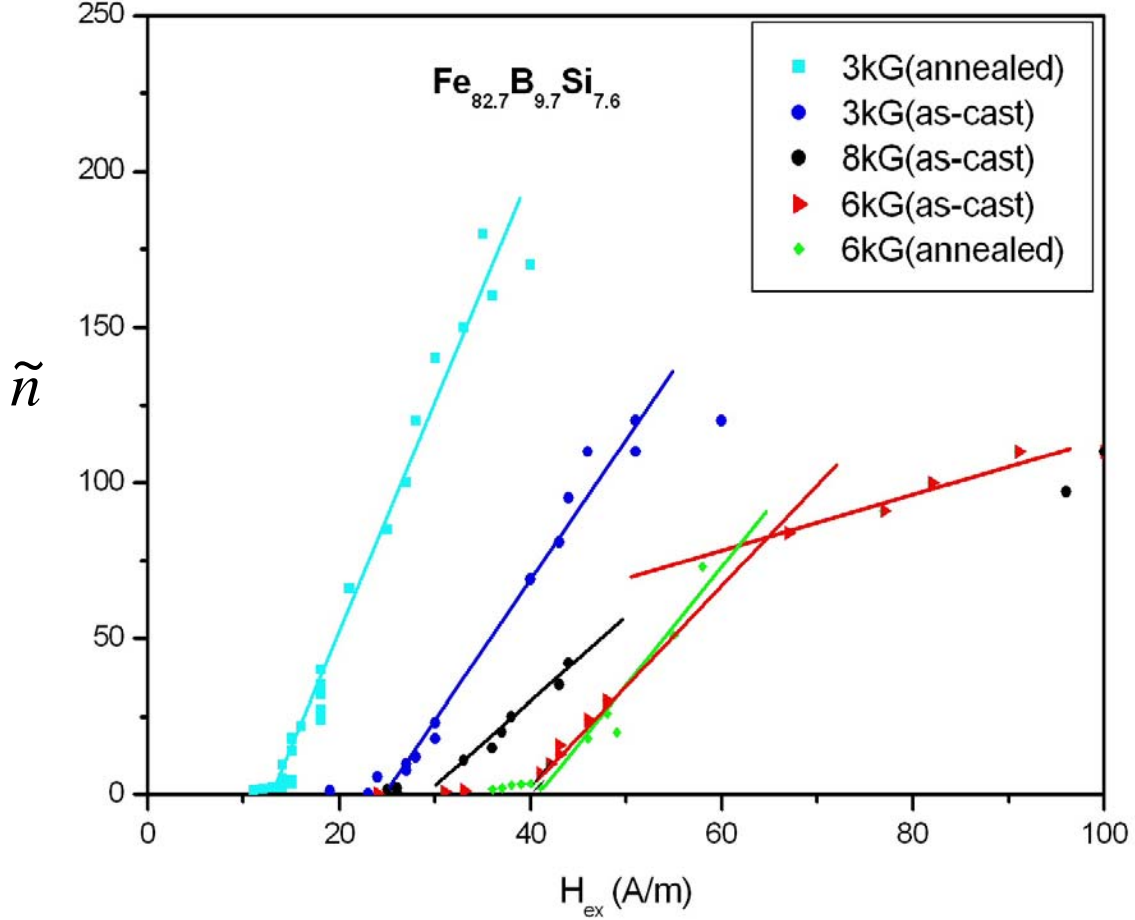
$$H_{ex} = \frac{P_{ex}}{4 B_{max} f}$$

[3.6]

This excess field is related to n, number of active flux switching regions by the formula:

$$H_{ex} = \frac{H^{(w)}}{\tilde{n}} = \frac{4 G S B_{max} f}{\rho \tilde{n}}$$

[3.7]

where H(w) is the switching field for the single domain wall and G = 0.1356 is a geometric factor describing the same. n has been plotted as a function of H_{ex} for amorphous alloy with composition $Fe_{82.7}B_{9.7}Si_{7.6}$ (Figure III.2.7). We just ignored the hysteresis loss, therefore the excess loss determined from this analysis can be slightly larger. A resistivity of 1.5 $\mu\Omega.m$ was used to determine the classical and excess losses. As seen in from Figure III.2.7, the n shows a

linearly increasing function of H_{ex}. The slope can be defined as $1/V_0$, where V_0 is a threshold field for the domain wall movement. The decrease of V_0 with stress relief annealing process for $B_{max} = 0.3$ and 0.6 T of can be read from this plot, meaning that the number of domain walls active at the same excess field is greater after annealing process, leading to the smaller excess losses. In the same sense, the increase of V_0 with increasing B_{max} represents the larger loss with increasing B_{max}. Another slope for the as-cast core at the 0.6 T B_{max} is probably due to the use of low-frequency limit equation for the classical loss calculation in the high f range.

Figure III.2.7: Number of active switching regions as a function of the excess field, as determined by a statistical model for excess eddy current loss. The slope is related to microstructural features of the sample and is equal to $1/V_0$

III.2.5 Transition to Magnetics, Inc. for Scale-up

Our Fe-based amorphous alloy with the lowest losses has been transitioned to Spang for pilot plant scale-up on their melt caster. They have successfully cast wide ribbons of composition $Fe_{61.5}Co_{20.5}Nb_3Ta_1Mo_1B_{13}$. These have been field annealed in a home built field annealing furnace prior to the commissioning of their newly purchased transverse field annealing furnace. Ring cores with dimensions 23.5 x 17.8 x 12.7 mm were produced from amorphous ribbon with a width of 12.7 mm and thickness of 0.025 mm. These were annealed at 410 ^{0}C for 1 hr in air and cooled in transverse magnetic field of 240 kA/m. The results of magnetic properties

measurements including loss measurements are summarized, by Vladimir Keilin, in Table III.2.1. These are benchmarked with FINEMET (FT-3) and a commercial Fe-based metallic glass (MT2001). Notable are the comparable losses between the $Fe_{61.5}Co_{20.5}Nb_3Ta_1Mo_1B_{13}$ material and FINEMET at 200 kHz. The thermal stability of this alloy has also been demonstrated to ~300 ^{0}C by Vladimir Keilin. The ultimate thermal stability appears to originate in the stability of the field induced anisotropy.

ALLOY	B800, T	Squareness Kr	μ initial permeability	Core loss at 0.2T&20kHz W/kg	Core loss at 0.02T&200kHz W/kg
$Fe_{61.5}Co_{20.5}Nb_3Ta_1Mo_1B_{13}$	1.4	0.08	1650	11	1.6
FINEMET	1.2	0.05	80,000	3.2	1.6
MT2001	1.45	0.20	1800	10	4.9

Table III.2.1: Benchmarking of magnetic properties of CMU's $Fe_{61.5}Co_{20.5}Nb_3Ta_1Mo_1B_{13}$ alloy on the Magnetic's melt-spin caster as compared with FINEMET (FT-3) and a commercial Fe-based metallic glass (MT2001).

As seen in Table III.2.1, properties measurements of the CMU alloy at Spang include initial permeabilities in excess of 1200 for temperatures up to 410 ^{0}C, inductions as high as 1.5 T (measured in a 800 A/m (10 Oe) applied field) at 450 ^{0}C. A core loss of 30 W/kg at 400 ^{0}C at a 0.2 T induction at 20 kHz was measured. Core loss at 0.02 T and 200 kHz was measured to be ~3 W/kg and relatively invariant with temperature. These losses are comparable to Finemet at 200 kHz and lower at frequencies above 200 kHz and better than results previously reported by CMU due to thinner ribbons and the impact of field annealing.

References
1. C.-Y. Um and M. E. McHenry, Magnetic Properties of Co-substituted Fe-Nb-B-Ta-Mo Bulk Amorphous Alloys. IEEE Trans. Mag. 40 (4): 2697-2699, (2004).
2. J. S. Blazquez, C. F. Conde, and A. Conde, "Thermomagnetic detection of recrystallization in FeCoNbBCu nanocrystalline alloys," *Appl. Phys. Lett.,* vol. 79, pp. 2898-2900, 2001.
3. C.-Y. Um, F. Johnson, M. Simone, J. Barrow, and M. E. McHenry, Effect of Crystal Fraction on Hardness in FINEMET and NANOPERM Nanocomposite Alloys. J. Appl. Phys. (2005).
4. A. W. Molvik, A. Faltens, Phys. Rev. Special Topics-Accelerators and Beams, **5**, 080401 (2002).
5. G. Berttoti, Hysteresis in Magnetism (Academic Press, New York, 1998)
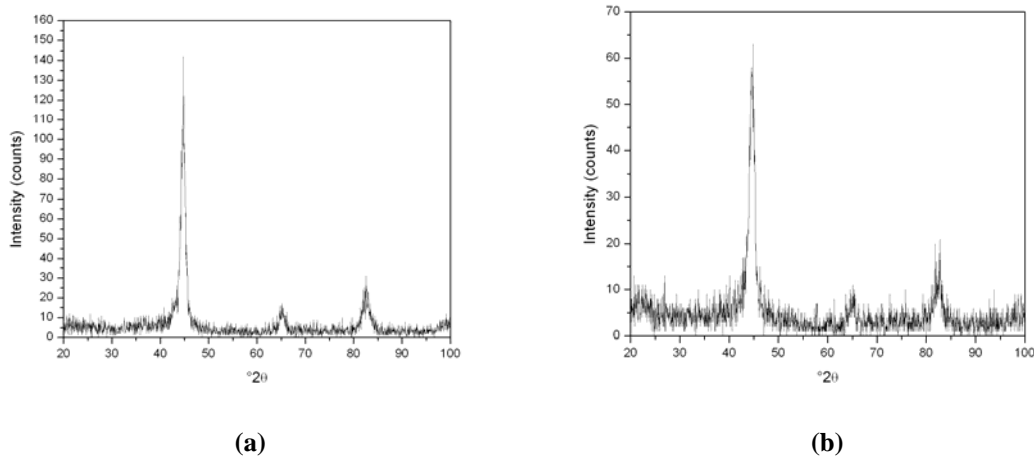6. M. Willard et al., MMM proceeding, in press (2005)

III.3   HITPERM Powders

The statement of work items and their timeline for the DUST task on developing HITPERM powder materials is shown in Table III.3.   Major results for this task are detailed in this section.

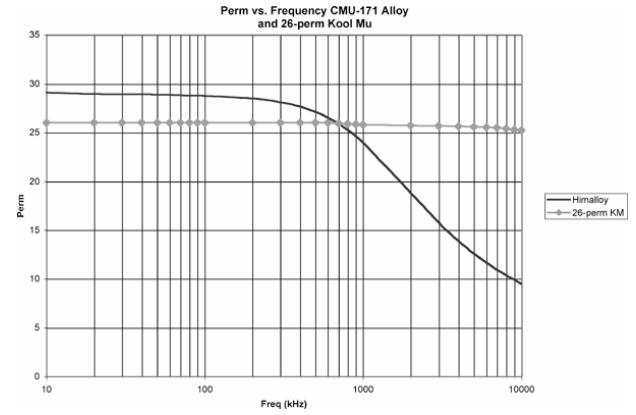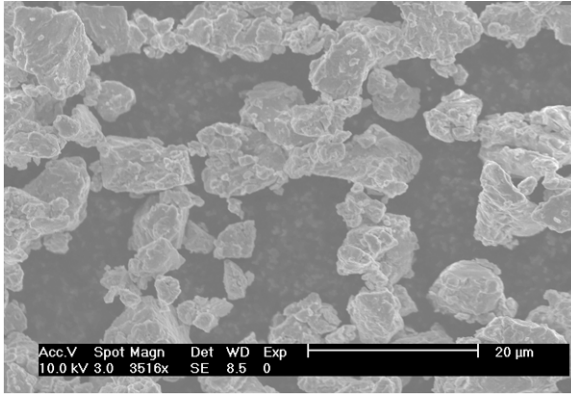| HITPERM Powders			
Materials Synthesis – Chemistry Determination, Optimization	X	X	
Structural Characterization	X	X	
Magnetic Characterization	X	X	X
Powders to Magnetics, Inc. for Cores		X	X
Properties measurements of powder cores		X	X
Communicate Results to Boeing (supply Cores if viable and competitive)		X	X
Report Results			X

Table III.3: Statement of work, DUST task: Amorphous Precursors to HITPERM Materials.

Frank Johnson and Hide Okumura provided ~200 g grams each of base HITPERM ($Fe_{44.5}Co_{44.5}Zr_7B_4$) and HIMALLOY compositions to Magnetics, Inc. for processing into crystalline powder cores. M Magnetics, Inc. crystallized and crushed the ribbon. XRD patterns of the crushed powders are shown in Figures III.3.1(a) and (b), for HITPERM and HIMALLOY, respectively. The XRD indicated that the powders were nanocrystalline. Magnetics, Inc. produced pressed powder cores from these materials. The magnetic characterization of powder cores was performed at Magnetics, Inc.

| (a) | (b) |

Figure III.3.1: X-Ray diffraction pattern of crushed HITPERM (a) and HIMALLOY powder (b)

Materials were nanocrystallized at 600 ^{0}C for 1 hr in N_2 prior to milling for 14 hr. A size distribution of: +120 0.9%; +200 2.8%; +230 1.5%; +325 38.9%; +400 0.7%; -400 55.3%; was determined by Magnetics, Inc. SEM observations confirmed the material chemistry and showed the morphology of the particles to be small platelets. III.3.2(a) shows typical crushed HITPERM particles. Efforts to compact this material into cores have been made and AC properties measured on these cores as illustrated in III.3.2 (b). Permeability was ~10% larger than Kool-mu powder cores for f ~10-100 kHz and equal to Kool-mu at ~700 kHz.

III.3.2: (a) Morphology of milled HITPERM materials and (b) permeability as a function of frequency for powdered HITPERM cores as compared with Kool-mu powder cores.

A new SPEX mill has recently been purchased with ARL funding for use in continuing production of HITPERM powders and precursors for ferrite nanoparticles synthesis.
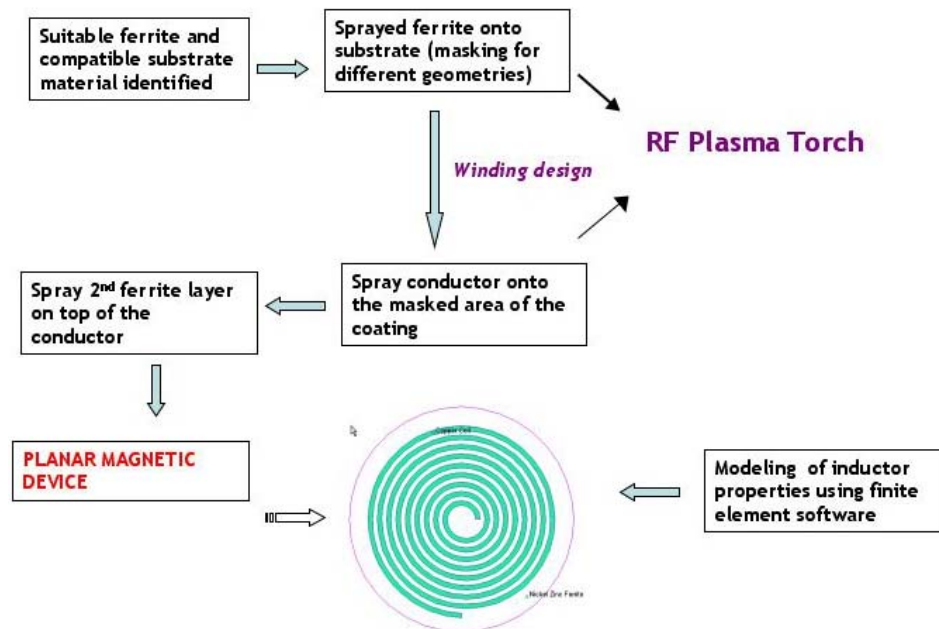
III.4 Nanocrystalline Coatings and Inductive Devices Produced by RF Plasma Synthesis. (ICES PITA support)

A project was funded by the State of PA (PITA) through the CMU Institute for Complex Engineered Systems and used to support MSE graduate student Raja Swaminathan. Funding from Magnetics, Inc. was used as required matching for this program and therefore the program is considered as ancillary to the DUST program. The objectives of the program were to develop nanocrystalline coatings for magnetic passive components in power and high temperature electronic circuits based on plasma torch synthesized ferrite materials. While nanocomposite metal amorphous soft magnetic materials are candidates for inductive devices at moderate frequencies ($<$ 1 MHz), nanocomposite metal/metal oxide and nanocrystalline ferrite soft magnets are candidates for high frequencies (up to 1 GHz). The development of materials in the second area was also argued to benefit from an emerging fundamental understanding of magnetic nanostructure/properties relationships fostered by state of the art characterization tools and understanding of magnetic properties at the nanoscale. The detailed progress in this program is found in the CMU Ph.d thesis of Raja Swaminathan**.**   In this section we present only selected research highlights. The reader is referred to the thesis for a detailed discussion.

III.4.1 Research Highlights – Planar Inductor Design
III.4.1a Planar Inductor Roadmap

R. Swaminathan developed a road map (Figure III.4.2) for his efforts in producing planar inductive devices by RF plasma synthesis. Miniaturization of devices in telecommunication, computers, vehicles and other industrial systems calls for efficient power conversion systems. Planar devices have a higher surface to volume ratio than conventional magnetic designs. Planar power magnetics as the name implies, involves low-profile magnetic components, does away with the mounting bobbin designs and utilizes windings from PCB that can be fabricated using assembly-line design techniques.

Figure III.4.1: Proposed roadmap for the fabrication of a planar inductor.
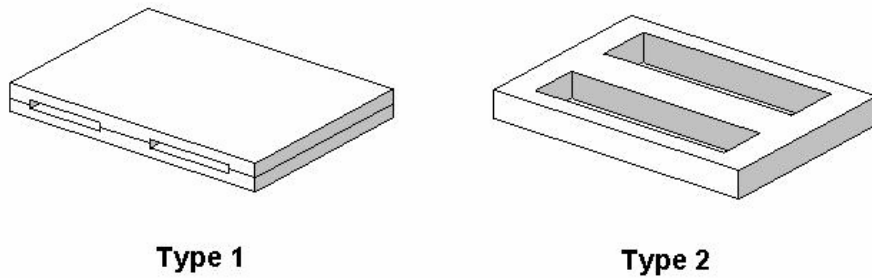
To fuel the increasing demand for new low- profile approaches for low- cost planar magnetic design, nanocrystalline coatings for magnetic passive components in power and high temperature electronic circuits were proposed to be developed using the RF plasma synthesis technique. This involves plasma spraying ferrite coatings on suitable substrates as rectangular and toroidal geometries using masks. To develop passive components for high frequency (close to ~ 1 GHz) applications, NiZn ferrite was chosen as the coating material. Since these ferrites also have low resistivities, eddy current losses in the inductive device can also be minimized. The general road map for the development of planar devices focused upon:

Substrate material: The choice of the substrate considered the compatibility of the thermal expansion coefficients (α) of the substrate and the ferrite. Differences in α between the substrate and the ferrite can lead to de-lamination from the substrate, or if the ferrite tends to adhere well, strain-induced anisotropy can degrade the material's performance. Typical values of α for NiZn ferrites are 7.1-10.1 x $10^{-6}/^0$C. So, the α of the substrate should be close to this value to minimize the interfacial stresses between the substrate and coating that arises during the coating processes. Alumina, Beryllia, Forsterite and Pt were identified as prospective substrate materials based on their thermal expansion coefficients. A PCB material developed by Dupont (which is used in industry for typical planar magnetic devices) having α = 8-10 x $10^{-6}/^0$C was also identified for use once the operating parameters in the plasma torch for the coating has been optimized.

Plasma torch operating parameters: like the gas rate, powder feed rate, substrate preheat, torch- substrate distance, deposition rate and the deposition time must be optimized for better coating properties. Substrate preheating reduces substrate cracking and promotes a good film-to-substrate bond[1,2]. The choice of the plasma torch arc gas is also an important aspect in obtaining the correct crystal structure of the coating material[1]. Adherence of the coatings to the substrate can be assessed using the transmission electron microscope (TEM).

Mask design: were considered for deposition of typical ferrite coil geometries like rectangular, E-core (Figure III.4.2) and toroidal windings as well as spiral coil inductors.

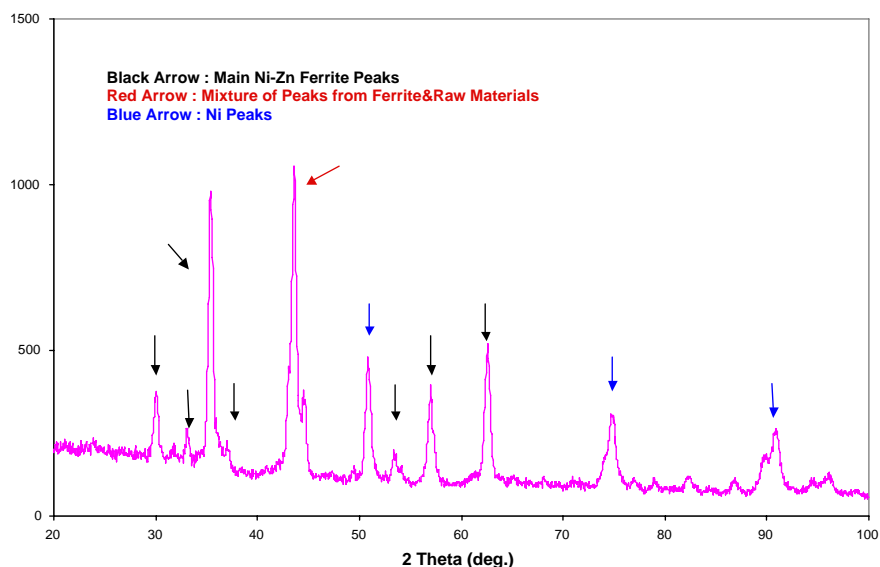### Planar Geometries for E Cores

Type 1   Type 2

Figure III.4.2: Planar geometries for E-cores[3] (J. Huth, *Magnetics, Inc.* private communication).

Strategies for depositing conductors for the planar devices include choice of conductors aimed at minimizing heat losses (I^2R) in the device. The temperature dependence of the resistivity for various conductors has been considered evaluated.[4,5] Copper and Silver have the lowest resistivity and temperature coefficient among the metals and alloys and therefore are the best choice of the conductors among the metals.

III.4.1b Coating Trial

A coating trial was performed to evaluate the efficacy of plasma synthesized ferrite coatings. NiZn ferrites were sprayed onto Alumina substrates using the following plasma torch operating conditions:
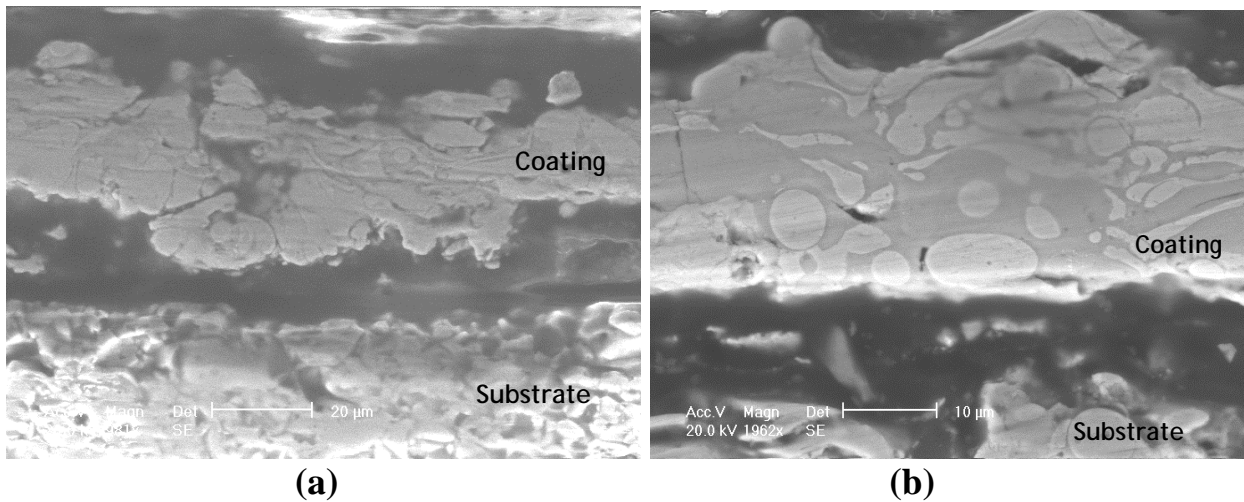
1. An Alumina ceramic disc (2mm thick, 1" diameter) was used as the substrate material. A water-cooled hollow Cu rod connected to a solid Cu block was used as the substrate holder.
2. The distance of the substrate holder from the bottom flange of the plasma torch was 20".
3. The substrate was preheated for about 30 seconds before the powder feeder was turned on.
4. A deposition time of 10 minutes yielded a coating thickness of ~100 μm (characterization detailed later).

Black Arrow : Main Ni-Zn Ferrite Peaks
Red Arrow : Mixture of Peaks from Ferrite&Raw Materials
Blue Arrow : Ni Peaks

Figure III.4.3: X-ray diffraction patterns of the coating on Alumina substrate.

NiZn ferrite was thermally sprayed at a deposition rate of 80 nm/s yielded a 50 μm thick, fairly uniform and adherent ferrite coating on the substrate. The coating was structurally characterized by XRD and SEM. XRD patterns were indexed to a spinel ferrite crystal structure and the SEM micrographs indicated the uniform coverage and adherence of the coating to the substrate. The EDX (Energy dispersive X-rays) analysis of the coating confirmed that the composition of the coating was close to the stoichiometric value ($Ni_{0.5}Zn_{0.5}Fe_2O_4$).

An XRD pattern for the NiZn-ferrite coating is shown in Figure III.4.3. The diffraction pattern shows major peaks corresponding to a NiZn ferrite phase and minority peaks present indicating some of the raw powder passed unreacted through the plasma torch. SEM micrographs of the interface structure are shown in Figure III.4.4. Figure III.4.4(a) and (b) show the SEM micrographs at scales 20 μm and 10 μm respectively. The interface is seen as the dark layer between the coating and the substrate. This interface is impregnated by the resin (used to prepare the mold for cross sectional SEM) peeling off the coating layer from the substrate. It was anticipated that good adherence to the substrate could be ensured by appropriately controlling the plasma torch operating parameters. While the coating trials using the plasma torch were performed on Alumina discs, the PCB material developed by Dupont may be more appropriate.

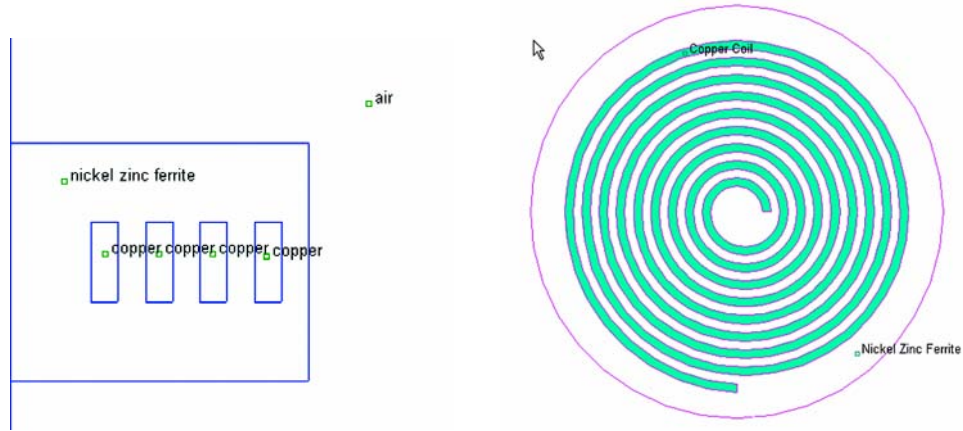**Figure III.4.4**: Structure of the interface observed by cross sectional SEM.

III.4.1c Suggested Masking Techniques and Deposition onto Conductors.

Planar magnetic geometries are recommended to be fabricated using photolithography and ion-beam etching. This is effectively an ex-situ masking technique. Mask geometries can be designed using the traditional software packages, as part of the standard photolithography techniques. For good quality geometries to be obtained using the above-mentioned techniques, the ferrite coating should be ~1-10 μm thick. Once a ferrite has been deposited and a suitable geometry has been patterned using the photolithography and ion-beam etching techniques, a thin layer of insulator (eg: SiO_2) could be deposited for preparing the surface for the deposition of the conductors. The conductors could be sprayed using the plasma torch or by sputtering.
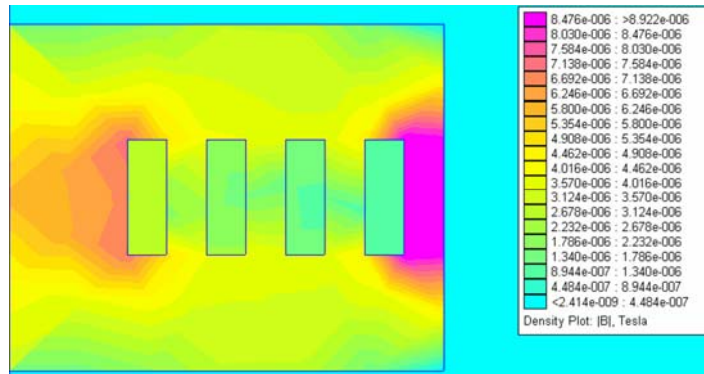
III.4.1d Determination of Coil Geometry.

The determination of an appropriate copper coil geometry for an ideal planar inductor was performed by Rob Rencwicz (ICES-SURE Thing undergraduate researcher) following an extensive literature search A spiral geometry was chosen as the ideal geometry to provide both the highest inductance and minimize the losses. Finite element software packages including FEMLAB©, FEMME© and FLEXPDE© were investigated to determine the fabrication parameters for the planar inductor like the number of turns of the coil, thickness of the Cu in the coil, thickness of the ferrite layer, radius of the core etc. This analysis was based on a combination of NiZn ferrite as a core material with a spiral Cu coil. The geometry used in FEMME to simulate the effects of various parameters and frequencies is shown in Figure III.4.5.

FEMME© was chosen because it was simple to use and a planar inductor can be simulated without a great degree of difficulty. FEMLAB© was reasonable for direct simulation of 3-D models of inductors (as opposed to an indirect method used in FEMME), but it is time-consuming to simulate even a simple geometry. FLEXPDE© was also considered as a modeling tool. In the axisymmetric mode used in the FEMME model, the cross section is defined and the entire structure is rotated about the y-axis to create a 3-d object. The axisymmetric mode was used as opposed to the planar mode, since the defined current direction is into the plane of the paper. The path of current (in the axisymmetric model) is defined by the use of concentric rings and is a very good approximation to the spiral geometry[6].

34

Figure III.4.5: (a) Cross-sectional and (b) top view of the planar inductor model using FEMME.

The magnetic induction profile for the geometry in Figure 15(b), as analyzed by FEMME, is shown in Fig.III.4.6. The losses in the inductor (eddy current and resistive) were also calculated using this software for various frequencies and materials/fabrication parameters. The results obtained were in reasonable agreement with literature. We investigated only the low-frequency range (up to 1 MHz) for the losses and the various material and fabrication parameters by ignoring the displacement currents (which is important in radio frequency applications). Improvements made to the model include better characterization of the AC properties, evaluation of the inductance and incorporation of the laminations in the copper coil (to prevent the under-utilization of the copper due to skin-depth effects).

Figure III.4.6: Density plot of the magnetic induction profile in the planar inductor
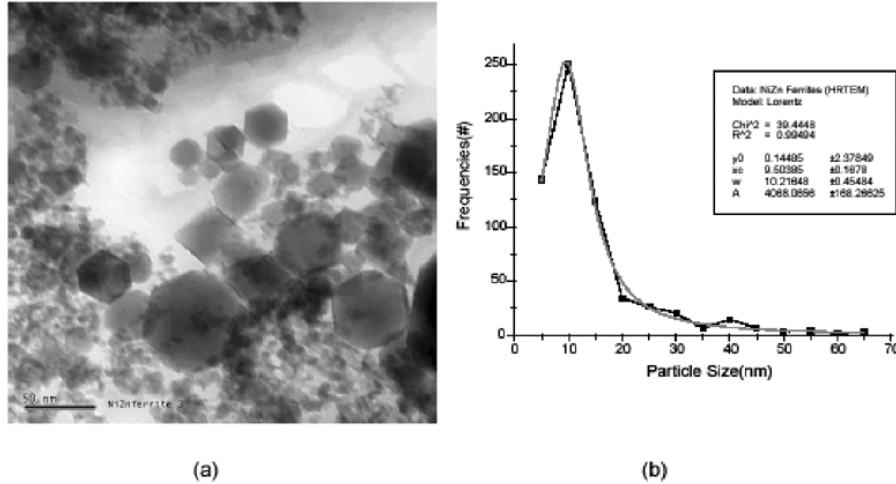
III.4.2 Research Highlights – Ferrite Nanoparticle Synthesis, Structure and Properties.
III.4.2a Experimental Observations

In nanocrystalline materials, an increased fraction of atoms at the surface that are not fully coordinated contribute differently to properties than in the bulk material. In nanocrystalline oxides (like spinel ferrites) it is more important to consider magnetic cation coordination polyhedral units as the basic structural units determining properties. We explored the Ni-Zn ferrite nanoparticles synthesized using a RF plasma torch by techniques including Mossbauer spectroscopy (in collaboration with Prof. Monica Sorescu, Duquesne Univ.) and extended x-ray absorption fine structure spectroscopy (EXAFS, in collaboration with Scott Calvin, NRL and Sarah Lawrence College). The morphology of the polyhedral surface structure of the ferrite nanoparticles was determined by TEM. The observed morphologies were used to interpret the

Mossbauer spectroscopy and EXAFS results and were used to discuss triangular spin structures at the (111) surfaces of these materials.

Bright field (BF) TEM observations revealed [Figure III.4.6] cuboctahedral-type polygonal growth forms with (100) and (111) facets. The particle size distribution was determined (based on BF images of 638 randomly selected particles) to be log-normal with a fit yielding an $R^2 = 0.995$. The number-weighted average particle size was 11.7 nm.

Figure III.4.7: (a) Bright field TEM images of NiZn ferrite nanoparticles (b) Particle size distribution based on 638 randomly chosen particles

Mossbauer spectra (Table III.4.1) were fit to five sextets and two doublets. The isomer shift values are consistent with a high-spin Fe^{3+} state on the tetrahedral and the octahedral sites. A sextet, with a hyperfine field of 49.7 T corresponded to tetrahedral (A) sites and B1, B2, B3 and B4 sextets corresponded to octahedral sites. The inequivalent B sites originate from a Fe^{3+} octahedral site having different nearest neighbor Zn atoms in the tetrahedral sites. Two superparamagnetic doublets in the Mossbauer spectrum account for 29% of the relative spectral areas. The fact that the particle size distribution was well described by a log-normal distribution suggests that two superparamagnetic doublets can be attributed to a bimodal distribution of the anisotropy energy barrier to thermal switching of these particles. The linewidth of the tetrahedral sites in the nanoparticle Mossbauer spectrum (0.47mm/s) was considerably larger than the linewidths associated with the A-sites in bulk Ni-Zn ferrite and attributed to distinctions between surface A sites in the spinel surface having tetrahedral apices pointing in and out of (111) planes.

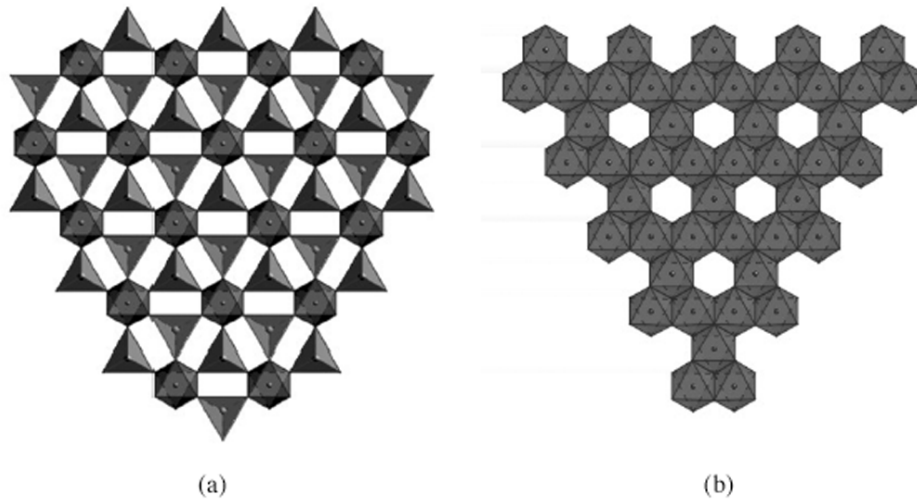| H_{hf} (T)	IS (mm/s)	QS (mm/s)	Relative areas	Γ (mm/s)	Site assignment
49.7	0.27	-0.25	21.9	0.47	Fe^{3+} A
52.8	0.31	-0.1	5.7	0.40	Fe^{3+} B1
49.5	0.33	0.23	13.0	0.36	Fe^{3+} B2
46.3	0.60	-0.12	17.4	0.5	Fe^{3+} B3
44.4	0.50	-0.17	13.0	1.5	Fe^{3+} B4
-	0.59	0.28	10.0	0.45	Superparamagnetic
-	0.62	1.34	19.0	0.63	Superparamagnetic

Table III.4.1: The fitted Mossbauer parameters of the NiZn ferrite nanoparticles. IS values given relative to α -Fe.

It was established, from the Fourier transform of the EXAFS spectra that the Fe cations reside in both tetrahedral (A) sites and octahedral (B) sites, while the Ni cations reside nearly exclusively in B sites. Both results are consistent with the Mossbauer estimates. The sample's Zn edge, while consistent with the first-shell environment of a spinel, shows a substantial suppression at greater scattering distances. This suppression is consistent with a Zn^{2+} concentration gradient in the nanoparticles, with Zn^{2+} more concentrated at the surface of the particles (where surface truncation reduces the second neighbor coordination). Important features of the zero-field cooled hysteresis loops (at 5 K) include the non-saturation of the moments up to an applied field of 5 T and an "open" hysteresis loop up to 2.25 T.
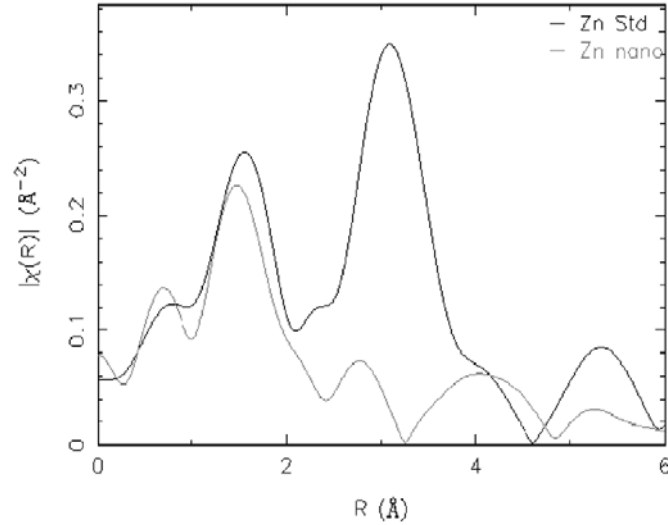
III.4.2b Surface Crystallography

Understanding the surface structure of ferrite nanoparticles is important to understand the effects of reduced coordination (due to truncation) of the cations on ferromagnetic exchange and magnetocrystalline anisotropy. The majority of nanoparticles had morphologies with truncated octahedral shapes, with a higher proportion of (111) than (100) surfaces. We modeled the (111) surface structure of the ferrite nanoparticles by considering the various possible (111)- type truncations in the polyhedral arrangement of the spinel structure. Figs.III.4.8 (a) and (b) illustrate two types of (111) planes with different arrangements of the surface polyhedral units. The (111)-mixed plane consists of both the tetrahedral and the octahedral polyhedra, whereas the (111)-octahedral plane consists only of the octahedral polyhedra. In the (111)-mixed planes, half the tetrahedra have their apices pointing up and the other half have apices pointing down. These are symmetrically equivalent sites in an infinite crystal but are distinct for (111) terminated surfaces. In nanoparticles truncated by the (111)-mixed plane, the tetrahedra that have their apex pointing upward will see a different crystal field than those with their apex pointing into the bulk. We proposed that this difference in the electronic environment between these inequivalent A-sites in the truncated (111) surfaces causes the increased Mossbauer linewidth in the nanoparticles.

(a)   (b)

Figure III.4.8: The (a) mixed and (b) pure octahedral (111) planes in the spinel structure.

The tetrahedral linewidth of the Ni ferrite nanoparticles was 0.8mm/s, indicating that more of the Fe^{3+} ions are on the surface tetrahedral units of the (111)-mixed planes in Ni ferrites than in Ni-Zn ferrites. This is indirect evidence of a higher surface Zn concentration in Ni-Zn ferrite nanoparticles. These observations are also consistent with the reduced EXAFS spectral

density in the Zn-edge associated with bonds between A-site and B-site cations [Fig. III.4.9]. Since there was no reduction in the EXAFS amplitude of the nearest neighbor metal-oxygen bonds, we proposed that the truncations take place by preserving the polyhedral subunits with the second near neighbor cation-cation (Zn-Fe) distances being affected.
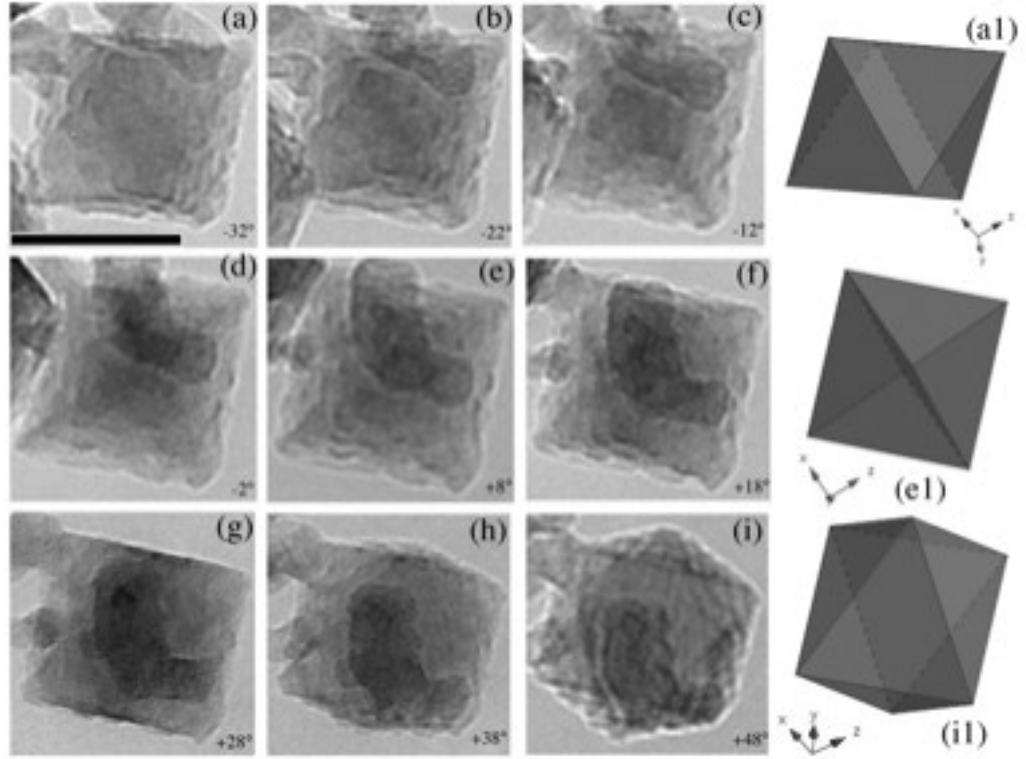

Figure III.4.9: Fourier transformed Zn-edge EXAFS spectra

Our results led us to propose that truncated ferrite nanoparticles have primarily (111)-mixed type truncations and Zn^{2+} migrates to these surfaces. This leads to reduced A-O-B interactions and magnetization on the surfaces and large fields required to saturate the moments. There is a 37.5% reduction in the A-O-B interactions on the (111)-mixed surface as compared 25% for the B-O-B interactions. At the (111)-mixed surface, the total exchange field is reduced by a combination of the reduced coordination for both the A-B and the B-B interactions. This effect, coupled with the increased Zn concentration at the surface acts to substantially reduce the A-O-B interactions in the nanoparticles. According to Yafet and Kittel, a B-sub-lattice triangular configuration is possible when the molecular field of B-B interactions is larger than the field of the A-B interactions. We therefore postulated a triangular B-spin arrangement on the (111) surfaces of these nanoparticles due to the two-fold effect in the reduction of A-B interactions. The non-saturation of the moments up to an applied field of 5 T and an open hysteresis loop up to 2.25 T also gave evidence to the triangular spin structure present on the surface. Surface spin canting has been attributed to the broken exchange bonds due to missing oxygen atoms from the surface. We observe that the broken exchange bonds are exacerbated not due to missing oxygen atoms, but due to the second near neighbor broken bonds.
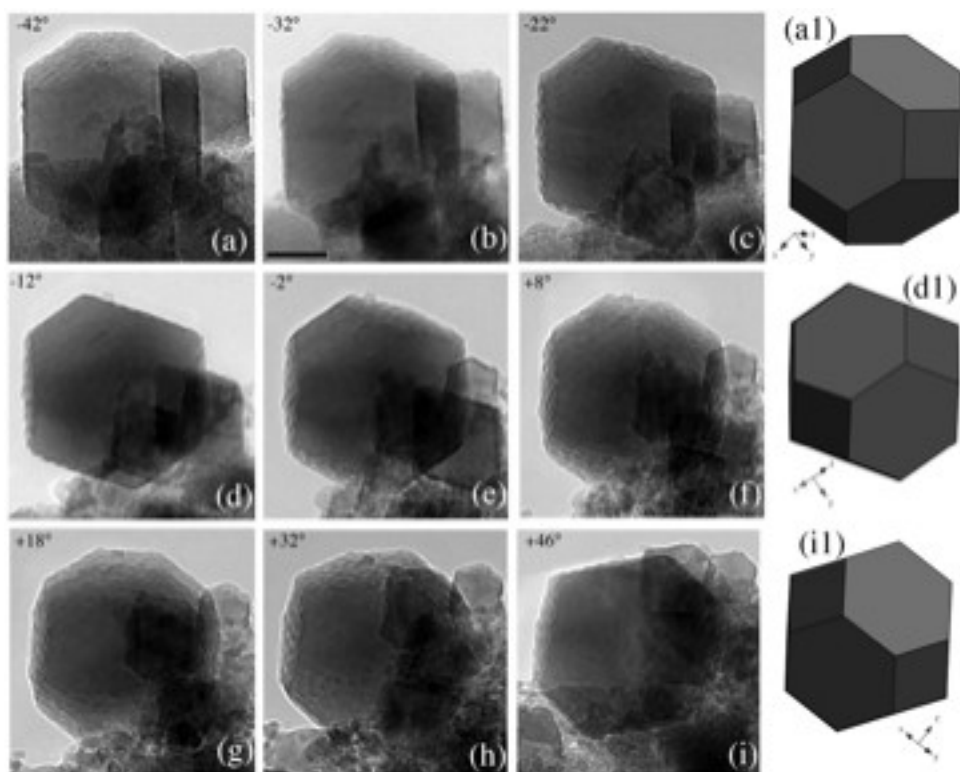
III.4.2b Electron Tomography
The 2-d projection TEM images of NiZn ferrite nanoparticles synthesized using the RF plasma torch suggested that particles exhibit cuboctahedral morphologies with exclusively (100) and (111) type facets. The projected images also indicated that the small particles (< 20 nm) are octahedral while the larger particles (20-50 nm) were truncated octahedral in shape. To confirm the 3-d morphologies of the nanoparticles, tilt experiments (Figure III.4.10) were performed on selected areas, with a single nanoparticle in focus, using a single-tilt specimen holder on a TECNAI FEG TEM (F20 model).

Figure III.4.10: Projected morphologies [(a)-(i)] at different tilt angles for an octahedral nanoparticle. (a1), (e1) and (i1) are projections of model octahedron. Scale bar is 20 nm.

A series of images (recorded at 2° tilt intervals) over a tilt range of ± 45° (with respect to the primary electron beam) were recorded using the attached CCD camera. Image shifts and focus changes were performed for all tilt angles to always keep the nanoparticle in the field of view. Since the ferrite nanoparticles are remarkably stable to electron exposure over long time periods, over-dosage of electrons to the sample is not a problem while obtaining a number of images in the specific area. The recorded series of 2D images were manually aligned, stacked and then rotated in the corresponding tilt range to obtain the 3D perspective of particle morphology shape, instead of using 3D reconstruction routines [2]. These image series for the smallest [Figure III.4.10(a)-(i)] and largest [Figure III.4.11(a)-(i)] particles were then compared to the 3D rotation models of the octahedron and truncated octahedron respectively. The different projections of the model octahedron [Figure III.4.10(a1), (e1) and (i1)] and the truncated octahedron [Figure III.4.11(a1), (d1) and (i1)] are shown for comparison. For example, Figure III.4.10(a1) is the projection image of the model octahedron representing the particle in Figure III.4.10(a). The 3D nanoparticle morphological observations validate our nucleation and growth models of the particles in plasma, according to which, the critical nucleus shape, which is the shape of the smallest nanoparticle is a perfect octahedron while the growth forms, which represent the larger particles are truncated octahedra.

Figure III.4.11: Series of 2-d projected morphologies [(a)-(i)] for a large truncated octahedral nanoparticle. (a1), (d1) and (i1) are different projections of model truncated octahedron. Scale bar on (b) is 20 nm.

III.4.2c Sintering Experiments

In order to characterize the AC magnetic properties of nanoparticles they were compacted and sintered. RF plasma synthesized ferrite nanoparticles were compacted and sintered in cylindrical shapes and their structure and densities were characterized at each processing stage. The compactions were performed using a Carver press with a maximum pressure of 5000 psi with and without the presence of a binder (PVA). The sintering profile for the compacts included a step to completely evaporate the binder (at 800°C) and a step to induce the actual sintering of the nanoparticles at 1100°C. The densities of the material were measured using a pycnometer.

Experimental results and the proposed surface structure model were presented in the 9th MMM-InterMag conference in January 2004. An extension of the surface structure model was published in the 9th International Conference on Ferrites (Aug. 2004), where it was presented as an invited talk. Work on ferrite nanoparticles was presented as an invited talk at the Spring 2005 MRS Meeting in San Francisco, California by Michael McHenry. Raja Swamnathan presented a separate paper on the sintering behavior of ferrite nanoparticles (work performed in collaboration with Magnetics, Inc.). Raja defended his thesis May 11, 2005. Work on electron tomography of ferrite nanoparticles was presented at the July 2005 Microscopy Society of America Conference and published in the conference proceedings. *The gas phase nucleation and growth model for ferrite nanoparticles was submitted at the time of the DUST final review but had not been accepted for publication. It is now in press and a proof copy is included in Appendix IV.*

References

1. "The effect of substrate materials and powder type on the properties of plasma sprayed ferrite" C.W.D. Andrews, B.A.Fuller, *Journal of Materials Science* **10** (1975) 1771-1778
2. "Microstructure and Magnetic Properties of Ferrite Films Prepared by Plasma Jet Spraying" Hiroshi Maeda *et.al*. *Transactions of National Research Institute for Metals* **19** No.4 (1977) 171-177
3. Fig. *Courtesy* Joseph Huth, Magnetics, Inc. (private communication)
4. CRC Materials Science and Engineering Handbook 2nd edition, CRC Press, 1994
5. http://home.san.rr.com/nessengr/techdata/metalresis.html#metal
6. *Planar Inductors on Magnetic Substrates*, W.A.Roshen and D.E.Turcotte, IEEE Transactions on Magnetics, 24(6), 3213-6.

Appendix I: Publications of DUST and DUST-related Research Efforts

Magnetic and Structural Characterization and Ferromagnetic Resonance Study of Thin Film HITPERM Soft Magnetic Materials for Data Storage Applications. H. Okumura, D. J. Twisselmann*, R. D. McMichael*, M. Q. Huang, Y. N. Hsu**, D. E. Laughlin** and M. E. McHenry**, J. Appl. Phys. 93, 6528-6530, (2003).

Structure and Magnetic Properties of Thermally Plasma Synthesized Mn and Mn-Zn Ferrite Nanoparticles. S. Son, R. Swaminathan, and M. E. McHenry, J. Appl. Phys. 93, 7495-7497, (2003).

The Kinetics of Nanocrystallization and Implications for Properties in FINEMET, NANOPERM and HITPERM Nanocomposite Magnetic Materials. M. E. McHenry, F. Johnson, H. Okumura, T. Ohkubo, A. Hsiao, V. R. V. Ramanan and D. E. Laughlin; (invited), Irsee, Germany, June, 2002, Scripta Mat. 48/7, 881 - 887. (2003).

Magnetic and Structural Properties and Crystallization Behavior of Si-rich FINEMET Materials. H. Okumura, M. E. McHenry and D. E. Laughlin, J. Magn. Magn. Mat.267, 347-356, (2003).

Magnetic Properties of Co-substituted Fe-Nb-B-Ta-Mo Bulk Amorphous Alloys. C. Um and M. E. McHenry, IEEE Trans. Mag. 40 (4): 2697-2699, (2004).

Induced Anisotropy in FeCo-based Nanocrystalline Ferromagnetic Alloys (HITPERM) by Very High Field Annealing. F. Johnson, H. Garmestani, S. Y. Chu, M. E. McHenry and D. E. Laughlin, IEEE Trans. Mag. 40 (4): 2724-2726 (2004).

Structure and Magnetic Switching of Thin Film HITPERM/SiO_2 Soft Magnetic Multilayers.. H. Okumura, C. Um, S. Chu, D. E. Laughlin, M. E. McHenry, and A. B. Kos, MMM/Intermag Anaheim 2004, to appear in IEEE Trans. Mag. 40(4): 2700-2702 (2004).

Magnetic and Structural Properties of Nickel Zinc Ferrite Nanoparticles Synthesized at Room Temperature. S.A. Morrison, C. L. Cahill, E. E. Carpenter, S. Calvin, R. Swaminathan, M. E. McHenry and V. G. Harris, J. Appl. Phys. 95 (11): 6392-6395, (2004).

Surface Structure Model of Cuboctahedrally Truncated Ferrite Nanoparticles. R. Swaminathan, M. E. McHenry, S.Calvin, M.Sorescu and L.Diamandescu, to appear in ICF Proceedings, J. Amer. Cer. Soc. (2005).

Structural and Magnetic Properties of NiZn and Zn Ferrite Thin Films Obtained by Laser Ablation Deposition. M. Sorescu1, L. Diamandescu, R. Swaminathan, M. E. McHenry, and M. Feder, J. Appl. Phys. (2005).

Effect of Crystal Fraction on Hardness in FINEMET and NANOPERM Nanocomposite Alloys. C.-Y. Um, F. Johnson, M. Simone, J. Barrow, and M. E. McHenry, J. Appl. Phys. (2005).

Magnetic Properties of Polydisperse and Monodisperse NiZn Ferrite Nanoparticles Interpreted in a Surface Structure Model. R.Swaminathan, M. E.McHenry amd H. Srikanth, J. Appl. Phys. (2005).

The Influence of Composition and Field Annealing on Magnetic Properties of FeCo-base Amorphous and Nanocrystalline Alloys. F. Johnson, C. Y. Um, M. E. McHenry, and H. Garmestami, J. Mag. Mag. Mat. (2005).

The Influence of Composition and Field Annealing on Magnetic Properties of FeCo-base Amorphous and Nanocrystalline Alloys. F. Johnson, C. Y. Um, M. E. McHenry, and H. Garmestami, J. Mag. Mag. Mat. (2005).

Surface Structure Model of Cuboctahedrally Truncated Ferrite Nanoparticles. R. Swaminathan, M. E. McHenry, S.Calvin, M.Sorescu and L.Diamandescu, Proc. 9th International Conference on Ferrites, 847-52, (2005).

Thermal Behavior of Substituted FeCo-based Metallic Glasses. M. Sorescu, C. –Y. Um, M. E. McHenry and L. Diamandescu, J. Non-Crys. Sol. **xxx**, xxx, (2005).

3-dimensional Morphologies of Truncated Ferrite Nanoparticles R. Swaminathan, N.T. Nuhfer and M.E. McHenry, Microsc Microanal **11** (Suppl 2),1904, 2005.
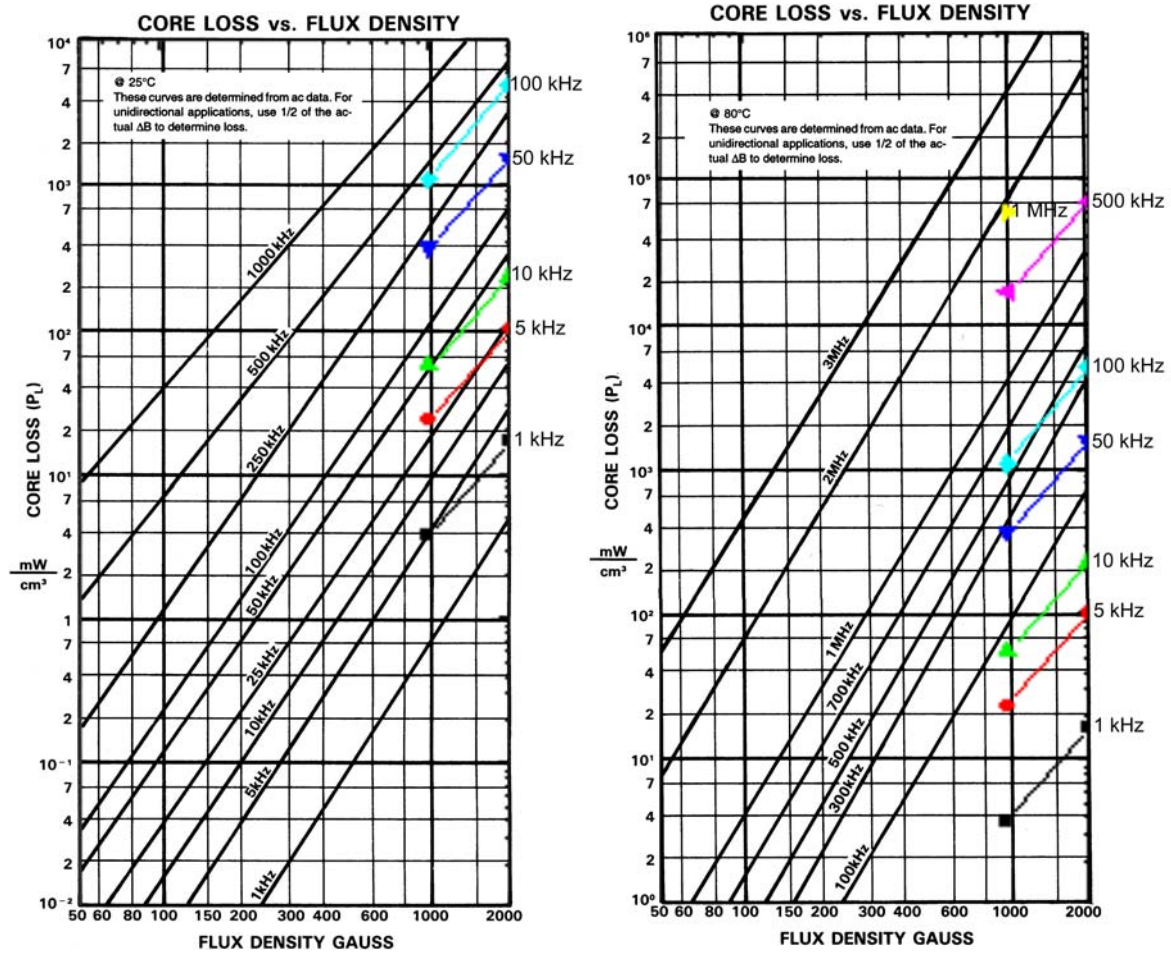
Appendix II: Apparatus Used in Material Science Department in DUST Program

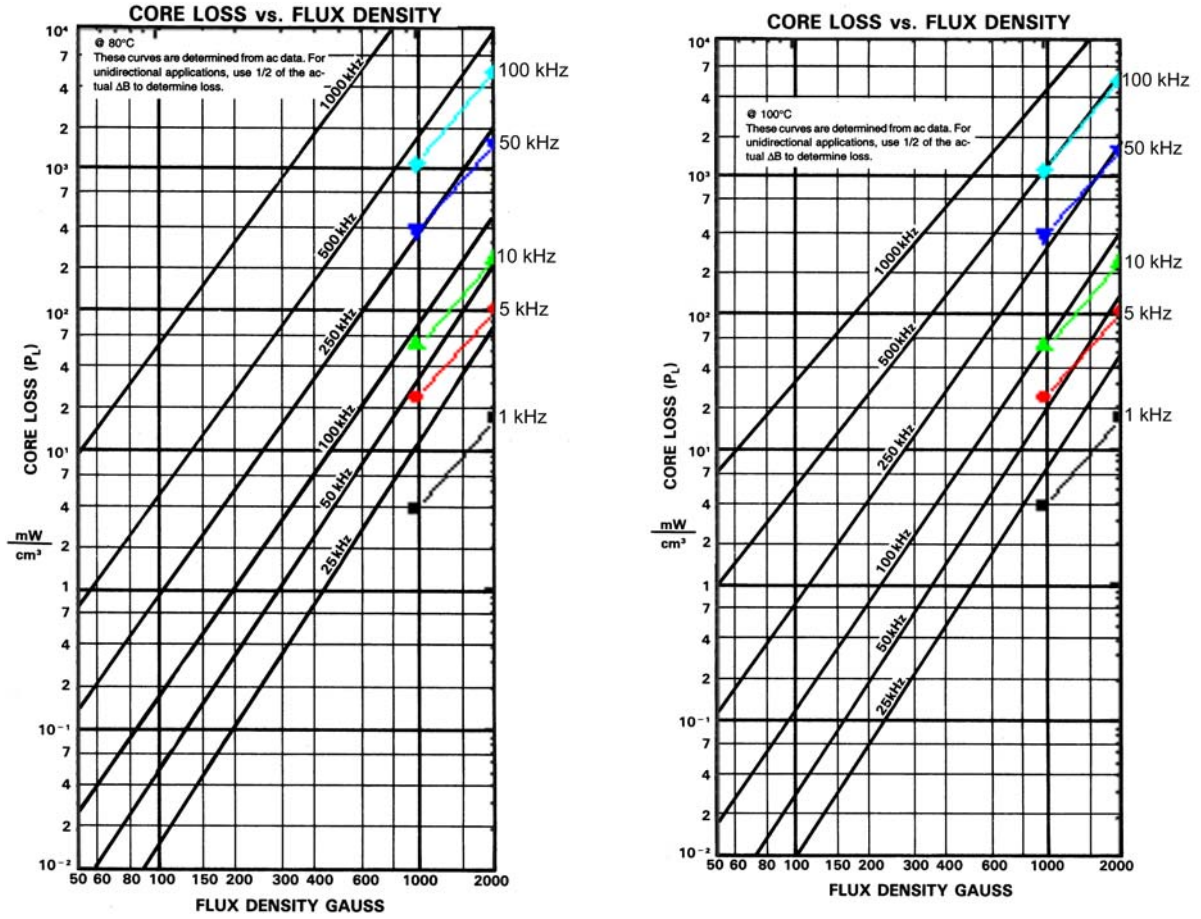| Apparatus	Supplier	Address	Phone	Location (CMU)
Vibrating Sample Magnetometer (VSM)	Lake Shore Cryogenics, Inc.	575 McCorkle Blvd. Westerville, OH 43082	614-891-2244	Wean Hall, 7403
Permeameter/ HysteresisGraph AMH- 401 POD	Walker Scientific, Inc.	Rockdale Street Worcester, MA 01606	1-800-962-4638 508-852-3674	Roberts Hall, 207
Differential Scanning Calorimetry (DSC)	Perkin Elmer, Inc.	45 William Street Wellesley, MA 02481-4078	781-237-5100	Roberts Hall, 226
Transmission Electron Microscopy (TEM): High Resolution	Philips Tecnai	22100 Bothell Everett Highway P.O. Box 3003 Bothell, WA 98041-3003	1-800-722-7900 425-487-7000	Roberts Hall, 123
Transmission Electron Microscopy (TEM): Conventional	Joel JEM-2000EX II			Roberts Hall, 126
X-Ray Diffractometer (XRD)	Rigaku /MSC	9009 New Trails Drive The Woodlands Texas USA 77381-5209	281-363-1033	Roberts Hall, 132
X-Ray Diffractometer (XRD)	Philips X'Pert	22100 Bothell Everett Highway P.O. Box 3003 Bothell, WA 98041-3003	1-800-722-7900 425-487-7000	Roberts Hall, 133
Scanning Electron Microscopy (SEM)	Phillips XL30	22100 Bothell Everett Highway P.O. Box 3003 Bothell, WA 98041-3003	1-800-722-7900 425-487-7000	Roberts Hall, 128
Plasma Torch	Tekna Plasma Systems, Inc.	2935 Boulevard Industrial Sherbrooke, Quebec, Canada J1L 2T9	819-820-2204	Roberts Hall, 207

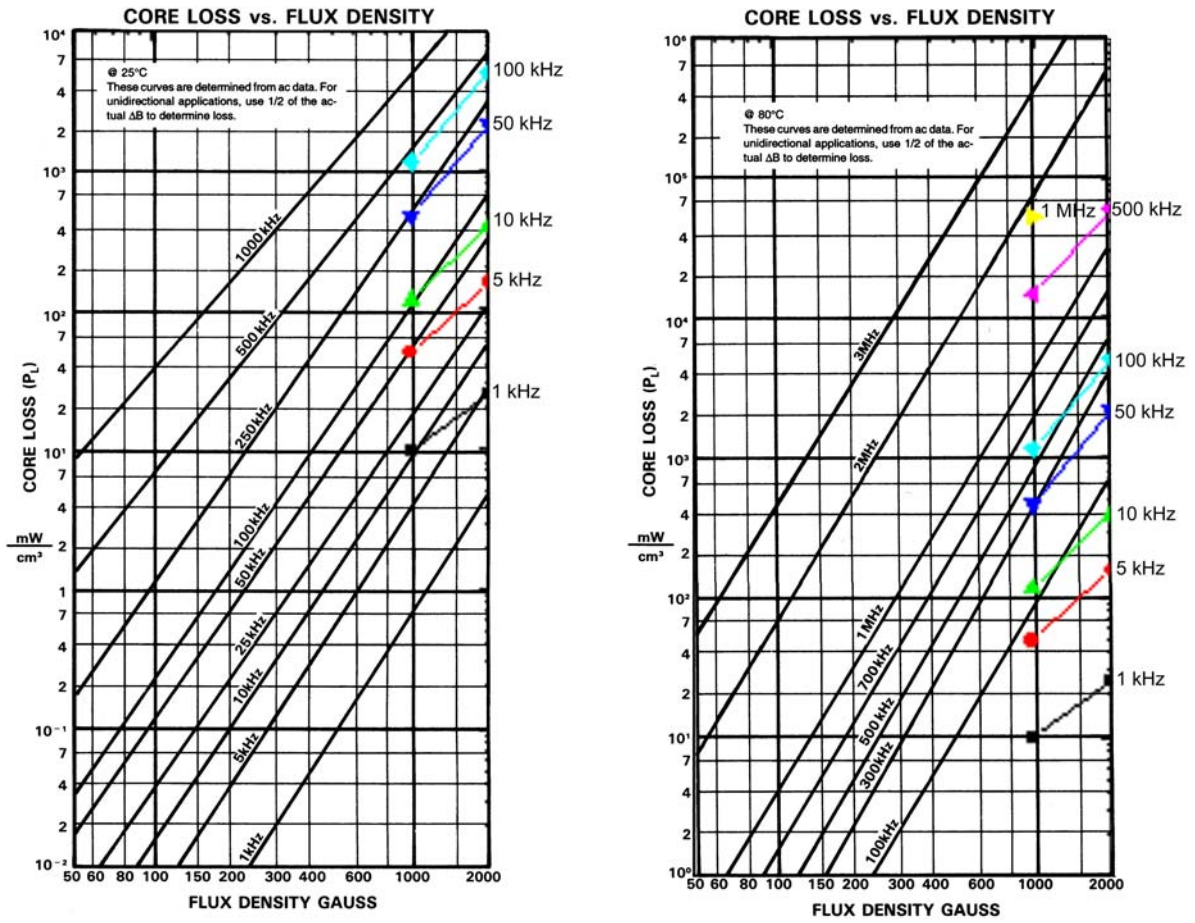|				
Physical Property Measurement System (PPMS)	Quantum Design	6325 Lusk Boulevard San Diego, CA 92121-3733, USA	1-858-481-4400	Roberts Hall, 307
Super Conducting Quantum Interference Device (Sample Property Measurement System)	Quantum Design	6325 Lusk Boulevard San Diego, CA 92121-3733, USA	1-858-481-4400	Roberts Hall, 307
High Energy Mill	SPEX CertiPrep	203 Norcross Avenue Metuchen, NJ 08840	1-800-LAB-SPEX 712-549-7144	Roberts Hall, 207
Mathematica 5.1 for Students	Wolfram Research, Inc.	100 Trade Center Drive Champaign, IL 61820-7237	1-800-965-3726 217-398-0700	Wean Hall, 7403
Solidworks: Finite Element Modeling Software	Solid Works Corporation	3000 Baker Avenue Concord, MA 01742 USA	1-800-693-9000	Wean Hall, 7403
Melt Spinner	Santoku			Roberts Hall, 207

Appendix III: Benchmark core loss comparisons between HITPERM and Magnetics ferrite cores.
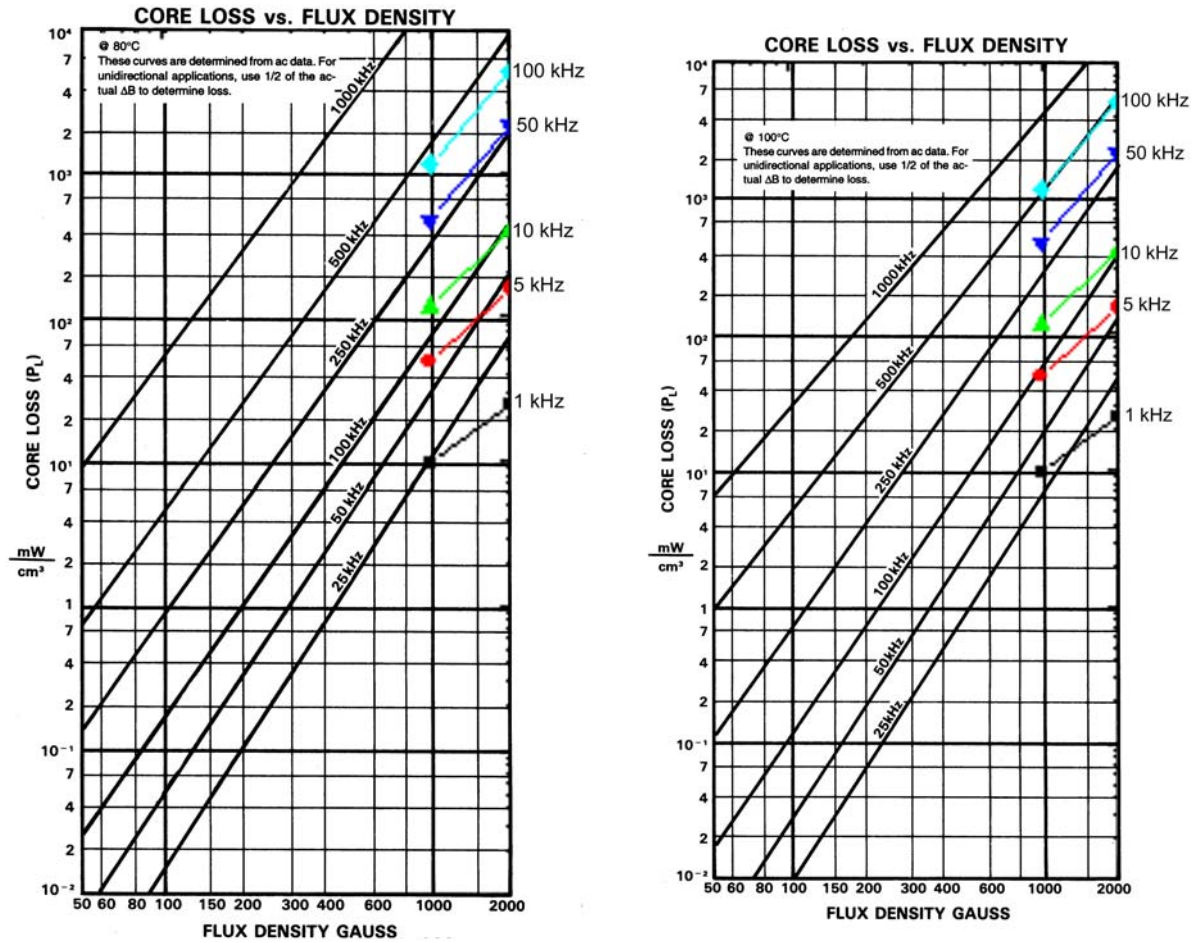

Figure A1: (a) Core loss vs. flux density comparison for F ferrite material (black lines) and field annealed HITPERM (colored lines) (b) Core loss vs. flux density comparison for K ferrite material (black lines) and field annealed HITPERM (colored lines).

Figure A2: (a) Core loss vs. flux density comparison for P ferrite material (black lines) and field annealed HITPERM (colored lines) (b) Core loss vs. flux density comparison for R ferrite material (black lines) and field annealed HITPERM (colored lines).

Figure A3: (a) Core loss vs. flux density comparison for F ferrite material (black lines) and field annealed HITPERM (colored lines) (b) Core loss vs. flux density comparison for K ferrite material (black lines) and field annealed HITPERM (colored lines).

Figure A4: (a) Core loss vs. flux density comparison for P ferrite material (black lines) and field annealed HITPERM (colored lines) (b) Core loss vs. flux density comparison for R ferrite material (black lines) and field annealed HITPERM (colored lines).

Experimental observations and nucleation and growth theory of polyhedral magnetic ferrite nanoparticles synthesized using an RF plasma torch

R. Swaminathan [a,*], M.A. Willard [b], M.E. McHenry [a,*]

[a] *Department of Materials Science and Engineering, Carnegie Mellon University, Pittsburgh, PA 15213, United States*
[b] *US Naval Research Laboratory, Physical Metallurgy Branch, Code 6320, Washington, DC 20375, United States*

Abstract

We have used transmission electron microscopy (TEM) to observe the morphologies of ferrite nanoparticles synthesized using a radio frequency plasma torch. These nanoparticles were faceted, having cuboctahedral polygonal growth forms with exclusively the {111} and {100} type faces. A model for the critical nucleus shapes and the growth forms of small cuboctahedral particles is proposed considering the Helmholtz free energies for nucleation and growth. The critical nucleus shape is predicted to be either a perfect cube or a perfect octahedron, while the equilibrium growth forms are the truncated shapes. High-resolution TEM observations of individual nanoparticles reveal that the smallest nanoparticles exhibit perfect octahedral shapes, while larger particles have truncated octahedral shapes. These observations are consistent with the model predictions. The morphology observations are also consistent with $0.95 < \frac{\gamma_{100}}{\gamma_{111}} < 1.14$, where γ_{100} and γ_{111} are the surface energies of the (100) and (111) surfaces, respectively.
© 2005 Acta Materialia Inc. Published by Elsevier Ltd. All rights reserved.

Keywords: Ferrite nanoparticles; High-resolution TEM; Polyhedral morphologies; Faceting; Critical nucleus and growth shapes

1. Introduction

The relationship between the surface structure and magnetic properties of ferrite nanoparticles [1,2] is of interest in exploring the potential of ferrite nanoparticles [3] for microwave device (100 MHz–1 GHz range) [4,5] and biomedical [6–9] applications (in a surface functionalized form). Faceted magnetite nanoparticles (Fig. 1) have been observed in magnetotactic bacteria [10] and in the Martian meteorite ALH84001 [11–13]. In the magnetotactic bacteria, nature selects magnetite particles ($\approx$50 nm in size) that have truncated octahedral morphologies [14]. The bacteria form chains coupled by magnetostatic interactions, leading

to the sharing of (111) nanoparticle faces. There has been great interest in determining whether the magnetite particles found in ALH84001 have a biogenic origin as the magnetite in the magnetotactic bacteria does [15]. The truncated octahedral shapes are also the most commonly occurring morphologies in the radio frequency (RF) plasma synthesized ferrite nanoparticles, discussed here, suggesting that faceted nanoparticles are common to a variety of processing conditions.

Nanoparticle magnetic properties, including surface exchange and magnetic anisotropy, can differ from the bulk material of the same composition. This difference results from an increased fraction of surface atoms in the nanoparticles that are not fully coordinated [16]. The correlation between specific surface structure, crystallography, and magnetic properties of magnetic nanoparticles is an evolving [17] field. For the ferrite nanoparticles studied here, coordination polyhedral units are considered to be the

---

* Corresponding authors.
E-mail addresses: rs6@andrew.cmu.edu, sgoofy8@gmail.com (R. Swaminathan), mm7g@andrew.cmu.edu (M.E. McHenry).
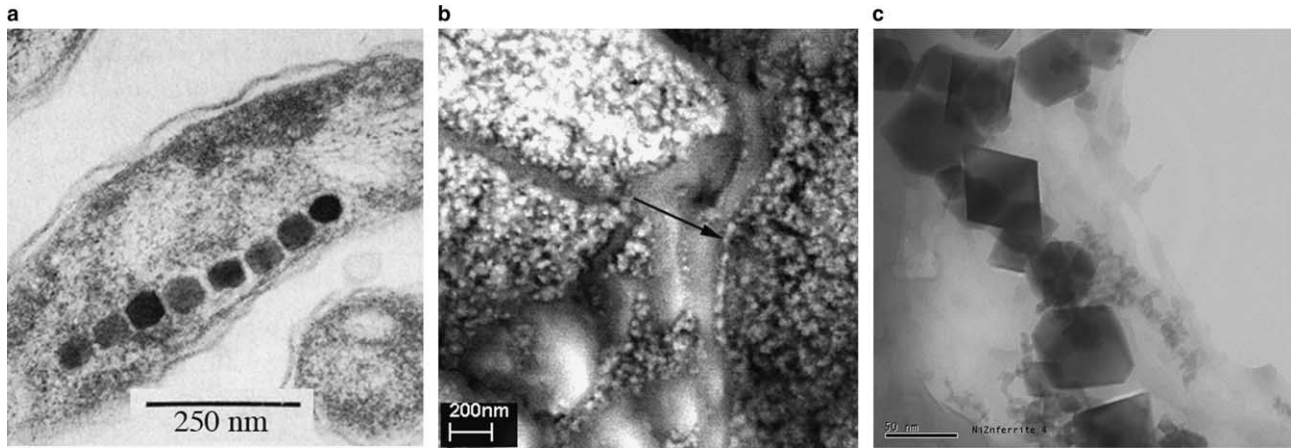
Fig. 1. The morphologies of: (a) ferrite chains in magnetotactic bacteria compared with, (b) magnetite particles in Martian meteorites and (c) RF plasma synthesized ferrite nanoparticles. (a) Reprinted with permission from Frankel et al., Science 203:1355-56 (Mar 30, 1979) AAAS. (b) Reproduced with permission from Friedmann et al. (2001). Copyright (2001) National Academy of Sciences, USA.

basic structural units for describing symmetry reduction at surfaces.

In the spinel structure of the ferrites, the strength and number of oxygen-mediated superexchange bonds [18] determine the temperature dependence of magnetization and the collinear or non-collinear alignment [19] of cation magnetic dipole moments. Exchange bonds are lost normal to surfaces in the nanoparticles. The resulting surface anisotropy, K_s [20], contributes [21] to the effective magnetocrystalline anisotropy, K_{eff}, as expressed:

$$K_{eff} = K_v + sK_s, \tag{1}$$

where K_v is the volume anisotropy contribution and s relates to the shape of the particles. K_s is influenced by the symmetry of the magnetic cation coordination polyhedra at the surface. Different terminating surfaces contribute differently to surface anisotropy and can significantly impact the magnetic properties of small particles.

The RF plasma synthesized ferrite nanoparticles described here exhibit cuboctahedrally truncated morphologies with varying fractions of the (100) and (111) sur-

faces. The influence of (100) and (111) surfaces on the magnetic properties of these nanoparticles has been reported [1]. We consider the surface terminations by the possible arrangements of tetrahedral and octahedral coordination polyhedra. The (100) surfaces exhibit chains of octahedra along the [110] and [1$\bar{1}$0] directions (Fig. 2(a)). The broken four-fold symmetry at these surfaces reflects the fact that the $Fd\bar{3}m$ space group of the spinel structure does not have a four-fold axis, but a 4_1 screw axis.

The two crystallographically distinct (111) surfaces (Fig. 2(b) and (c)) have different hexagonal arrangements of the tetrahedra and octahedra. In these nanoparticle systems, (111) terminated surfaces exhibit triangularly canted spin structures [17], while (100) terminated surfaces exhibit uniaxial surface magnetic anisotropy [1]. Since the morphology of the nanoparticles determines the fraction of (111) and (100) surfaces, it in turn will influence the effective surface anisotropy. This influence motivates our systematic study of the morphology of magnetic ferrite nanoparticles.
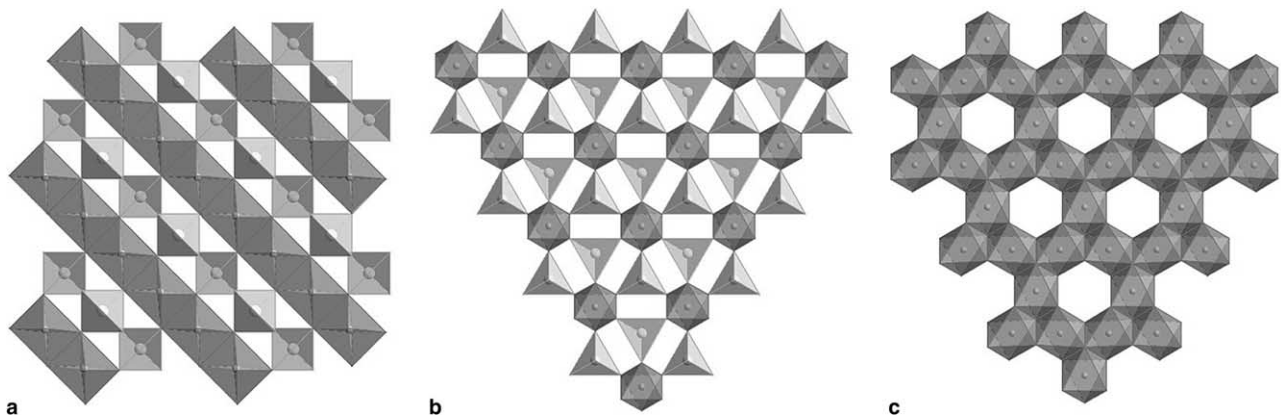

Fig. 2. The (a) (100), (b) (111)-mixed, and (c) (111)-octahedral surfaces of the spinel structure, illustrating the difference in the arrangements of the tetrahedral and octahedral units.

Despite many experimental observations of cuboctahedral morphologies in small particles [22–25,17], explanations of the evolution of these shapes in terms of nucleation and growth [26] models are sparse. Such an explanation is critical to the understanding of the influence of particle morphology on the physical properties at different sizes [1]. In this paper, we model both the critical nucleus and growth form shapes of the cuboctahedral ferrite nanoparticles by considering the Helmholtz free energies of perfect and truncated cubes and octahedra. This model considers both volume and surface energy terms (ignoring edge energies [27]) to predict the critical nucleus shapes. The growth forms are obtained by minimizing the total surface energy associated with (1 0 0) and (1 1 1) surfaces while constraining the volume to a constant size. The predicted shapes are corroborated using high-resolution transmission electron microscopy (TEM) observations of the nanoparticles. Based on the TEM observations and the proposed model, a range of the surface energy ratio of the (1 0 0) and (1 1 1) surfaces, $\frac{\gamma_{100}}{\gamma_{111}}$, is also determined. The values of $\frac{\gamma_{100}}{\gamma_{111}}$, experimental observations of three-dimensional nanoparticle shapes [28], atomic structure [17], and magnetic surface anisotropy [1] aid in the complete understanding of how surface structure influences the magnetic properties of truncated ferrite nanoparticles.

2. Ferrite nanoparticle synthesis

NiZn ferrite nanoparticles were synthesized from ball-milled metallic precursors in the desired stoichiometric ratio (Ni:Zn:Fe = 1:1:4 for $Ni_{0.5}Zn_{0.5}Fe_2O_4$ nanoparticles) using a 50 kW, 3 MHz RF plasma torch. The metallic precursors were oxidized by an oxygen-rich reactive plasma gas [29,30]. A polydisperse nanoparticle size distribution with a 12 nm mean and a 11 nm standard deviation in the particle size was observed. To isolate the small particles, a surfactant-based chemical size selection technique was used [1], which yielded a relatively monodisperse particle size distribution with a 6 nm mean and a 3 nm standard deviation.

In plasma synthesis, the nucleation and growth of particles occurs [31] after the gas-phase chemical reactions are completed in the plasma plume. The ionized metallic precursors react with oxygen and are cooled rapidly by an inert gas (Ar). Particle nucleation occurs at significant undercooling (provided by the cold inert gas) by the condensation of the supersaturated vapor. The critical nuclei approach their final growth forms [32] as the distance from the plasma nozzle exit increases [33]. The growth ceases when the particles travel out of the growth zone to where there is no further supply of atoms, embryos, or nuclei. Finally, the particles are quenched by the cooled reactor walls and collected from the reactor walls.

The polydispersity seen in RF plasma synthesized nanoparticles is attributed to the quenching of both the critical nuclei and particles that have varying degrees of growth terminated at different distances from the torch. Small particles correspond to the critical nucleus shapes, while the larger particles are growth forms.

3. TEM observations of nanoparticle shapes

The TEM images of the nanoparticles were obtained using a 200 kV, TECNAI F20 FEG TEM. The TEM specimens were prepared by dispersing the as-synthesized and size-selected particles in ethanol and placing a few drops of the dispersion on a holey-C grid. The ferrite nanoparticles exhibit faceted cuboctahedral morphologies [Fig. 3] with exclusively (1 0 0) and (1 1 1) type surfaces, as was the case for the previously studied Mn and MnZn ferrite particles [30].

Fig. 4 illustrates the high-resolution TEM images of small ((a) and (b)) (⩽≈22 nm) and large ((c)–(f)) (>22 nm) NiZn ferrite nanoparticles that have octahedral and truncated octahedral morphologies respectively. The HRTEM images in Fig. 4(a) and (b) are representative images of small octahedral nanoparticles obtained after size selection. The insets in Fig. 4(c), (e) and (f) correspond to the (c) [1 1 0] and (e), (f) [1 1 1] diffraction patterns of the respective nanoparticles and are obtained by performing Fourier transforms of the nanoparticle under consideration. The three-dimensional morphologies of the nanoparticles obtained using electron tomographic techniques [28] confirmed this difference in the particle shape between small and large nanoparticles. These experimental observations have prompted studies to determine whether the nanoparticle shapes can be described in a quantitative nucleation and growth (N&G) model. In this paper we will summarize the results of this study.
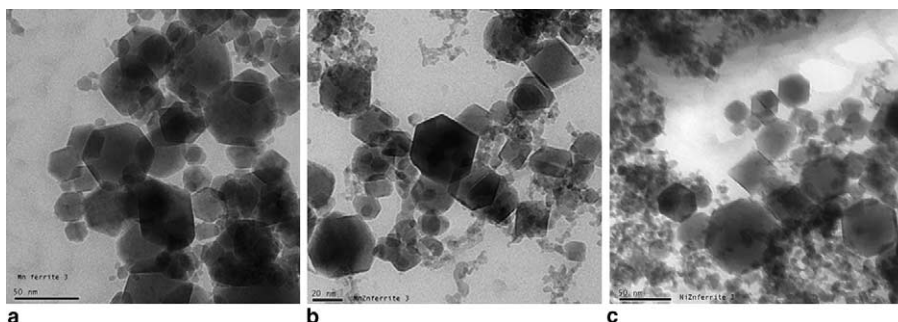

Fig. 3. Bright field TEM images of: (a) Mn ferrite, (b) MnZn ferrite and (c) NiZn ferrite nanoparticles.
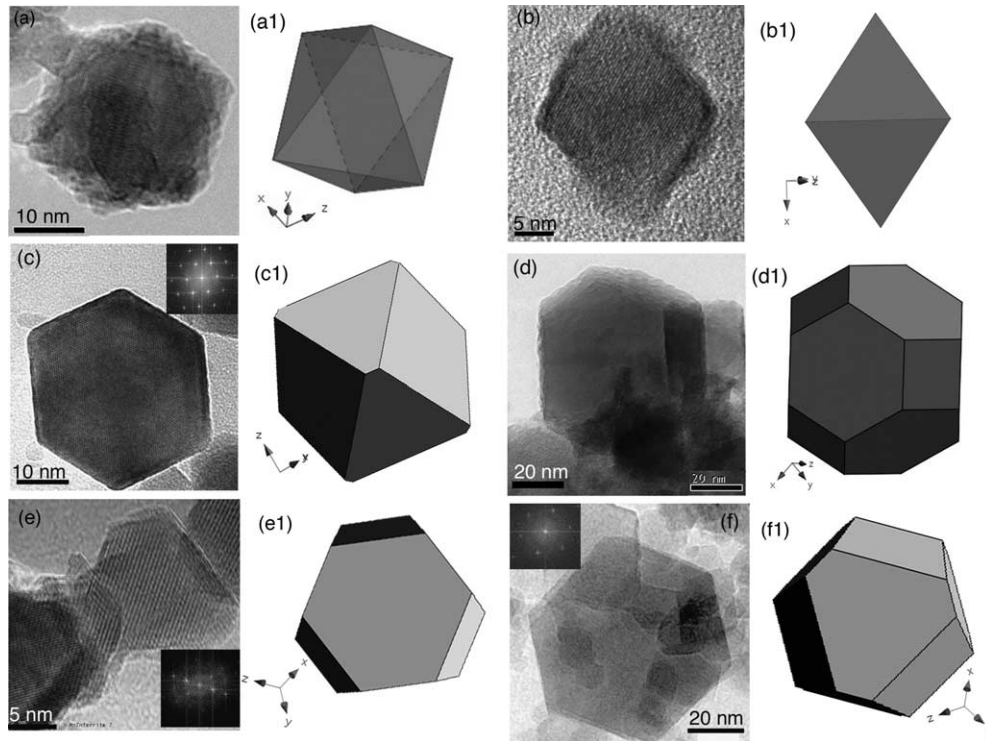
Fig. 4. High-resolution TEM images of: (a) and (b) small ferrite nanoparticles having octahedral morphologies; (c)–(f) large ferrite nanoparticles having truncated octahedral morphologies with truncation ratios 0.43, 0.36, 0.36 and 0.43, respectively. (a1)–(f1) are the projections of the corresponding polyhedral models in similar orientations.

4. Morphology model

The observed faceting of the ferrite nanoparticles indicates that the surface energy anisotropy is important in determining the final particle shape. To quantify this anisotropy of the contributing surfaces, the faceted particles have been described in terms of the truncations of the perfect cube (exclusively (100) faces) or the octahedron (exclusively (111) faces). Fig. 5 shows that the truncations of the cube and the octahedron yield solids with both (100) and (111) faces. There is a continuous truncation path from the cube to the cuboctahedron (Fig. 5(a)–(c)), and similarly from the octahedron to the cuboctahedron (Fig. 5(c)–(e)). The truncated cube, a regular Archimedean solid, is the intermediate state in the path between the cube (a Platonic solid) and the cuboctahedron. The truncated octahedron is the intermediate state in the path between the octahedron (a Platonic solid) and the cuboctahedron.

In what follows, the term truncated octahedron will refer to both regular ((111) faces that are perfect hexagons) and irregular ((111) faces are imperfect hexagons) truncations of the octahedron. The truncated cube will refer to both regular ((100) faces that are perfect octagons) and non-regular ((100) faces that are not perfect octagons) truncations of the cube. The proposed model for nucleation and growth uses the surface energy ratio of the (100) and (111) surfaces $\left(\frac{\gamma_{100}}{\gamma_{111}}\right)$ as a parameter in a normalized Helmholtz free energy formalism.

4.1. Parameterization of truncation geometry

Fig. 6(a) and (b) show projections of the (100) and the (111) faces of the truncated cube (TC) and truncated octahedron (TO), respectively. The number, type, and polygonal forms of the faces present in these truncated solids are summarized in Table 1. The cuboctahedral solid geom-
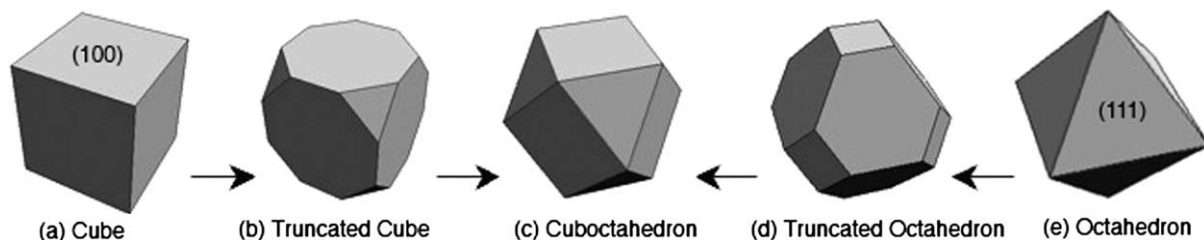

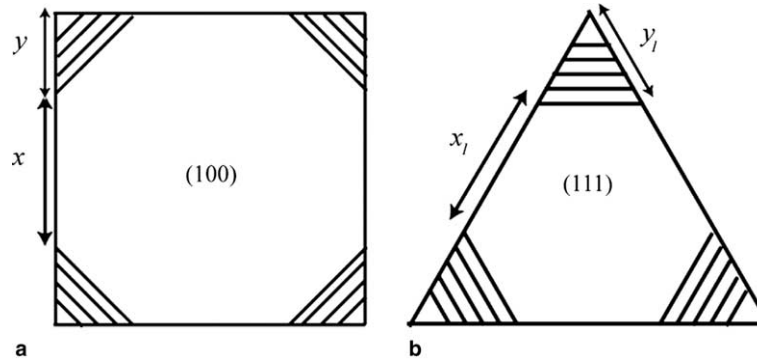Fig. 5. The various morphologies in the cuboctahedral truncations.

Fig. 6. Schematic of: (a) truncated cube and (b) truncated octahedron indicating the (100) and (111) planes, respectively. The dashed area represents the progressive truncation.

etries are parameterized in terms of two variables: x, y for the TC and x_1, y_1 for the TO. These truncation variables are independent if there is no volume constraint for a particular truncated solid; while they are dependent on each other if the volume of the solid is constrained. The truncation ratio is defined as the ratio of the length of the truncated segment to the original segment from which it was truncated. For TO, the truncation ratio is $t_1 = \frac{y_1}{(x_1 + 2y_1)}$, while for TC it is $t = \frac{y}{(x + 2y)}$. The areas of each of the (100) and (111) surfaces, A_{100} and A_{111}, and the volumes, V_T, of the TC and the TO are expressed in terms of the truncation parameters (Table 2).

4.2. Helmholtz free energy formalism for N&G

The Helmholtz free energy change, ΔF between the vapor and the solid, which is used to model the critical nucleus and growth shapes, is given by:

$$\Delta F = -V\Delta f_v + \Sigma \gamma_i A_i, \tag{2}$$

where Δf_v is the free energy change per unit volume for the formation of solid from the vapor. A particular surface facet with the normal vector (hkl) of area A_i has surface free energy γ_i.

The free energy barrier to the formation of the critical nucleus has been modeled by considering both the surface and volume energy terms (Section 4.3). This model does not impose any constraint on the volume of the particle. The equilibrium growth shapes are modeled using the Wulff construction [34] by minimizing the total surface free energy of a faceted particle, under the constraint of constant volume (Section 4.4). By constraining the volume, the truncation variables are dependent upon each other. This dependence makes determining the growth form a single variable problem, in contrast with the determination of the critical nucleus shapes, which is a two variable problem.

Table 2
Surface areas and volumes associated with the truncated cube and truncated octahedron expressed in terms of the truncation parameters

	TC	TO
A_{100}	$(x + 2y)^2 - 2y^2$	y_1^2
A_{111}	$\frac{\sqrt{3}y^2}{2}$	$\frac{\sqrt{3}}{4}[(x_1 + 2y_1)^2 - 3y_1^2]$
V_T	$(x + 2y)^3 - \frac{4y^3}{3}$	$\frac{\sqrt{2}}{3}(x_1 + 2y_1)^3 - \sqrt{2}y_1^3$

In our model, we assume that the γ_{100} and γ_{111} values are independent of the particle size. We also assume that γ_{100} and γ_{111} are less than the surface energies associated with the other high index faces. The latter is consistent with our observing no surface facets other than the (100) and (111).

The energy expressions for obtaining the critical nucleus shapes ΔF_n can be written as:

$$\Delta F_n = -V\Delta f_v + F_g, \tag{3}$$

where the total surface energy for determining the equilibrium growth shape F_g is:

$$F_g = 6\gamma_{100}A_{100} + 8\gamma_{111}A_{111}. \tag{4}$$

4.3. Critical nucleus shape determination

The homogeneous nucleation theory for solid particles nucleating from the vapor has been used [31] to describe materials produced by the plasma torch. As an embryo increases in size, the surface energy increases while the volume energy decreases. This is represented in Fig. 7, where x is a general coordinate describing the particle size. The particle size can be represented by a single variable for a sphere; whereas for a truncated cube or a truncated octahedron, it is represented by two variables. Homogeneous nucleation

Table 1
The number and types of faces for the cuboctahedral morphologies

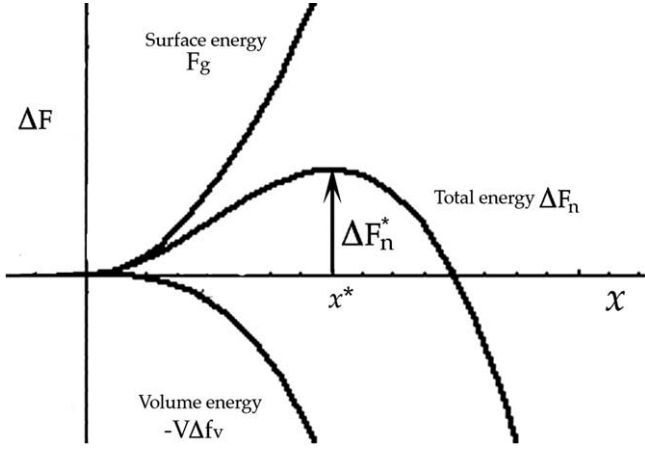| Number and type of surface	TC (Fig. 5(b))	Cuboctahedron (Fig. 5(c))	TO (Fig. 5(d))
$6 \times (100)$	Octagon	Square	Square
$8 \times (111)$	Equilateral triangle	Equilateral triangle	Hexagon

Fig. 7. Schematic for determining the critical nucleus from Eq. (3), where x is a general coordinate describing particle size and x^* is the critical nucleus size.

requires that a critical nucleus size, x^*, is reached before the particle can grow; otherwise, it is re-dissolved into the vapor solution [35]. The nucleation energy barrier and, hence, the critical nucleus are obtained at the maximum value of the total Helmholtz free energy (ΔF_n^*), where both the volume and surface terms are considered.

For faceted particles, the nucleation energy barrier is represented by the maximum value of the Helmholtz free energy as a function of the two truncation parameters (x and y for TC; x_1 and y_1 for TO) that determine the shape of the truncated particle. Determination of the critical nucleus shape requires examination of both the first and second derivatives of the Helmholtz free energy with respect to x and y (for TC). Examination of the first derivative identifies extremization conditions (maxima, minima, and the saddle points); examination of the second derivative allows us to determine which of the solutions are the maxima. The solutions that give rise to the largest maxima are the critical nuclei.

Using Eqs. (3) and (4), the total Helmholtz free energy, ΔF_n, can be calculated for the cases of truncated cubes and octahedra by substituting the appropriate area and volume terms from Table 2. ΔF_n is then normalized by γ_{111} because only the ratio of the two surface energies $\frac{\gamma_{100}}{\gamma_{111}}$ (which will be referred to as r) is important in comparing the energies of different shapes. These normalized energies for the truncated cube ($F_n^{c'} = \frac{F_n^c}{\gamma_{111}}$) and the octahedra ($F_n^{o'} = \frac{F_n^o}{\gamma_{111}}$) can be expressed in terms of r and the truncation parameters (Fig. 6) as:

$$F_n^{c'} = -\frac{\Delta f_v}{\gamma_{111}}\left[(x+2y)^3 - \frac{4y^3}{3}\right] + 6r[(x+2y)^2 - 2y^2] + 4\sqrt{3}y^2$$
(5)

$$F_n^{o'} = -\frac{\Delta f_v}{\gamma_{111}}\left[\frac{\sqrt{2}}{3}(x_1+2y_1)^3 - \sqrt{2}y_1^3\right] + 6ry_1^2$$
$$+ 2\sqrt{3}[(x_1+2y_1)^2 - 3y_1^2]$$
(6)

$F_n^{c'}$ and $F_n^{o'}$ are the effective total Helmholtz free energy expressions that will be used for further analyses. These are functions of the corresponding truncation parameters, r and $\frac{\Delta f_v}{\gamma_{111}}$. We have confirmed that the results in the variation of the critical nucleus shapes with r is independent of the actual value of $\frac{\Delta f_v}{\gamma_{111}}$. Consequently, for simplicity in the mathematical analysis, $\frac{\Delta f_v}{\gamma_{111}} = 1$ will be used in this paper.

The nucleation energy barrier is obtained from the two-variable calculus problem of maximizing the functions $F_n^{c'}$ and $F_n^{o'}$ with respect to the two independent truncation parameters (x and y for TC; x_1 and y_1 for TO). The solutions from the first derivative analysis yields x and y in terms of r (for TC). Only those solutions for which both x and y are non-negative are examined further for the presence of a maxima, using the second derivative criterion. This criterion, for a function of two-variables (shown for TC), restricts all the eigenvalues of the matrix M to be negative

$$M = \begin{pmatrix} \frac{\partial^2 F_n^{c'}}{\partial x^2} & \frac{\partial^2 F_n^{c'}}{\partial x \partial y} \\ \frac{\partial^2 F_n^{c'}}{\partial y \partial x} & \frac{\partial^2 F_n^{c'}}{\partial y^2} \end{pmatrix} < 0$$
(7)

In the following sections, the first and second derivative analysis of the solutions for TC are discussed in detail while only the final solutions are presented for the TO.

4.3.1. Solutions from first derivative analysis and their physical validity

$F_n^{c'}$ is maximized when $\frac{\partial F_n^{c'}}{\partial x} = 0$ and $\frac{\partial F_n^{c'}}{\partial y} = 0$. The three solutions for x and y in terms of r, apart from the trivial solution $x = y = 0$, are:

1. $x = 4r$, $y = 0$ (Perfect cube) – non-negative in all r ranges.
2. $x = 4(\sqrt{3} - 3r), y = -2(\sqrt{3} - 3r)$ (Truncated Shape) – non-negative only at $r = \frac{1}{\sqrt{3}}$.
3. $x = 4(\sqrt{3} - 2r), y = -2(\sqrt{3} - 3r)$ (Truncated Shape) – non-negative when $\frac{1}{\sqrt{3}} < r < \frac{\sqrt{3}}{2}$.

4.3.2. Analysis of maxima from second derivative analysis

Each non-negative solution obtained as an extrema from the first derivative analysis is examined using the second derivative criterion (Eq. (7)) for the presence of a maxima. Only the solutions that yield all negative eigenvalues of the matrix M are considered as the maxima. These are, then, the possible solutions to the critical nucleus. In this section, we will analyze all the solutions for the TC for the presence of a maxima.

1. $x = 4r$, $y = 0$ (Perfect cube) – both the eigenvalues of M are negative when $r \geqslant \frac{1}{\sqrt{3}}$.
2. $x = 4(\sqrt{3} - 3r), y = -2(\sqrt{3} - 3r)$ (Truncated Shape) – never has negative eigenvalues in any r range.

55

3. $x = 4(\sqrt{3} - 2r), y = -2(\sqrt{3} - 3r)$ (Truncated Shape) – both the eigenvalues of M are negative when $r < \frac{1}{\sqrt{3}}$. But, this is not a non-negative r range.

From this analysis, we conclude that for the case of the truncated cubes, only the perfect cube is the critical nucleus shape for $r \geqslant \frac{1}{\sqrt{3}}$. Likewise, the perfect octahedron is the only critical nucleus shape for the truncated octahedra for $r \leqslant \sqrt{3}$. So, in the r range where the truncated shapes can exist ($\frac{1}{\sqrt{3}} < r < \sqrt{3}$), it has been demonstrated that only the perfect cubes or the perfect octahedra can be the critical nucleus shapes. A trivial extension confirms that the perfect cubes are the critical nucleus shapes for $r < \frac{1}{\sqrt{3}}$ and the perfect octahedra are the critical nucleus shapes for $r > \sqrt{3}$.

For surface energy ratios, r, between $\frac{1}{\sqrt{3}}$ and $\sqrt{3}$, either the cube or the octahedron could be a critical nucleus shape. Therefore, an additional criterion must be applied to determine which form is most stable for different values of r in this region. This is accomplished by comparing the values of the nucleation energy barrier of the octahedral and cubic shapes – $\Delta F^*_{\text{octahedron}}$ vs. ΔF^*_{cube} at various values of r, as shown in Fig. 8. The shape with the lower value of the barrier is the critical nucleus shape for a given r.

The γ_{111}-normalized Helmholtz free energy curves for the cube and the octahedron are plotted with the same abscissa. At $r = \frac{3^{1/6}}{2^{1/3}}$, both the cube and the octahedron have the same values of ΔF^*. Above this value of r, the octahedron is the critical nucleus shape; and below it, the cube is the critical nucleus shape. The small ferrite nanoparticles,

which correspond to the critical nucleus shapes, exhibit only perfect octahedral morphologies (Fig. 4(a) and (b)). This consistency indicates that the r values of the ferrite nanoparticles are $\geqslant \frac{3^{1/6}}{2^{1/3}} = 0.95$.

There have been differing views [36,37] on the applicability of equilibrium crystal shapes determined using the Wulff construction to critical nucleus shapes. In this study, the critical nucleus shapes have been modeled while taking into account competing surface and volume energy terms; and, these shapes have been shown to be perfect octahedra or perfect cubes. The equilibrium crystal growth forms will be modeled in the next sub-section by considering two competing surface energy terms. These shapes are invariably the truncated Platonic solids. The mathematical model presented in this study indicates that the critical nucleus shapes need not be the same as the equilibrium growth shapes. Also, due to the geometrical differences between a cube and an octahedron, the critical nucleus shapes are perfect octahedra for $r > 0.95$, and are not for $r > 1$.

4.4. Equilibrium growth form determination

The equilibrium growth shapes are obtained by the progressive atomic attachment to the critical nuclei [32,33]. In this paper, these equilibrium growth forms for cuboctahedral ferrite nanoparticles are modeled by minimizing the total surface free energy, $\sum_i \gamma A_i$, under the constraint of a fixed particle volume. It has been shown that the result presented in this model is applicable to any constant value of
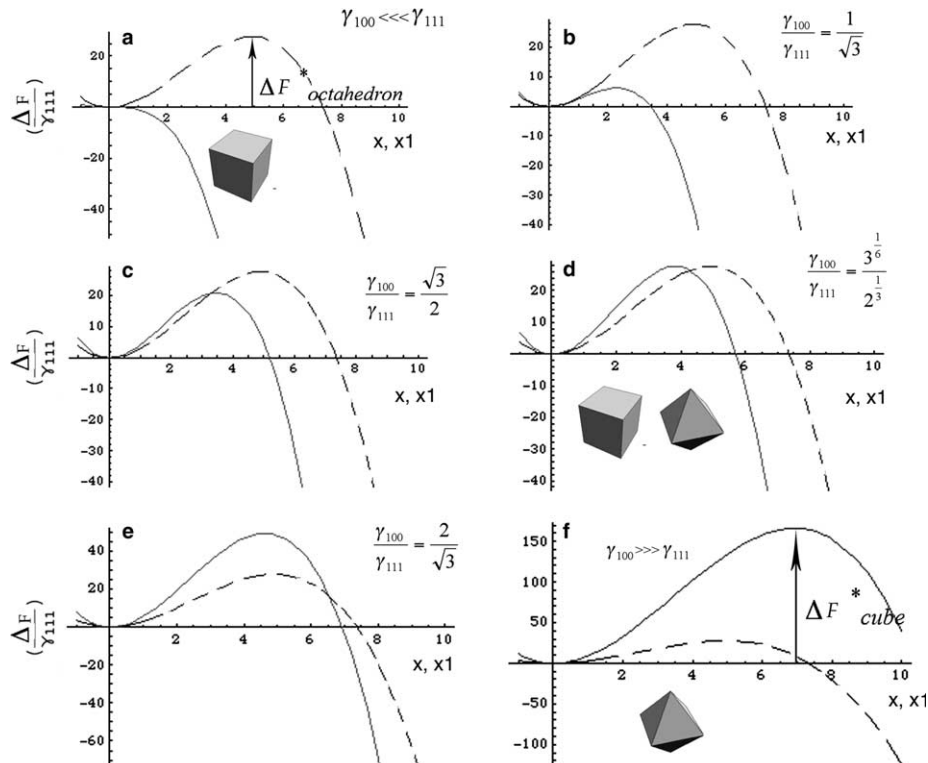

Fig. 8. The normalized nucleation energy curves as a function of x, x_1, indicating the ΔF^* for the formation of the critical nucleus for the cube (solid line) and the octahedron (dashed line) at various surface energy ratios. This figure also indicates the various shapes that are critical nuclei at various r values.

V_T. Volume normalization ($V_T = 1$ for simplicity) yields the following relation for TC (from Table 2)

$$x = \left(1 + \frac{4y^3}{3}\right)^{1/3} - 2y \tag{8}$$

The corresponding relation for TO is given by:

$$x_1 = (3/\sqrt{2})^{1/3}\left(1 + \sqrt{2}y_1^3\right)^{1/3} - 2y_1 \tag{9}$$

These relations (Eqs. (8),(9)) make the Wulff construction a single variable problem.

The total surface energy expression for the TC based on Eq. (8) (assuming that $V\Delta f_v$ is a constant, as it does not contribute to the minimization) is

$$\frac{F_g^c}{\gamma_{111}} = 4\left(\sqrt{3} - 3r\right)y^2 + 6r\left(1 + \frac{4y^3}{3}\right)^{2/3} \tag{10}$$

This γ_{111}-normalized surface energy is then minimized with respect to the single truncation parameter y to obtain the equilibrium growth forms. The minimal energy for a particular r value corresponds to the particle of the corresponding equilibrium growth shape and size. From this analysis, we obtain $\frac{1}{\sqrt{3}} < r < 1.464$ as the surface energy ratio range where the truncated cubes are the equilibrium shapes for various particle sizes y. Similarly, the truncated octahedra are the equilibrium growth shapes for $0.5311 \leqslant r < \sqrt{3}$ for particle sizes y_1.

The favored range of r for the TC and that for the TO overlap between $\frac{1}{\sqrt{3}}$ and $\sqrt{3}$. Therefore, an additional criterion must be applied to determine which growth form is most stable for different values of r in this range. This is accomplished by comparing the values of the total surface energies for both the cases at various values of r, as shown in Fig. 9. The solid curves are the γ_{111} normalized energy curves for the TC and the dashed curves are those for the TO. The curves have been rescaled to provide coinciding energy and volume values at the cuboctahedron. The absolute minimum in these energy curves, which correspond to the equilibrium growth shapes for a particular r value, occurs for the TC till $r = \frac{\sqrt{3}}{2}$, and for TO beyond this. At $r = \frac{\sqrt{3}}{2}$ (Fig. 9(c)), the energies for the TC and the TO exhibit a minimum at the ideal cuboctahedron. For $r < \frac{\sqrt{3}}{2}$, the truncated cubes are the equilibrium growth forms; while for $r > \frac{\sqrt{3}}{2}$, the truncated octahedra are the growth forms. The equilibrium shapes for $r \leqslant \frac{1}{\sqrt{3}}$ and $r \geqslant \sqrt{3}$ are the cube and octahedron, respectively.

4.5. Summary of nucleation and growth model

A nucleation and growth model was developed for particles formed in a plasma using a normalized Helmholtz free energy formalism. While the critical nucleus was modeled without a volume constraint, the equilibrium growth forms were modeled with a constraint on the particle
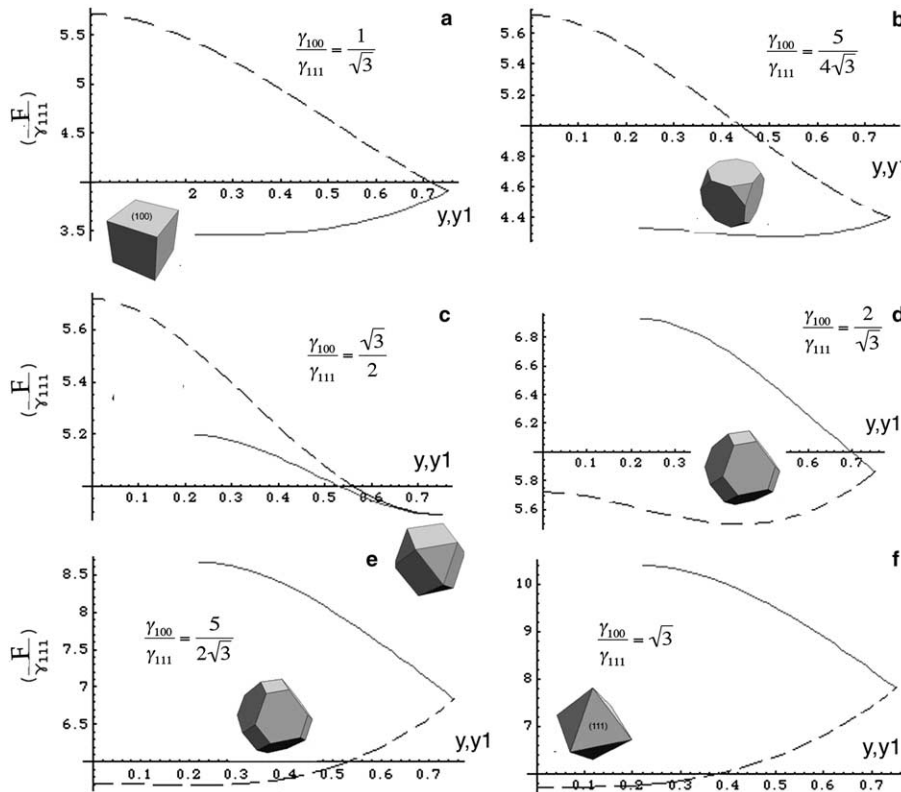

Fig. 9. γ_{111} normalized energy curves that depict the equilibrium morphologies for various $\frac{\gamma_{100}}{\gamma_{111}}$ ratios. The solid curve corresponds to the energy curves for the TC and the dashed curve corresponds to the energy curve for the TO. The absolute minimum in energy for either curves is the equilibrium growth shape for a particular r value.
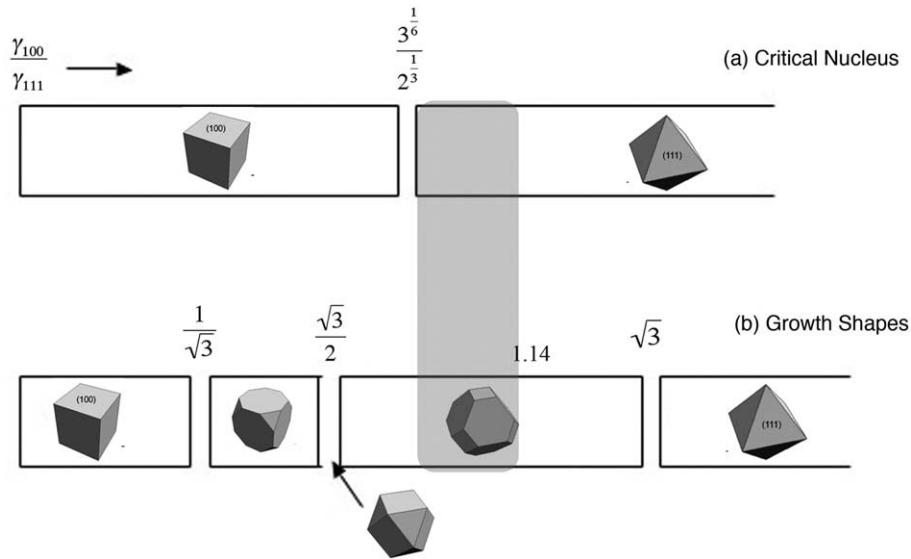
Fig. 10. Surface energy ratio limits for observing the critical nucleus and growth shapes in the cuboctahedral morphologies. The shaded region corresponds to the surface energy ratio $\frac{\gamma_{100}}{\gamma_{111}}$ estimated in Section 4.6.

volume. This model was then used to determine the critical nucleus and growth shapes for various values of the surface energy ratio (r) of the (100) and (111) surfaces.

For $0 < r \leqslant \frac{3^{1/6}}{2^{1/3}}$, the critical nucleus shape is the cube; while for $r \geqslant \frac{3^{1/6}}{2^{1/3}}$, the critical nucleus shape is the octahedron (Fig. 10(a)). The perfect cubes are the equilibrium shapes for $0 < r \leqslant \frac{1}{\sqrt{3}}$. The truncated shapes (TC and TO with varying degrees of truncation) are the equilibrium shapes for $\frac{1}{\sqrt{3}} < r < \sqrt{3}$. The octahedron is the equilibrium shape for $r \geqslant \sqrt{3}$ (Fig. 10(b)).

4.6. Validity of model

Because the small ferrite nanoparticles are perfectly octahedral (Fig. 4(a) and (b)) and correspond to the critical nucleus shapes, we infer that $r \geqslant \frac{3^{1/6}}{2^{1/3}} = 0.95$. The larger particles have truncated octahedral shapes (Fig. 4(c)–(f)), which are the growth forms for $r \geqslant \frac{\sqrt{3}}{2}$. Based on these two observations, the lower bound on r is 0.95. The high resolution TEM images of a number of truncated octahedral nanoparticles suggest that the these particles have a truncation ratios (t_1) range, given by $0.35 < t_1 < 0.45$. This range in t_1 is obtained by visual comparison of the high resolution images to the solid truncated polyhedral models (Fig. 4(c)–(f)). This t_1 range corresponds to $1.1 < \frac{y_1}{x_1} < 4.4$ (using the relationship, $y_1/x_1 = t_1/(1 - 2t_1)$).

The $\frac{y_1}{x_1}$ range can be independently obtained from the nucleation and growth model that has been proposed. The y_1 values are obtained as the energy minima of the TO for various values of r, and the corresponding x_1 values are obtained from the normalization relationship for TO, as shown in Eq. (9). The r range where this $\frac{y_1}{x_1}$ obtained from the N&G model coincides with the $\frac{y_1}{x_1}$ range obtained from the visual comparison to the polyhedral models is $0.95 < r < 1.14$. Therefore, this r range is $\frac{\gamma_{100}}{\gamma_{111}}$, predicted

for the ferrite nanoparticles by considering the equilibrium growth shapes. This is also a valid r range for the critical nucleus shape to be the perfect octahedron. Therefore, the $\frac{\gamma_{100}}{\gamma_{111}}$ for the plasma synthesized, cuboctahedral ferrite nanoparticles, determined from the nucleation and growth model is $0.95 < \frac{\gamma_{100}}{\gamma_{111}} < 1.14$.

5. Conclusions

Ferrite nanoparticles synthesized using an RF plasma torch exhibited morphologies that were exclusively cuboctahedral, having only (111) and (100) surfaces. A nucleation and growth model for the evolution of cuboctahedral nanoparticle shapes was developed. The critical nucleus shapes were predicted to be either a cube or an octahedron. The growth shapes corresponded to the truncated shapes, depending on the $\frac{\gamma_{100}}{\gamma_{111}}$. The high-resolution TEM observations confirm that the small particles, which are the critical nucleus shapes, are perfectly octahedral; and, the larger particles, which are the growth forms, are truncated octahedral. Based on these observations, the surface energy ratio ($\frac{\gamma_{100}}{\gamma_{111}}$) for the ferrite nanoparticles was estimated to be between 0.95 and 1.14.

References

[1] Swaminathan R, McHenry ME, Poddar P, Srikanth H. J Appl Phys 2005;97:10G104.

[2] Kodama RH, Berkowitz AE, McNiff Jr EJ, Foner S. Phys Rev B 1996;77:394.

[3] Willard MA, Kurihara LK, Carpenter EE, Calvin S, Harris VG. Int Mater Rev 2004;49(3-4):125–70.

[4] Abe M, Matsushita N. J Magn Soc Jpn 2003;27(6):721–9.

[5] Vollath D, Szabo DV, Fuchs J. In: Materials research society symposium proceedings: advanced hard and soft magnetic materials; 1999. p. 443–8.

[6] Berry CC, Wells S, Charles S, Curtis Adam SG. Biomaterials 2003;24:4551–7.

[7] Fang M, Grant PS, McShane MJ, Sukhorukov GB, Golub VO, Lvov YM. Langmuir 2002;18:6338–44.

[8] Ito A, Matsuoka F, Honda H, Kobayashi T. Cancer Gene Therapy 2003;10:918–25.

[9] Nitin N, LaConte LEW, Zurkiya O, Hu X, Bao G. J Biol Inorganic Chem 2004;95:706–12.

[10] Frankel RB, Blakemore RP, Wolfe RS. Science 1979;203(4387):1355–6.

[11] Thomas-Keptra KL et al. Proc Natl Acad Sci 2001;98(5):2164–9.

[12] Buseck PR et al. Proc Natl Acad Sci 2001;98(24):13490–5.

[13] Friedmann EI, Wierzchos J, Ascaso C, Winklhofer M. Proc Natl Acad Sci 2001;98(5):2176–81.

[14] Mann S, Frankel RB, Blakemore RP. Nature 1984;310(5976):405–7.

[15] McKay CP, Friedmann EI, Frankel RB, Bazylinski DA. Astrobiology 2003;3(2):263–70.

[16] Gleiter H. Prog Mater Sci 1989;33(4):223–315.

[17] Swaminathan R, McHenry ME, Calvin S, Sorescu M, Diamandescu L. Proceedings of the ninth international conference on ferrites. American Ceramic Society; 2005. p. 847–52.

[18] Gorter EW. Philips Res Rep 1954;9:295–442.

[19] Yafet Y, Kittel C. Phys Rev 1952;87:290–4.

[20] Nèel L. J Phys Radium 1954;15:225.

[21] Chuang DS, Ballentine CA, O'Handley RC. Phys Rev B 1994;49(21):15084–95.

[22] Kimoto K. J Jpn Cryst Growth Soc 1979;6(3):122–65.

[23] Marks LD. Rep Prog Phys 1994;57:603–49.

[24] Flueli M, Borel JP. J Cryst Growth 1998;91:67–70.

[25] Wang ZL. Adv Mater 1998;10(1):13–30.

[26] Wang SW, Falicov LM, Searcy AW. Surf Sci 1984;143:609–25.

[27] Wonczak S, Strey R, Stauffer D. J Chem Phys 2000;113(5):1976–80.

[28] Swaminathan R, Nuhfer NT, McHenry ME. Proc Microsc Microanal, in press.

[29] Son S, Taheri M, Carpenter E, Harris VG, McHenry ME. J Appl Phys 2002;91:7589–91.

[30] Son S, Swaminathan R, McHenry ME. J Appl Phys 2003;93:7495–7.

[31] Girshick SL, Chiu CP. Plasma Chem Plasma Process 1989;9(3):355–69.

[32] Girshick SL. Plasma Sources Sci Technol 1994;3:388–94.

[33] Rao N, Girshick S, Heberlein J, McMurray P, Jones S, Hansen D, et al. Plasma Chem Plasma Process 1995;15(4):581–606.

[34] Herring C. Phys Rev 1951;82(1):87–93.

[35] Porter DA, Easterling KE. Phase transformations in metals and alloys. second ed. New York, NY: Chapman and Hall; 1992 [p. 186–89, Chapter 4].

[36] Ramanujan RV. Mater Sci Eng 1995;B32:125–35.

[37] Lee JK, Aaranson HI. Acta Metall 1975;23:799–808.